Surface Functionalization of Graphene Devices

by

Xu Zhang

B.S., University of Science and Technology of China (2010)

Submitted to the Department of Electrical Engineering and Computer Science in partial fulfillment of the requirements for the degree of

Master of Science

At the

MASSACHUSETTS INSTITUTE OF TECHNOLOGY

September 2012

Author_____
Department of Electrical Engineering and Computer Science
August 30, 2012

Certified by

_____

Tomás Palacios

Professor of Electrical Engineering and Computer Science, Thesis Co-Advisor

_____

Mildred Dresselhaus

Professor of Physics and Electrical Engineering and Computer Science, Thesis Co-Advisor

Accepted by

_____

Leslie A. Kolodziejski

Chair, Department Committee on Graduate Students

(This page is left intentionally blank)

Surface Functionalization of Graphene Devices

By

Xu Zhang

Submitted to the Department of Electrical Engineering and Computer Science
September 2012, in partial fulfillment of the
requirements for the degree of
Master of Science

Abstract

Graphene, a zero-gap semiconductor with massless charge carriers, is emerging as an amazing material for future electronics, due to its outstanding electrical and mechanical performances. However, the lack of a bandgap results in a high off-state current leakage and a nonsaturating drive current, both of which severely limit graphene's practical applications in electronic devices. Chemical functionalization on its surface promises a powerful tool to manipulate its electronic properties and modify its atomic structures. Graphene is a true two-dimensional material; every carbon atom in single layer graphene is exposed to its environment. Therefore, the surface functionalization in graphene can significantly change its physical and chemical properties, such as bandgap opening and piezoelectricity engineering, etc. Hydrogenation and fluorination have been experimentally demonstrated to be effective in changing the hybridization state of carbon atoms and opening a bandgap from 2.9 eV to 5.4 eV. However, both of these methods are destructive to graphene, and will degrade its carrier mobility.

In this study, we fabricated graphene-based field effect transistors (FETs) and conducted surface functionalization via plasma reactions. We systematically investigated graphene chlorination and characterized the results with Raman spectroscopy, X-ray photoelectron spectroscopy, atomic force microscopy (AFM) and transport measurement. A schematic picture of how the chlorine plasma interacts with graphene was also proposed. Hydrogenation and fluorination were also conducted and analyzed as comparison.

We demonstrated that chlorination in graphene via plasma reactions is a very effective and controllable way to engineer its structural and electronic properties. The high mobility of the resulting structures is a very important advantage with respect to other functionalization approaches.

Keywords: Graphene, functionalization, chlorination, plasma, bandgap, Fermi level, doping, mobility

(This page is left intentionally blank)

Acknowledgement

First and foremost, I would like to express my sincere gratitude to my co-advisors, Prof. Mildred Dresselhaus and Prof. Tomás Palacios. It would not have been possible to complete this thesis without their continuous support and encouragement. It is a great opportunity for me to have rich exposure to both basic physics research and electrical engineering technology.

It has been a great honor and privilege for me to work in the Dresselhaus Group and Palacios' Group. The experience under the supervision of my co-advisors is a combination of exploring both fundamental science and innovative technology. It is the best learning experience that I can image. I sincerely appreciate Prof. Dresselhaus and Prof. Palacios for their motivation, patience, immense knowledge and sharp minds. I am also very grateful to Prof. Jing Kong for her guidance and generous support. Every time I talked to her, she was always willing to help and gave me a lot of valuable advices. I am also thankful to my friends for their kind help and bringing me lots of fun.

Most importantly, my deepest gratitude goes to my parents who give me unlimited love. Their love is my driving force to pursuit for excellence and rise to the challenges I face.

(This page is left intentionally blank)

Table of Contents

(This page is left intentionally blank)

List of Figures

List of Tables

(This page is left intentionally blank)

Chapter 1 Introduction

1.1 Physics in Graphene

Graphene, a two-dimensional honeycomb network of sp^2-hybridized carbon atoms, has attracted tremendous interest in the scientific community, thanks to its unique electron physics, as well as its promising applications in electronic devices[1]. Each carbon atom has four valence electrons. Three of these four valence electrons participate in the in-plane bonding to their three nearest neighbors (σ-bonds), and the fourth π-bond is oriented perpendicular to the surface and is delocalized[2]. Figure 1 and figure 2 show a schematic of the atomic structure and the electronic orbitals of graphene.

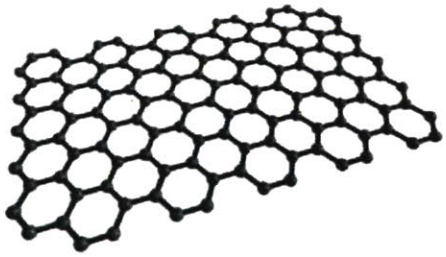

Figure 1 The atomic structure of the graphene lattice[2]

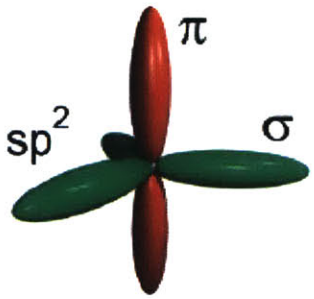

Figure 2 Illustration of the electronic bonding among the graphene valence electrons[2]

There are two equivalent triangular sublattices A and B in the graphene structure. This unique atomic arrangement results in a band structure exhibiting a linear energy dispersion relation for electrons, i.e. the energy E(k) is proportional to crystal momentum k [3]. The conduction band and valence band intersect at a so-called Dirac point, i.e. graphene is a zero bandgap material. An illustration of the graphene band structure near the Dirac point is shown below in Figure 3.

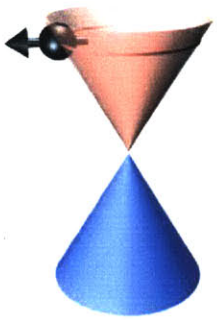

Figure 3 A schematic of the graphene band structure near the Dirac point [3]

What makes graphene so unique is that its Hamiltonian is the same as the one in the relativistic Dirac equation, with zero effective mass at the low energy spectrum. The only difference is that the Fermi velocity of graphene serves in the role of the light speed c. That is the reason why electrons in graphene are called "massless Dirac fermions"[3]. In the relativistic Dirac equation, the wave function (i.e. spinor) can be expressed as a two-component vector, which results from the two spin angular momenta components (+1/2 and -1/2). Similar, the wave function of electrons in graphene also has two components, but they originate from the two equivalent carbon sublattices A and B. The two components are named as "pseudospin" components. The wave functions in the vicinity of K and K' (Dirac point) are chiral [4]. As a consequence, many unique physical effects are found in graphene, such as the half-integer quantum Hall effect, Klein tunneling and universal quantum limited conductivity etc [5]. In addition, graphene possesses outstanding mechanical and electrical properties which will be discussed in the next section.

1.2 Advantages of Graphene

➢ Mobility

Due to its very unique band structure, electrons in graphene behave like massless Dirac fermions, with Fermi velocity 1/300 of the light speed, which is ten times higher than in silicon[3]. Moreover, the mean free path of graphene can be as long as 400nm at room temperature, which means that the carriers in graphene can travel ballistically for 400nm[6] without experiencing any scattering. All these together enable an ultrahigh mobility in graphene: For exfoliated graphene on SiO_2 substrates, mobilities of 10,000-15,000 cm^2/Vs can be easily achieved[7]. And the fact that the mobility in graphene on SiO_2 is only weakly dependent on temperature indicates that impurity scattering is the main factor limiting the mobility measured in graphene[7][8]. It has been experimentally demonstrated that the mobility in suspended graphene devices can be as high as 1,000,000 cm^2/Vs. For large area chemical vapor deposition (CVD) grown graphene transferred onto SiO_2 substrates, a mobility higher than 3700 cm^2/Vs can be achieved[9]. Recently, a novel, dry-transfer method was developed to minimize chemical contamination during transfer, and thereby the mobility can range from 30,000 cm^2/Vs at high carrier density to 50,000 cm^2/Vs at a carrier density lower than $5 \times 10^{12} cm^{-2}$ [10].

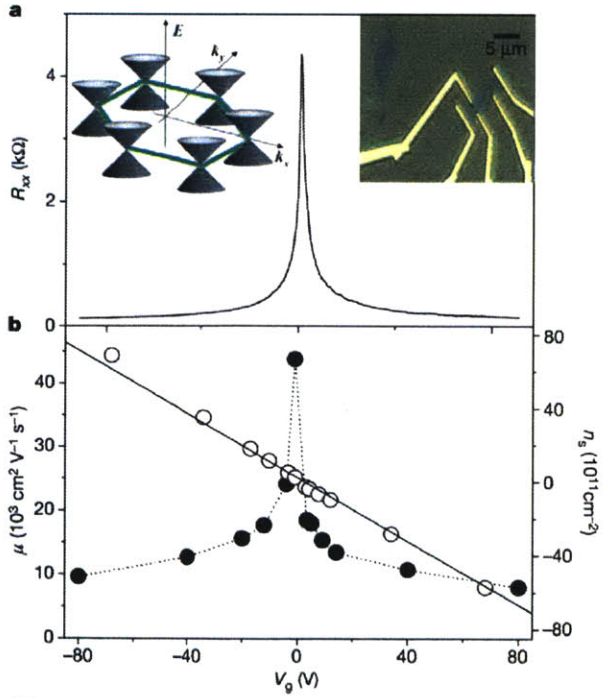

Figure 4 The relation between mobility and gate voltage, and the relation between carrier concentration and gate voltage. The upper left inset is the band structure of graphene. The upper right one is the optical image of the graphene device. [11]

For comparison, the silicon MOSFET channel mobilities are around a few 100 cm^2/Vs. For GaAs pHEMTs, the mobilities can reach 6,000 cm^2/Vs. For InP HEMTs and GaAs mHEMTs (Metamorphic High Electron Mobility Transistors), their carrier mobilities can be as high as 10,000 cm^2/Vs [12]. Therefore, the electron mobilities in graphene are very attractive. In addition, the hole mobilities in graphene are also quite competitive, much higher than in any other semiconductors[13]. However, it is also worth noting that top-gate fabrication and edge roughness in graphene will degrade its channel mobility to some degree.

- **Robustness against "short-channel" scaling**

Graphene is a real two-dimensional material, with only one atomic layer in thickness, which makes it more robust against "short-channel effects" when scaling down the channel length[12]. In the semiconductor industry, it is desirable to push down the limit of the channel length in order to increase the operation speed and the number of components per chip. However, fabricating "short" gate length will eventually lead to short-channel effects, such as drain-induced barrier lowering (DIBL), threshold voltage roll-off, and poor sub-threshold slope[14]. A channel is "short" when the channel length is on the same order as the depletion-layer widths of the source and drain junction. The thinner the channel is, the better the electrostatic integrity and better gate control of the channel potential, which means that the MOSFET vertical dimensions should be scaled along with the horizontal dimensions. The two-dimensional nature of graphene enables its largest potential to scale down its channel lengths without severe "short-channel" effects[12].

- **High-field Transport**

In order to fully investigate graphene's performance when scaling down its channel length, we have to examine its high-field transport properties. Let us consider a graphene field effect transistor (FET) with a channel length 20nm and a voltage of 0.2V drop between the source and drain terminals. The average field along the channel will be around 100kV/cm. At such high electrical fields, the carrier velocity in the channel will saturate before carriers reach the drain terminal[12]. Mobility is then no long as a good indicator of the FETs' performance; the saturating velocity becomes a critical figure of merit instead. Figure 5 shows how the electron velocity changes as the electrical field increases for graphene (simulation)[10], carbon nanotubes (CNT), Silicon, GaAs and InGaAs. There are several interesting observations that can be made. First of all, the saturating velocities for graphene and CNTs are much higher than that of silicon and III-V compounds; this means graphene is possible to enable higher speed transistors. Secondly, the saturating electrical field required for graphene is not very different from III-V semiconductors, but much smaller than for silicon. Moreover, the high-field carrier velocity in graphene does not decrease as radically as III-V materials after it saturates [10]. Therefore, from

the high-field perspectives, graphene outperforms silicon, and some members of the III-V family.

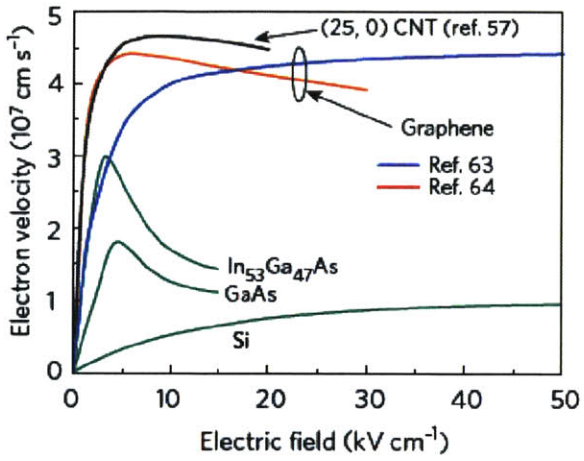

Figure 5 The relation between electron velocity in graphene and the applied accelerating electric field[12]

➢ High Thermal Conductivity

The thermal conductivity of suspended graphene ranges from 4.84×10^3 to 5.30×10^3 W/mK[15], much higher than for copper. The superior thermal conductivity makes graphene an excellent material for thermal management. According to the projected performance metrics of the "End-of-the Roadmap" CMOS circa 2020 table, the demanding requirement on managing power dissipation is the critical bottleneck that limits us to scale down of the size of modern FETs[6]. Graphene can be a potential candidate as a heat spreader in modern electronic chips. Furthermore, the excellent current carrying capability (10^8 A/ cm^2)[16], together with its outstanding thermal conductivity, makes graphene very suitable to function as interconnects in microelectronic circuits.

➢ Compatibility with Planar Processing

The true two-dimensional nature of graphene makes it perfectly compatible with planar processing technology in the semiconductor industry[2]. For chemical vapor deposition (CVD) grown graphene, the best quality can be achieved by growing graphene on copper foil[17]. The wet transfer technology permits us to transfer graphene from copper to arbitrary substrates. By using a doped silicon wafer with a 300nm oxide layer on top, the optical contrast can be optimized for single layer graphene under an optical microscope[18]. In the meantime, the doped silicon substrate can function as a back-gate, while the 300nm SiO_2 layer serves as the

dielectric layer. The fabrication of graphene devices follows the standard silicon processing technology after being transferred onto a silicon substrate, including photolithography, electron beam lithography, reactive ion etching, and metal deposition as electrodes etc[2]. Figure 6 shows a schematic of a graphene FET with a source, drain and back-gate. The high integration potential with CMOS technology in wafer-scale graphene makes it a very promising post-silicon electronic material. The detailed graphene FET fabrication processes will be discussed in Chapter 2.

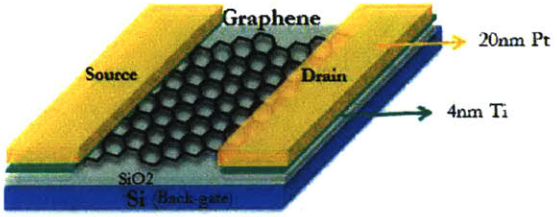

Figure 6 A schematic of a graphene FET with a source, drain and backgate. The electrodes are made of 4nm Ti on top of 20nm Pt, where the Ti is deposited as an adhesion layer

1.3 Challenges of Graphene

➢ Poor switching capability

The on/off ratio for graphene FETs is very low; a high off-state leakage makes graphene not suitable for logic circuit applications. There are two main reasons for the poor switching capability in graphene. First of all, large-area graphene has no bandgap. Figure 7 plots the band structure of graphene calculated by a tight-binding model[5].

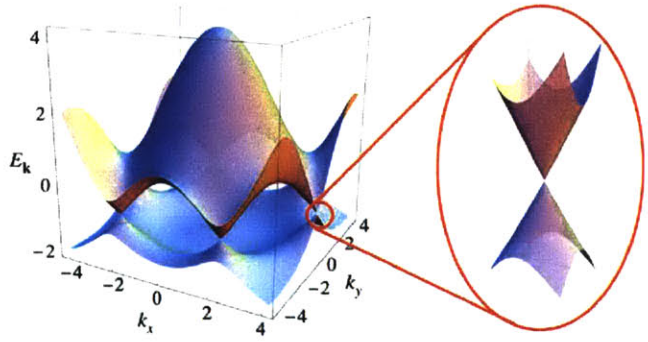

Figure 7 The full band structure in graphene by a tight binding model calculation, and a zoom-in of the part close to one of the Dirac points[5]

The conduction and valence bands in graphene touch each other at k=0 in momentum space, which is defined as the Dirac point. Close to the Dirac point, the energy-momentum relation is linear for electrons (holes) in the conduction (valence) band, rather than the quadratic relation recurring in usual semiconductors[5]. This is the most striking feature in the graphene band structure. However, in order to work as a logic circuit material, a bandgap of at least 0.4eV is necessary[12]. Therefore, a graphene FET cannot be switched off, which limits its applications in the semiconductor industry.

Secondly, the Klein tunneling effect makes the situation even worse. In quantum mechanics, particle tunneling describes the process whereby an energetic particle is transmitted through a potential barrier with a height higher than its kinetic energy (classically forbidden region). For ordinary non-relativistic particles, the transmission probability exponentially depends on the height and width of the energy barrier[5][19]. However, for Dirac fermions like carriers in graphene, the transmission probability depends very weakly on the barrier height, but depends on how sharp the barrier is. For an infinitely high barrier, Dirac fermions can achieve perfect transmission[4]. Therefore, electrons in graphene can tunnel through a very high and sharp energy barrier at normal incidence, which makes a graphene FET even harder to switch off completely.

Figure 8 shows a sketch of the drain current characteristics in graphene FETs. We see here clearly how the channel current changes with backgate bias. At a Dirac voltage V_{Dirac}, the conductance reaches its minimum value, since the Fermi level lies across the Dirac point, where the density of states is zero ideally. The Dirac point is determined by the work function, the interface with substrates and the doping level etc. When V_{gs} , the backgate bias voltage, is larger than V_{Dirac} , the regime corresponds to electron transport, because the carriers in the graphene channel are electrons; when V_{gs} is smaller than V_{Dirac}, holes dominate in the channel transport characteristics. We can thus see that the on/off ratio in this graphene FET is very low (please note that the different V_{ds} branches are shifted up from one another in order to differentiate one from another. We should thus compare the relative difference between the maximum and minimum current I_{ds} for each V_{ds} as seen in figure 8).

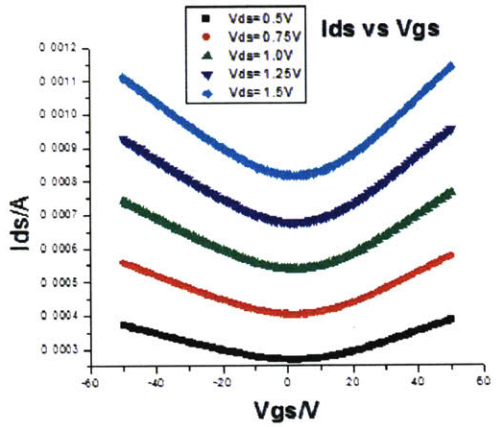

Figure 8 Sketch of source-to-drain current I_{ds} in a graphene FET versus backgate bias voltage Vgs, at different Vds values. please note that the different Vds branches are shifted up from one to another in order to differentiate each from the others.

➢ Lack of Current Saturation

There is no current saturation in large-area pristine graphene. In ordinary MOSFETs, the drain current saturates as the drain-to-source voltage increases to some point. Taking the example of silicon, figure 9 shows the linear region and the saturation region of the output characteristics silicon MOSFETs[20].

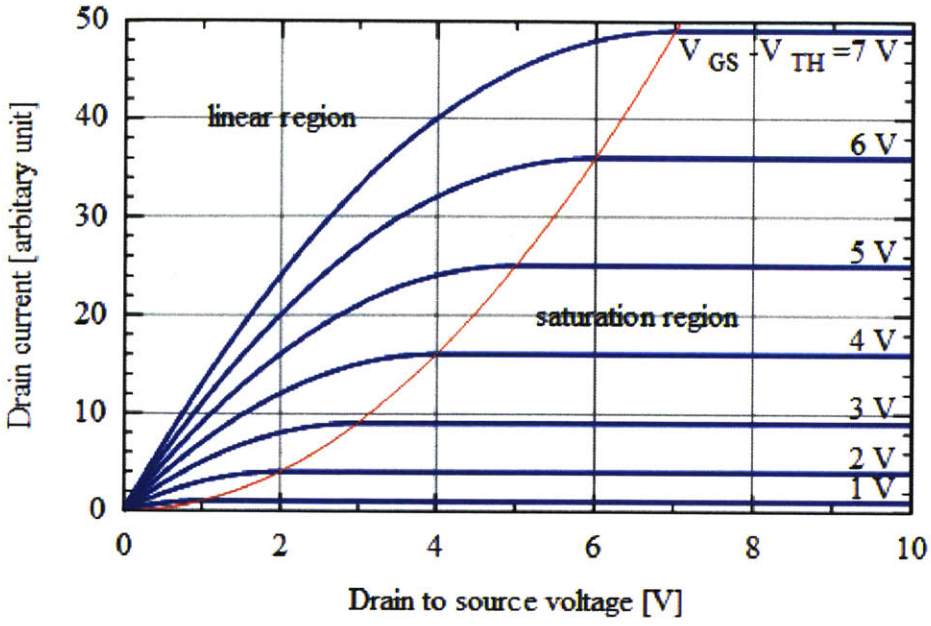

Figure 9 Sketch of the output characteristics of silicon MOSFETs at different values of the gate bias, in both the linear region and the saturation region[20]

However, in graphene FETs, we cannot find any signs of current saturation. Figure 10 is an example of the output characteristics in a graphene FET at different values of backgate bias voltage.

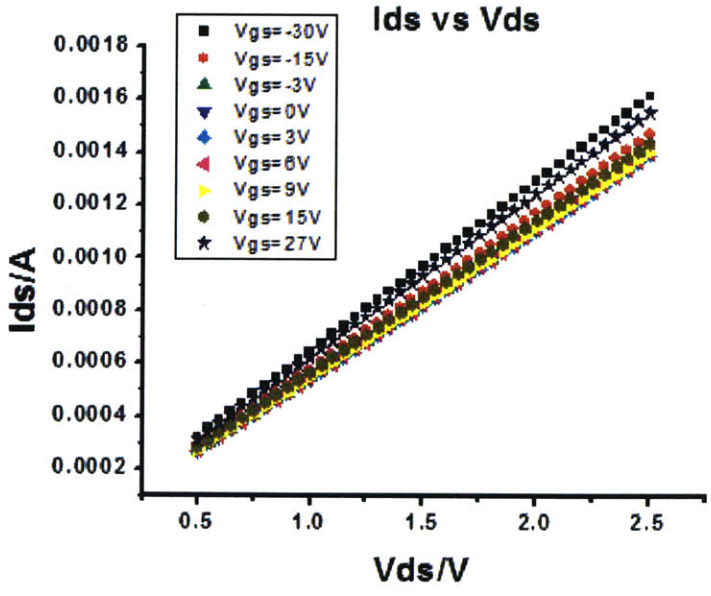

Figure 10 Sketch of the output characteristics of a graphene FET at different values of backgate bias voltage.

Why is current saturation important? First of all, the intrinsic gain, which is an important figure of merit for mixed-signal circuits, depends sensitively on the saturation region[12]. The intrinsic gain G_{int} can be expressed as

$$G_{int} = \frac{g_m}{g_o},$$

where the g_m and g_o represent the transconductance and output conductance of MOTFET's, respectively.

$$g_m = \left.\frac{\partial I_{ds}}{\partial V_{gs}}\right|_{V_{ds}=const,}$$

$$g_o = \left.\frac{\partial I_{ds}}{\partial V_{ds}}\right|_{V_{gs}=const,}$$

In the saturation region, the transconductance g_m reaches its maximum value, while the output conductance g_o reaches its minimum value. And therefore the intrinsic gain G_{int} maximizes itself only in the saturation region [12].

Secondly, in radio frequency devices, the current-gain cut-off frequency f_T also peaks in the saturation region. The current-gain cut-off frequency is the frequency at which the small signal current gain drops to unity. f_T is a widely used figure of merit to assess the suitability of MOSFETs for high-frequency mixed-signal applications. f_T can be expressed as follows[11].

$$f_T = \frac{1}{2\pi(C_{gs}+C_{gd})\frac{[1+g_{ds}(R_S+R_d)]}{g_m}+C_{gd}(R_S+R_d)},$$

where C_{gs} is the gate to source capacitance, C_{gd} is the gate to drain capacitance, g_{ds} is the drain conductance, R_s and R_d are source and drain series resistance respectively. For a similar reason as the intrinsic gain analysis, the cut-off frequency f_T reaches a maximum value when the transconductance g_m reaches its highest value, while the output conductance g_o reaches its lowest value. It is only in saturation region that these conditions can be satisfied [12].

A significant metric for power electronics is the power-gain cutoff frequency f_{MAX}, which is closely related to the current gain cutoff frequency f_T . f_{MAX} can be expressed as follows[21][22].

$$f_{MAX}=\frac{f_T}{2}\sqrt{\frac{1}{g_o(R_g+R_i)}}$$

where the R_g is the gate resistance and R_i is the input resistance (lumped representation of the distributed channel resistance). When operating in current saturation region, the f_T reaches its maximum value and output conductance $g_o$also reaches its lowest value. Therefore, we can find that the power gain cutoff frequency f_{MAX} is maximized only when the device is operated in current saturation region.

1.4 Opportunities in Surface Functionalization on Graphene

Although graphene is one the most chemically inert materials, chemical functionalization on its surface promises new opportunities for manipulating its electronic properties and for modifying its atomic structures[23]. It will also advance our understanding of mechanisms for graphene's interaction with its environment. Graphene is a true two-dimensional semimetal; every carbon atom in single layer graphene is exposed to its environment. Therefore, the surface functionalization in graphene can significantly change its physical and chemical properties. There are several motivations for these efforts in both theoretical and experimental research:

i. Band structure engineering, especially the band gap opening[23];
ii. Piezoelectricity engineering[24];
iii. Passivation and protection of graphene nanoribbon edges[25];
iv. Potential use of graphene for hydrogen and halogens storage[23];
v. Decoration of defects in graphene[26];
vi. Cracking graphene to create nanostructures in desired shapes, etc[27].

In this study, we only focus on the investigation of bandgap engineering and piezoelectricity engineering in graphene through chemical functionalization.

➢ Bandgap Engineering

Pristine graphene is a sp^2-hybridized carbon network in two dimensions, with a zero bandgap [28]. Each carbon atom has six electrons. Two of them are core electrons, occupying 1s states. They are bound tightly to the nucleus and do not participate in binding with neighboring carbon atoms. The other four electrons are valence electrons. Two of them occupy 2s states, two of them sit in 2p states. When carbon atoms are packed together to form graphene, the two 2s orbitals and two 2p orbitals interact and mix with each other to form three in-plane covalent bonds (σ bonds) through sp^2 hybridization[28]. Each atom has three nearest neighbors. These strong σ bonds contribute to graphene's outstanding mechanical performance. And also a delocalized electronic state (π bond) is created perpendicular to the graphene plane, which contributes to its excellent transport properties. Figure 11 shows schematics of the bonding structures in graphene.

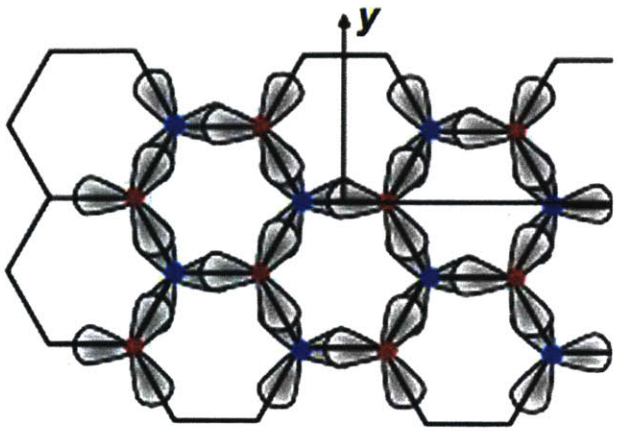

Figure 11 Schematic of the σ bonds between neighboring carbon atoms in graphene[29]

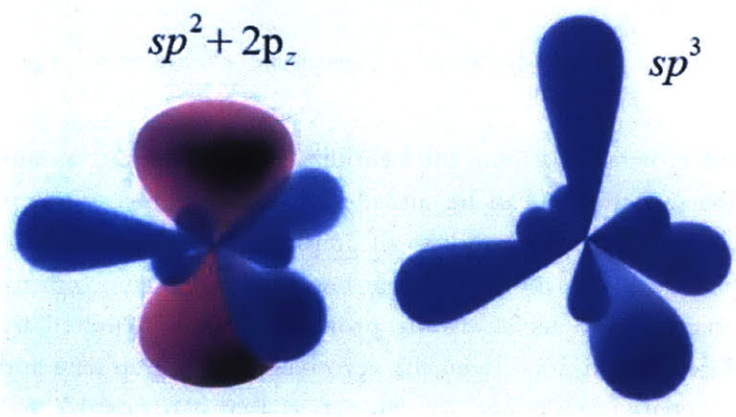

Figure 12 A schematic of the electronic bonding configuration of sp2 and sp3 hybridization, the $2p_z$ orbital is pink [30]

When carbon atoms in graphene interact with other chemical species, their electronic bonding structures can be modified. There are two types of surface functionalization: covalent and non-covalent bonding[31]. In covalent functionalization, covalent bonds will be formed between carbon atoms and other species. In non-covalent functionalization, van der Waals bonds bridge carbon atoms and the functioning species. When covalent functionalization occurs, sp^2 hybridization will be transformed into sp^3 configurations to some extent [31]. For example, by exposing graphene to a hydrogen plasma, hydrogen atoms form covalent bonds with graphene and become located on alternate sides of adjacent carbon atoms[23]. This fully hydrogenated graphene is named graphane, as shown in figure 13. It is worth to note that one hydrogen atom is needed to satisfy the π electron.

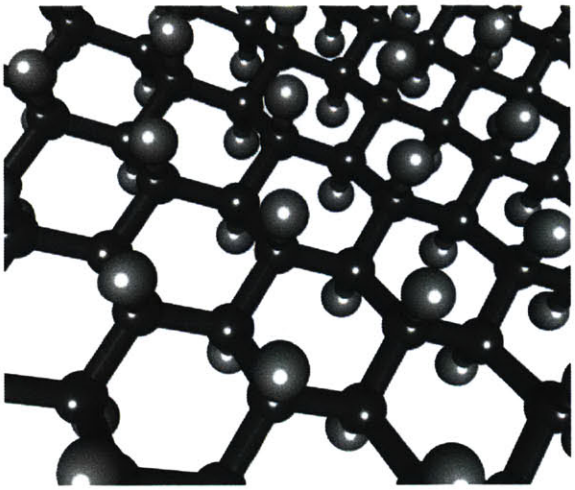

Figure 13 Schematic of atomic structures of graphane, i.e. fully hydrogenated graphene[32]

One consequence of transforming the hybridization state of carbon atoms from sp^2 into sp^3 (figure 14) is that a bandgap can be introduced in the highly conductive graphene[23]. It is theoretically calculated that the bandgap of graphane (fully hydrogenated graphene) can reach up to 5.4 eV[33]. What is more, it is further experimentally confirmed that hydrogenated graphene is reversible and its electronic properties could be tuned by controlled hydrogen adsorption and desorption[23]. Given the zero bandgap of graphene and the large bandgap of graphane (hydrogenated graphene), we can expect that it is possible to engineer the bandgap over a wide range by tuning the hydrogen coverage[34]. Fluorine is also exciting for a variety of applications due to its functionality as increasing hydrophobicity, reducing surface energy, and it is useful in bio-applications[35], [36]. However, both of these dopants are destructive to graphene, and will degrade its carrier mobility. Chlorine is also a very promising material to functionalize graphene. Theoretical works predict that by exposing both sides of graphene to chlorine it is possible to open a bandgap up to 1.3 eV [37]. Chemical functionalization of graphene, especially by hydrogen, fluorine and chlorine, has shown fascinating results, such as doping, edge passivation and widening of the bandgap of the resulting material [38][39]. However, how to functionalize graphene in a controlled way and to characterize it, without creating too many defects is still a challenge. In this thesis, we will mainly focus on the study of the chlorination in graphene.

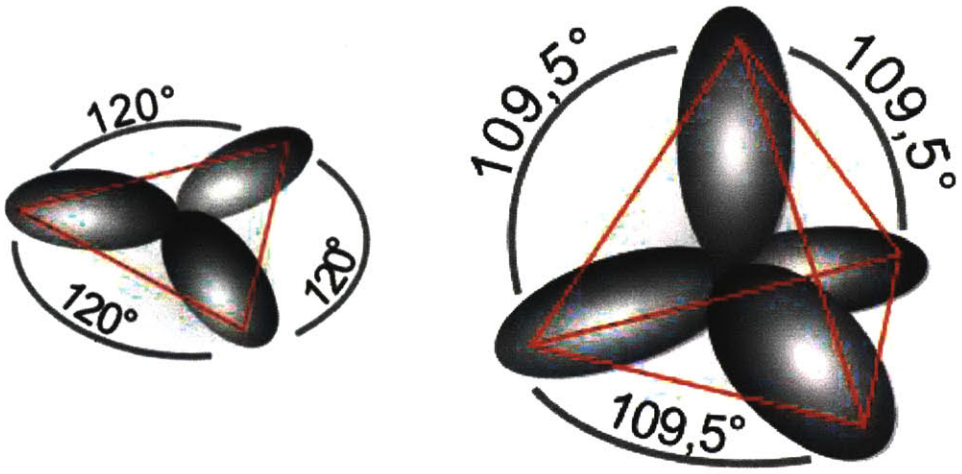

Figure 14 Schematics of carbon sp2 (left) and sp3 (right) electron orbitals [40].

- **Piezoelectricity engineering**

The piezoelectric effect is a reversible process in which an applied external electrical field can result in an internal mechanical strain in some special materials. Meanwhile, an applied mechanical force can also lead to the generation of piezoelectric charge in the material[41]. This approach is widely used in piezoelectric sensors, atomic force microscopes, scanning and tunneling microscopes etc. An essential characteristic for piezoelectric materials is the lack of inversion center in their crystal structures, for example, many piezoelectric materials have the wurtzite structure[24]. Unfortunately, graphene belongs to a centrosymmetric point group, and thus is not an intrinsic piezoelectric material. However, theoretical work shows that it is possible to engineer piezoelectricity into graphene nanostructures through surface functionalization[24]. The reason is that selective adsorption of other chemical species on one side of a graphene layer can break its inversion symmetry. The calculations for various types of strains are summarized in the figures below[24].

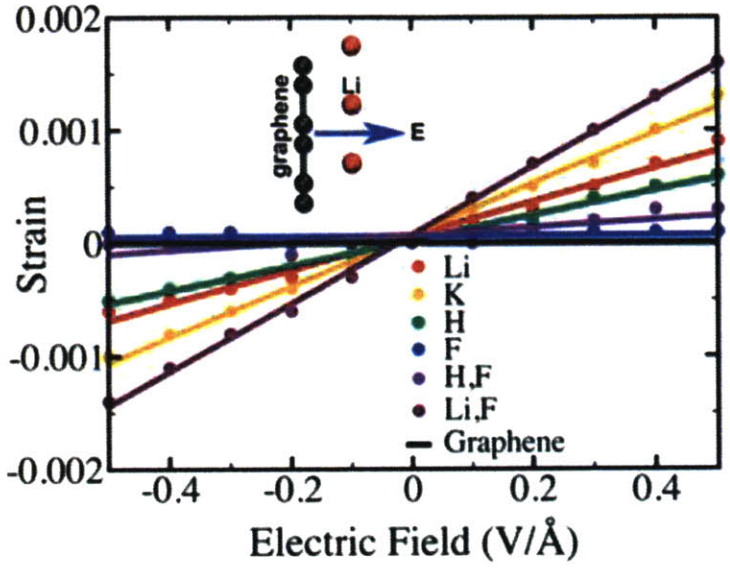

Figure 15 The illustration shows how an applied perpendicular electric field can produce strain in a surface functionalized graphene. The inset shows the strain resulting from Li surface functionalization. [24]

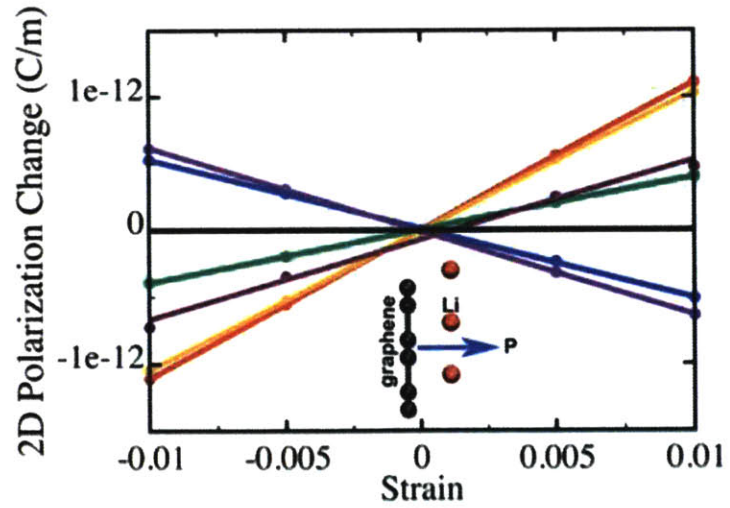

Figure 16 The illustration shows that how an equibiaxial in-plain strain on a graphene layer can induce a change in the polarization perpendicular to the graphene plane. [24]

Surface functionalization of graphene shows a promising way to create two-dimensional piezoelectric devices. What is more, it is demonstrated that graphene under strain can produce a pseudo-magnetic field up to 300 Tesla, as indicated in figure 17[42]. This fact provides a new avenue to generate quantum Hall effect without a real magnet. And the possibility to engineer strain in 2D graphene through the piezoelectric effect by surface functionalization, could facilitate the development of new devices based on quantum Hall effects, such as infrared detectors and metrology with super precision (the Hall conductance at each Landau level plateau is precisely integer times of $\frac{e^2}{h}$) etc. Furthermore, piezoelectric effects in graphene could perhaps be used to dynamically control motion and deformation in nanostructures[24].

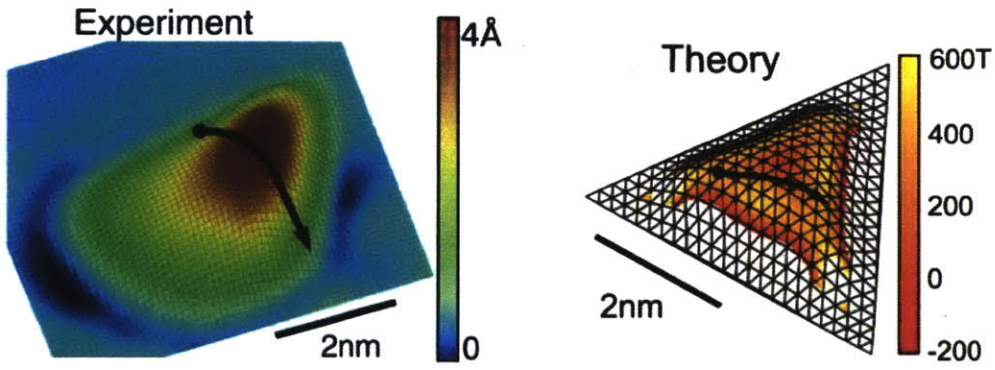

Figure 17 The left part shows STM topography of a graphene nanobubble with strain. The right figure shows the theoretical result of the pseudo-magnetic field color map generated in the graphene nanobubble. [42]

Objective of this Thesis

The extremely rapid and exciting development of graphene has attracted tremendous interest. Surface functionalizations, together with device fabrication, promise a powerful tool to engineer graphene's electronic properties and to facilitate its applications in future electronics. It is of critical importance to find a way to open a sizeable band gap in the graphene band structure, without sacrificing its extraordinary high mobility. In the meantime, it is also interesting to find out the possibility to build piezoelectricity in graphene to dynamically control its deformation at nanometer scale. In particular, in this thesis we will focus on investigating how chlorination in graphene changes its electrical and physical properties by different characterization methods. A schematic picture of reaction mechanism in chlorination will be proposed and discussed. Hydrogenation and fluorination will also be conducted and analyzed in comparison, looking for similarities and differences between the various doping agents (Cl, H and F). We will demonstrate that the controllability and high mobility preservation in chlorinated graphene are unique advantages over other functionalization approaches.

Chapter 2 Fabrication of Graphene-based Field Effect Transistors (FETs)

Graphene is endowed with many outstanding electrical and mechanical properties, which make it very promising as a semiconductor material for future electronics applications[43]. However, in order to harness its unique properties and to fulfill its potential in high-performance electronics applications, it is of critical importance to integrate and fabricate graphene-based transistors. In this thesis, we are aiming to understand how chlorination impacts the electronic properties in graphene, which necessitate the fabrication of devices with graphene as a channel material. Both exfoliated graphene and CVD-grown graphene are investigated. Chlorine plasma is used to functionalize the graphene channel of the FETs we fabricated. Hydrogenation and fluorination are also analyzed as functionalization approaches, because they can also interact strongly with graphene and modify its structure. This chapter presents the process of sample preparation and lithography for device fabrication. We start by introducing the method of exfoliating HOPG graphene and transferring CVD graphene onto a SiO_2/Si substrate, since by carefully choosing the thickness of SiO_2 layer we can optimize graphene's optical contrast under the microscope[18]. In the following section, photolithography and electron beam lithography are discussed and we will explain why graphene is compatible with the planar processing of silicon technology.

2.1 Graphene Sample Preparation

➢ Exfoliation of HOPG Graphene

Presently, mechanically exfoliated graphene has shown the best quality, compared with the CVD-grown graphene and epitaxial graphene on silicon carbide[1]. To get an exfoliated graphene flake, we followed the "Scotch-tape" method initiated by the Geim Group[1]. The process is summarized in the following figure.

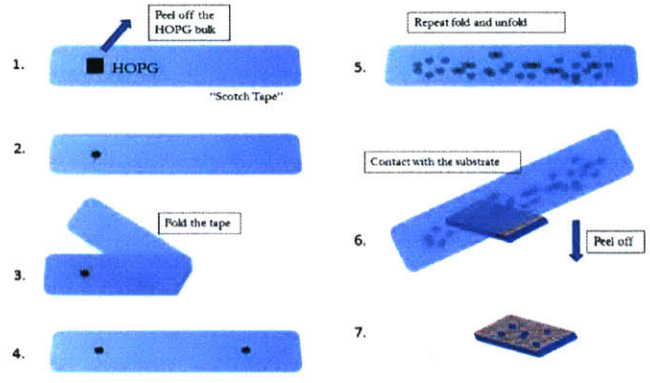

Figure 18 Schematic of the exfoliation process of HOGP-based graphene

Following figure 18, first, the HOPG bulk material was cleaved off and we put the clean and shining surface in contact with scotch tape, so that we have a platelet of HOPG on the tape. However, the platelet is usually quite thick. Next, by repeatedly folding and unfolding the tape, we can get thinner and thinner graphene flakes. When the HOPG flakes left on the tape seems very light, gently press the substrate onto the tape and peel off thin flakes.

Under the optical microscope, we can identify few-layer graphene flakes, which have a light pink color. Figure 19 shows an example of the graphene images. There are some tape residues left on the substrate in Figure 19, as shown below. By annealing at 300 ℃ for two hours, we can get rid of most of the residues.

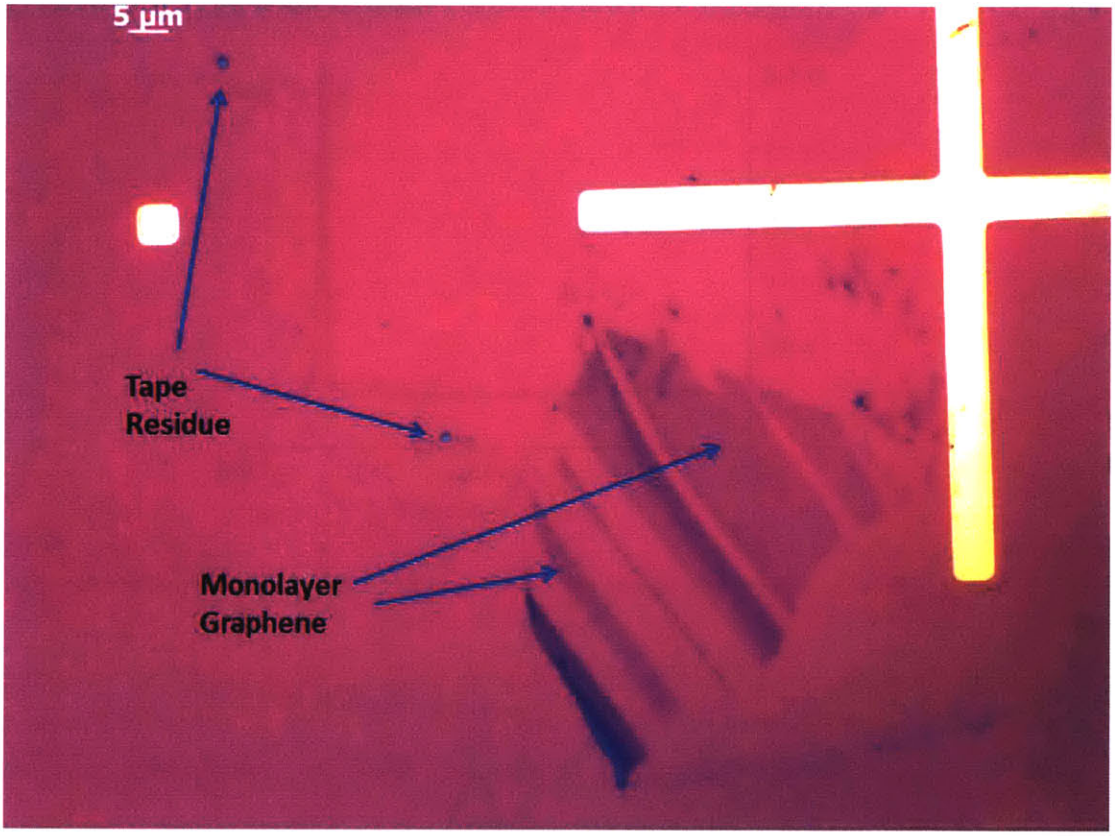

Figure 19 Optical images of monolayer graphene flakes

The reason that atomically thick graphene can be identified by an optical microscope is the interference between the graphene layers and the oxide layer of the substrate. A specific thickness of the SiO_2 layer is carefully chosen so that the contrast of the few additional carbon atom layers on top of the SiO_2 layer is maximized[18]. The substrates used in our experimental studies are a 300 nm SiO_2 layer grown on highly doped bulk silicon, which is commonly used at the present time to maximize the optical contrast of graphene flakes.

The number of graphene layers cannot be determined by optical images alone. We did further Raman characterization to differentiate single layer, double layer and triple layer graphene from one another, as described below[28][44].

A typical Raman spectrum of monolayer graphene is shown below in Figure 20. Using a wavelength of 532nm, a Lorentzian profile in the G' peak centered at ~ 2680 cm^{-1} is observed, with G'/G intensity (integrated area under the Raman line) ratio of about 4 is the signature of monolayer graphene[28][45]. More details about the graphene's Raman spectroscopy will be discussed in the next chapter.

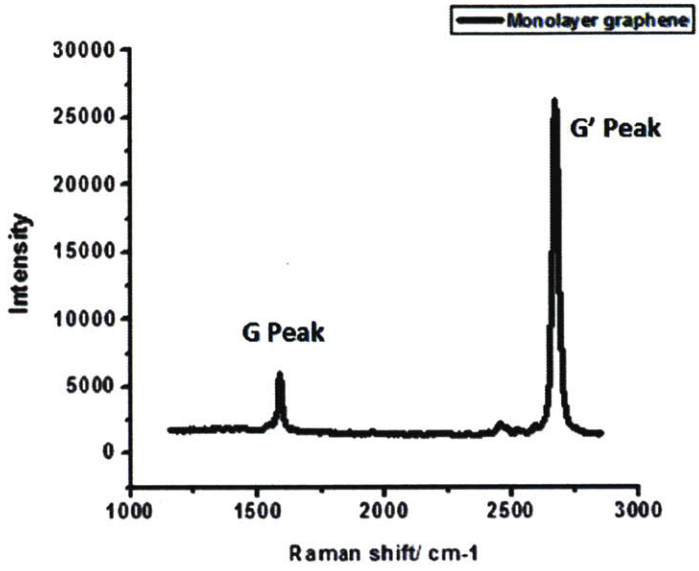

Figure 20 Raman spectrum of a monolayer graphene flake. The G peak is centered at ~1580 cm-1, and the G' peak is centered at ~ 2680 cm-1.

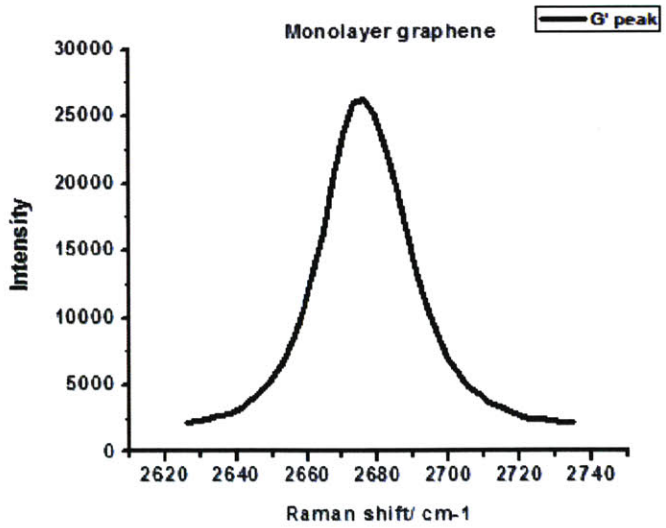

Figure 21 The G' peak in the Raman spectrum of monolayer graphene

The Raman signatures for AB-stacked bilayer graphene are illustrated in the figure 22. The G' peak is not a single Lorentzian profile, but a superposition of four Lorentzian peaks. In addition, the G'/G band intensity ratio and the linewidth of G' band for bilayer graphene are different from monolayer graphene. [28], [44], [45]

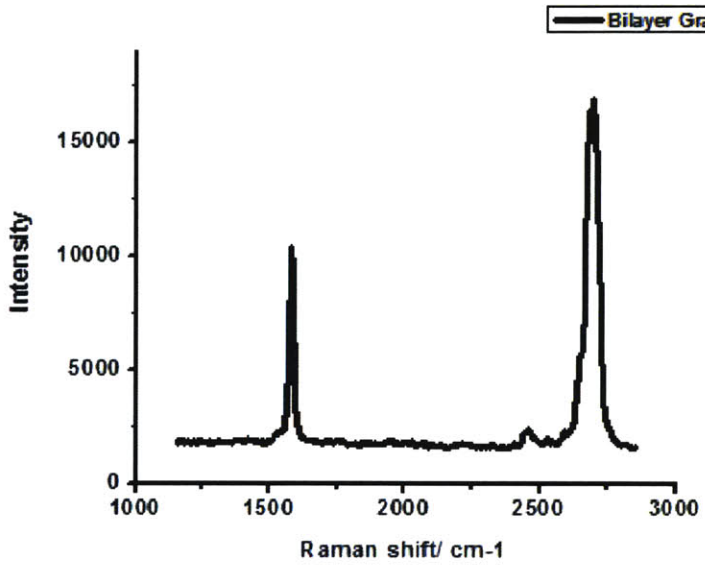

Figure 22 Raman spectrum of a AB stacked bilayer graphene

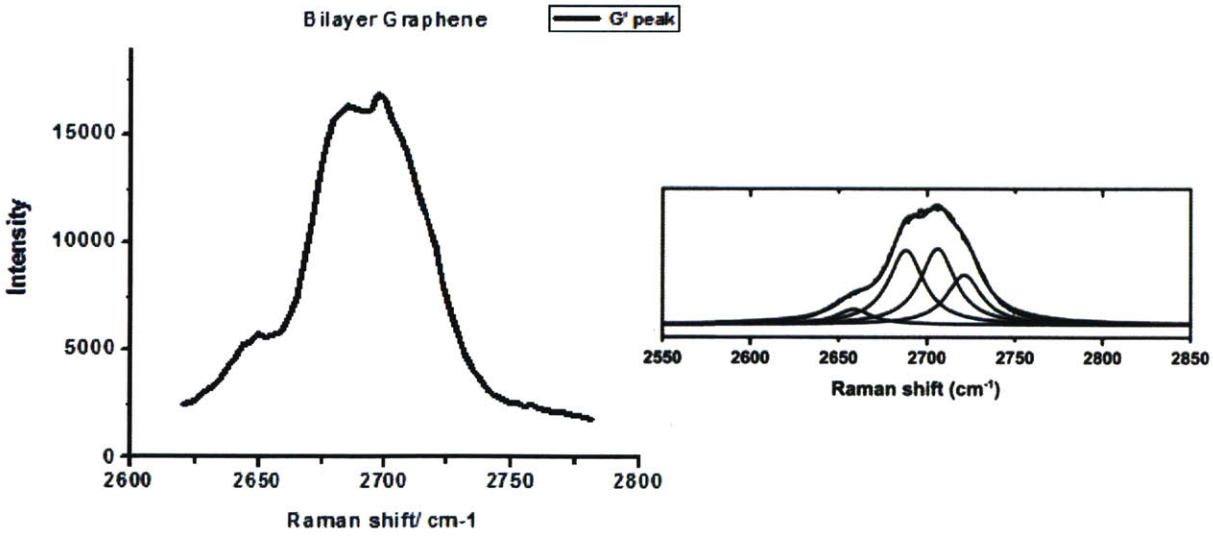

Figure 23 The G' peak in the Raman spectrum of bilayer graphene (left). It can be fitted by four Lorentzian peaks (right).[45]

Trilayer graphene is more complicated due to the stacking order. There are two kinds of stacking that can be found in trilayer graphene: ABA and ABC stacking as shown in figure 24.[46]

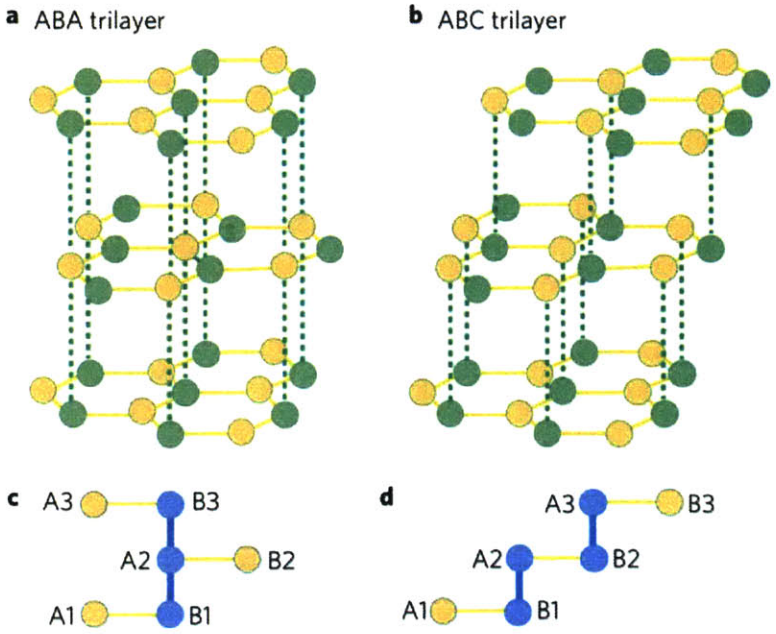

Figure 24 Atomic structures of ABA ((a) and (c)) and ABC ((b) and (d)) stacking in trilayer graphene[46]

The Raman spectra of ABA and ABC trilayer graphene are different from each other, allowing us to distinguish between these two layer stacking arrangement. Figure 25 below shows a typical result for the Raman spectra ABA-stacked trilayer graphene[45].

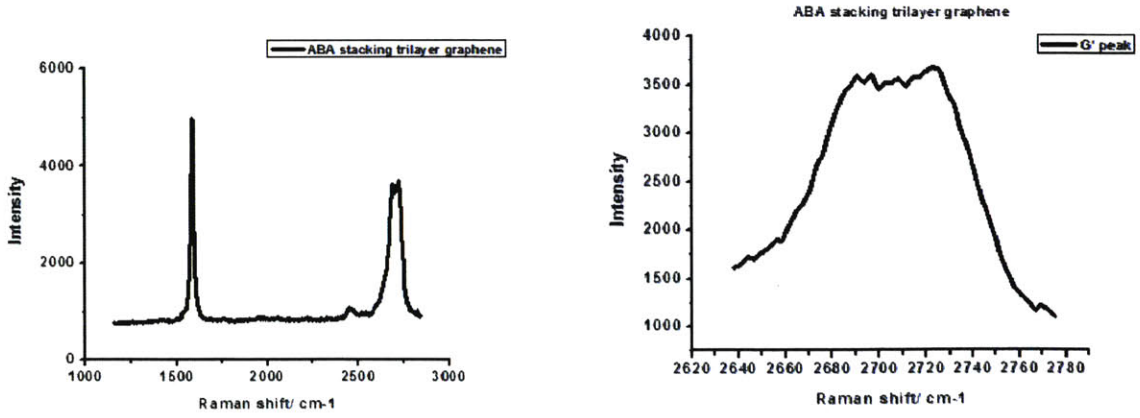

Figure 25 Raman spectrum of ABA-stacked trilayer graphene and the zoom-in figure of the G' peak spectrum

A typical Raman spectrum of ABC-stacked trilayer graphene is different, as indicated by comparing the spectrum for the ABC stacking in Figure 26 with the ABA stacking in Figure 25.

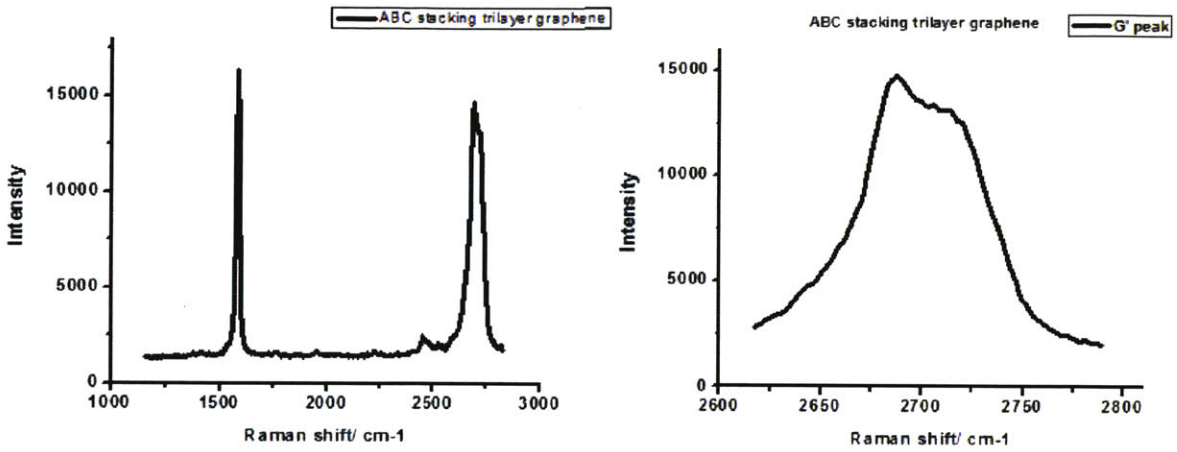

Figure 26 The Raman spectrum of ABC-stacked trilayer graphene and the zoom-in figure of the G' peak

➢ Chemical vapor deposition (CVD) grown Graphene

In this study, we also used CVD-grown graphene for X-ray photoelectron microscopy investigation. CVD graphene was grown on a copper foil having a thickness of 25 μm. A wet-transfer method was used to transfer graphene from copper to SiO_2/Si substrates[47]. The figure below illustrates this five-step process.

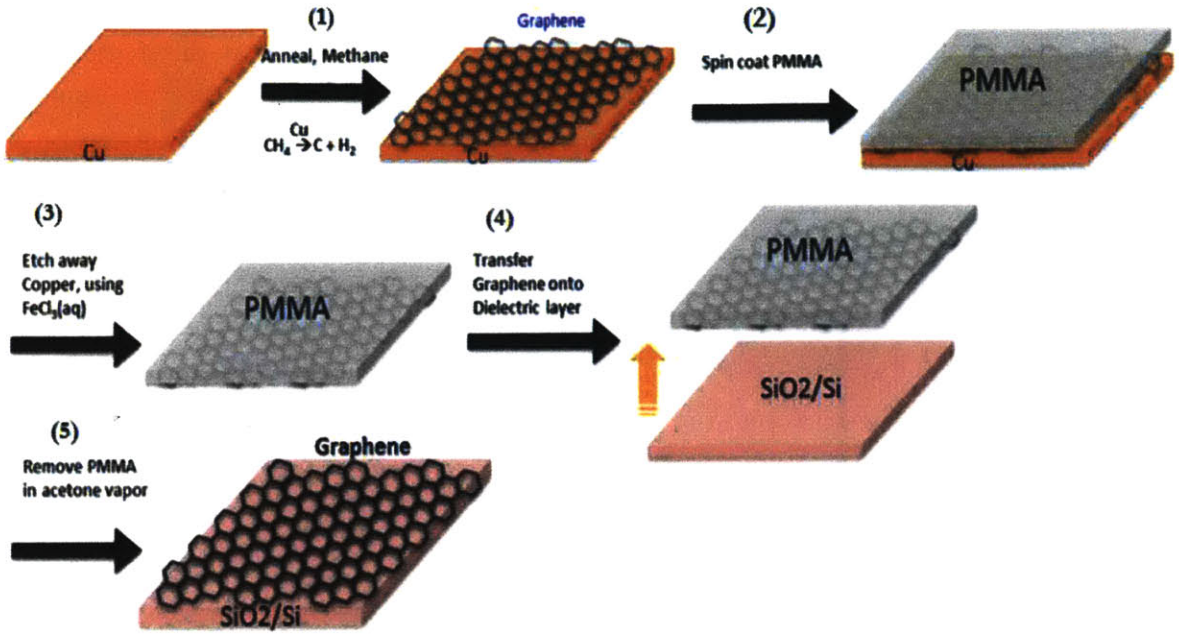

Figure 27 Illustration of wet transfer process for transferring graphene from copper to a SiO2/Si substrate

We grew graphene on a copper foil the by the decomposition of methane gas (1), and both sides of the copper foil were covered by graphene[17], [48]. We first etched away the graphene on one side of copper foil by oxygen plasma. And then we spun, at 2500 rpm for 60 seconds, a layer of PMMA on copper to protect the graphene (2). Then the PMMA/graphene /copper sample was baked at 140 °C in an oven (at 1atm) for 10 minutes. After that, we put the sample in a $FeCl_3$ (aq) solution to float for about 40 minutes to etch away the copper foil underneath (3). Next, we use glass to lift up the sample out of the $FeCl_3$ solution and we transfer it into a 10% HCl (aq) solution for about 20 minutes to wash away the Cl^-. And then by using the same technique, we transferred the PMMA/graphene into deionized (DI) water for cleaning the sample and we repeated this procedure 2-3 times, before finally transferring the sample onto the desired substrate: SiO_2/Si wafers (4). Next, we dissolved the PMMA layer in acetone vapor for about 20 minutes. After that, we rinse the graphene sample by using isopropyl alcohol and DI water (5).

2.2 Photolithography

In the case of large-area CVD graphene, we did photolithography to fabricate graphene-based FETs. Lithography is a process of creating patterns in the sample by information-carrying beams, such as photon, electron or ion beams. Photolithography makes use of photons and transfers the pattern from an optical mask to the sample surface [49]. The fabrication process of graphene FETs by photolithography is discussed here.

➢ Define Source and Drain Electrodes

The first step is to define contact electrodes on the SiO_2/Si substrates, even before transferring the CVD graphene onto the substrates. The reason for this is to minimize the damage to the graphene caused by the lithography process. Negative photoresist AZ 5214 was used for patterning. The procedure of defining electrodes on the substrates through photolithography is illustrated in Figure 28 below.

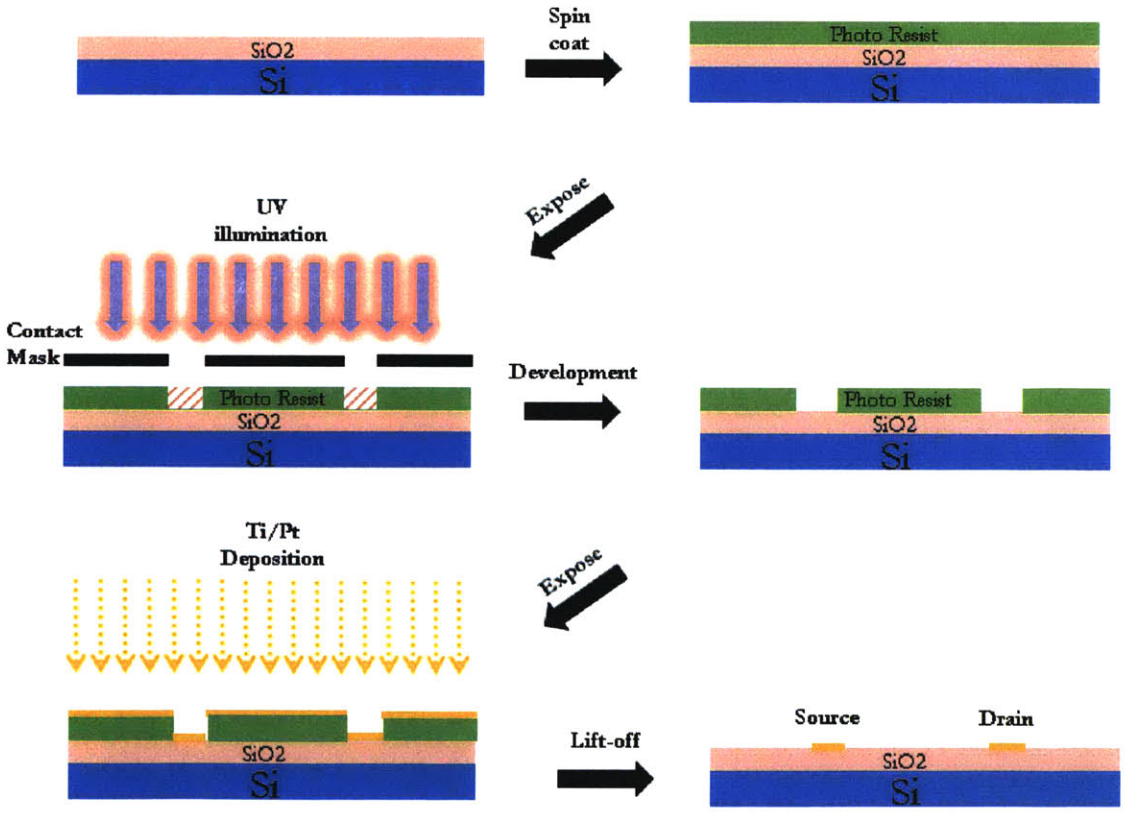

Figure 28 Schematic of the procedure of photolithography to define electrodes. No graphene sample is shown.

A contact mask was used to transfer the electrode pattern to the substrates. The pattern of the mask we used is shown below in Figure 29. The right hand part of the pattern shown in Figure

29 was used for Hall bar devices fabrication. Such Hall bars can be used for mobility and carrier concentration measurements.

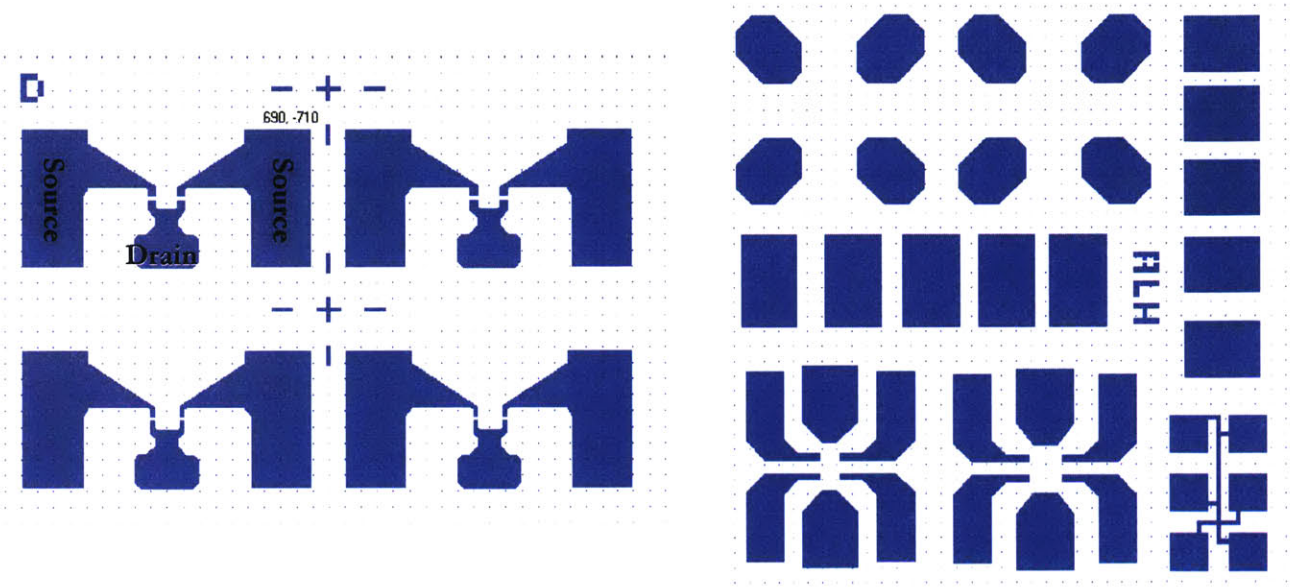

Figure 29 Pattern of the mask used for defining source and drain electrodes

➢ Transfer Graphene

After fabricating the contact electrodes, we transferred large-area CVD graphene onto SiO_2/Si substrates (Figure 30) by the method illustrated above (Figure 27).

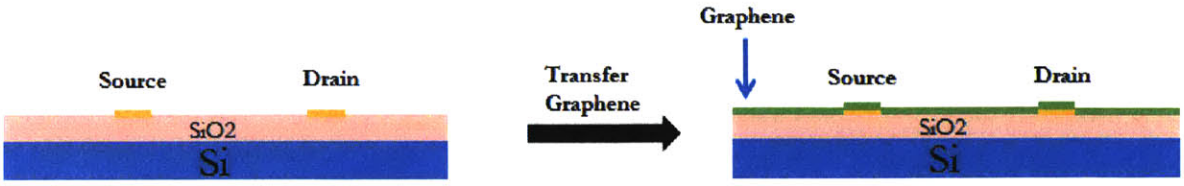

Figure 30 Transfer CVD graphene(indicated by green film) onto SiO_2/Si substrates fabricated with electrodes

➢ Mesa Isolation

After transferring graphene onto the SiO_2/Si substrates, all the electrodes were shorted together since graphene is an excellent conductor. Therefore, we did mesa isolation to separate and shape graphene into the required patterns. Figure 31 shows the process flow that was used.

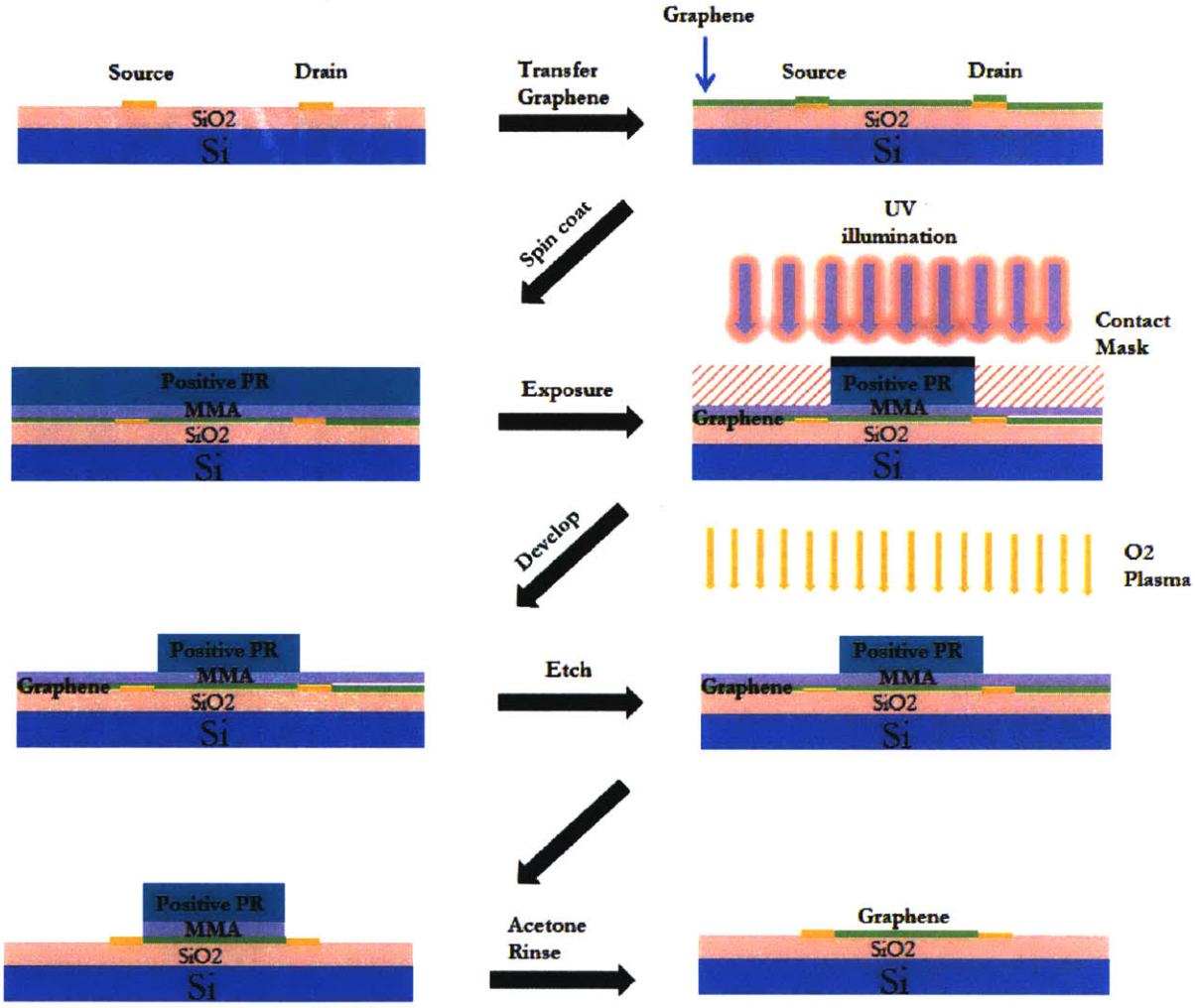

Figure 31 Illustration (sideview) of the process flow for mesa isolation of graphene

Positive photoresist OCG834 was used in this step to transfer the isolation pattern from the lithography mask to graphene. Before spin-coating this photoresist (PR) layer (OCG 834), we coated MMA as a buffer layer to facilitate the removal of OCG 834 when rinsing in acetone, since MMA can be easily removed in acetone. After development, we put the sample in an O_2 plasma etcher (Reactive Ion Etching, RIE) for 2 minutes to etch away the unwanted graphene. The blue features in shown in figure 32 are electrodes we pre-

patterned before transferring graphene. The green features are the patterned graphene layers.

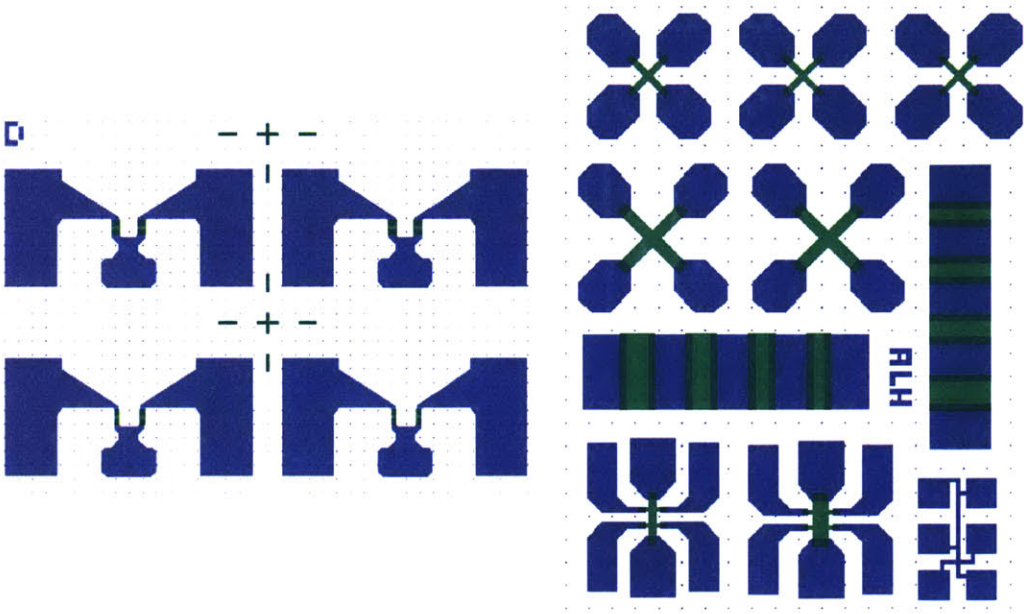

Figure 32 Pattern of the mask used for mesa isolation. The blue electrodes were patterned on the SiO2/Si wafer before transferring graphene. The green parts are the graphene regions that remain after isolation.

- **Back-gate**

In this work, the graphene transistors where gated through the use of a back-gate made of the heavily doped Si substrate. This allows the simple functionalization of the top graphene surface with Cl_2 gas. Figure 33 shows a schematic of such a back-gated graphene FET.

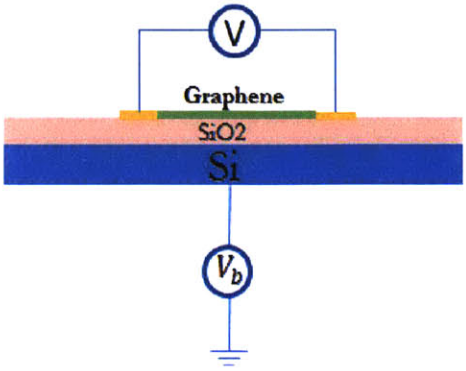

Figure 33 Schematic of a back-gated graphene FET.

2.3 Electron Beam lithography

For exfoliated graphene, we used electron beam lithography instead of optical lithography to fabricate the electrodes. Before transferring the graphene, we fabricated alignment marks on the substrates. And then we placed exfoliated HOPG graphene onto the substrates with marks. Figure 34 shows an example of the as-received samples.

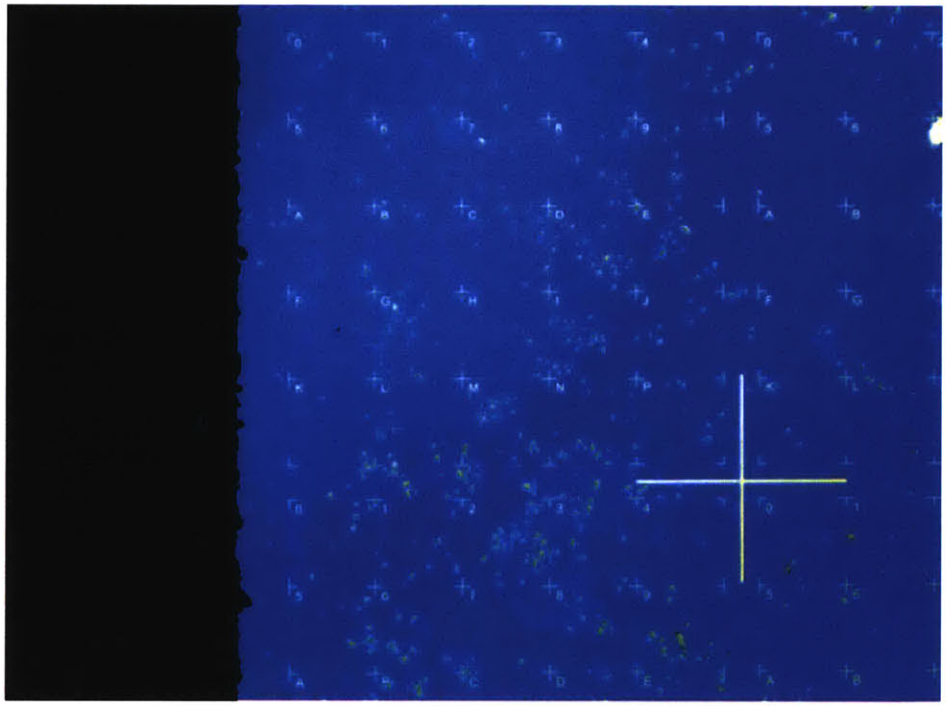

Figure 34 Exfoliated graphene flakes on a SiO_2/Si substrate with alignment marks. The labels "0", "1", "2" etc presents the alignment marks on the substrate that help us to locate the graphene flakes

After identifying the area of monolayer graphene, we used e-beam lithography to isolate the sample and pattern it into the desired shape. Take as an example, the exfoliated graphene flake shown in figure 35. In this case, we spun a layer of PMMA on the sample at 4000 rpm for 60 seconds. After exposure to the e-beam and the development of the PMMA, we created the desired pattern in the PMMA layer as indicated in the figure 36.

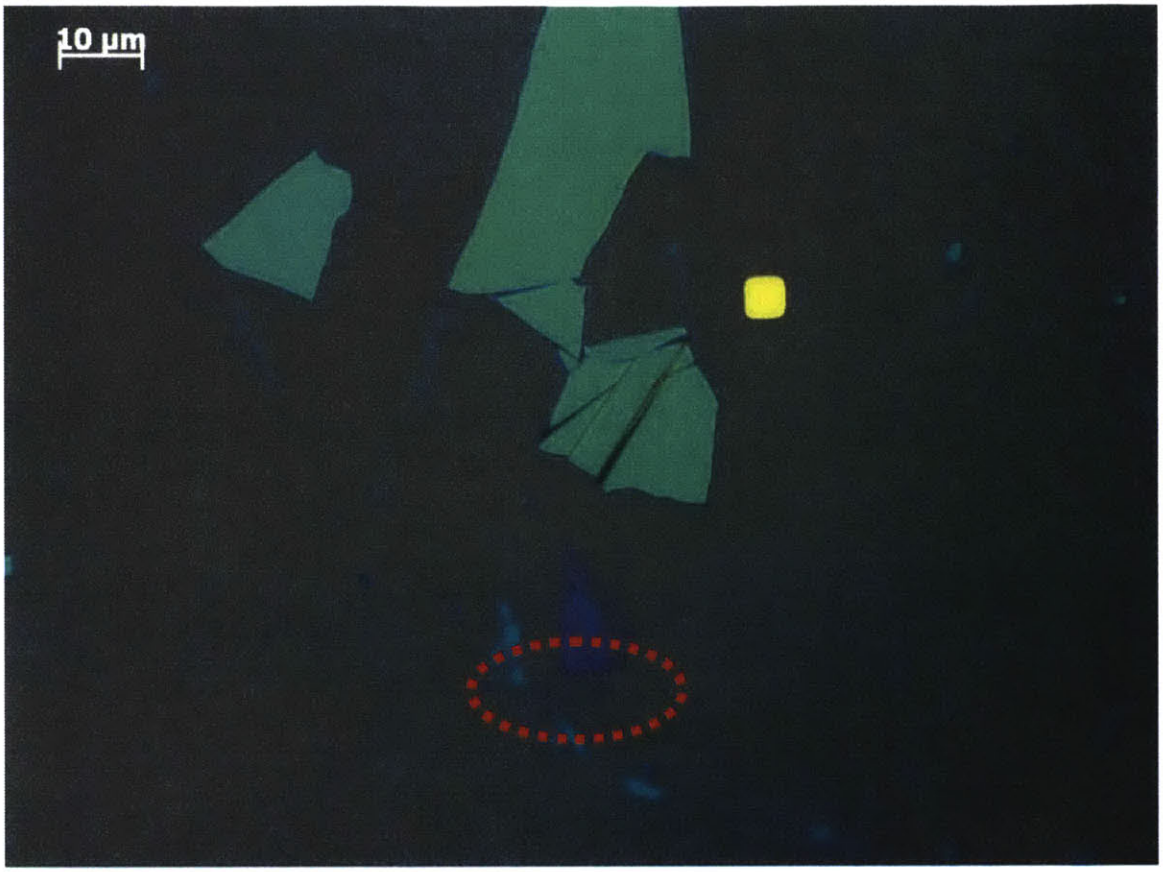

Figure 35 Optical image of exfoliated graphene flakes. The flake inside the red dashed circle is the one we intend to use in devices.

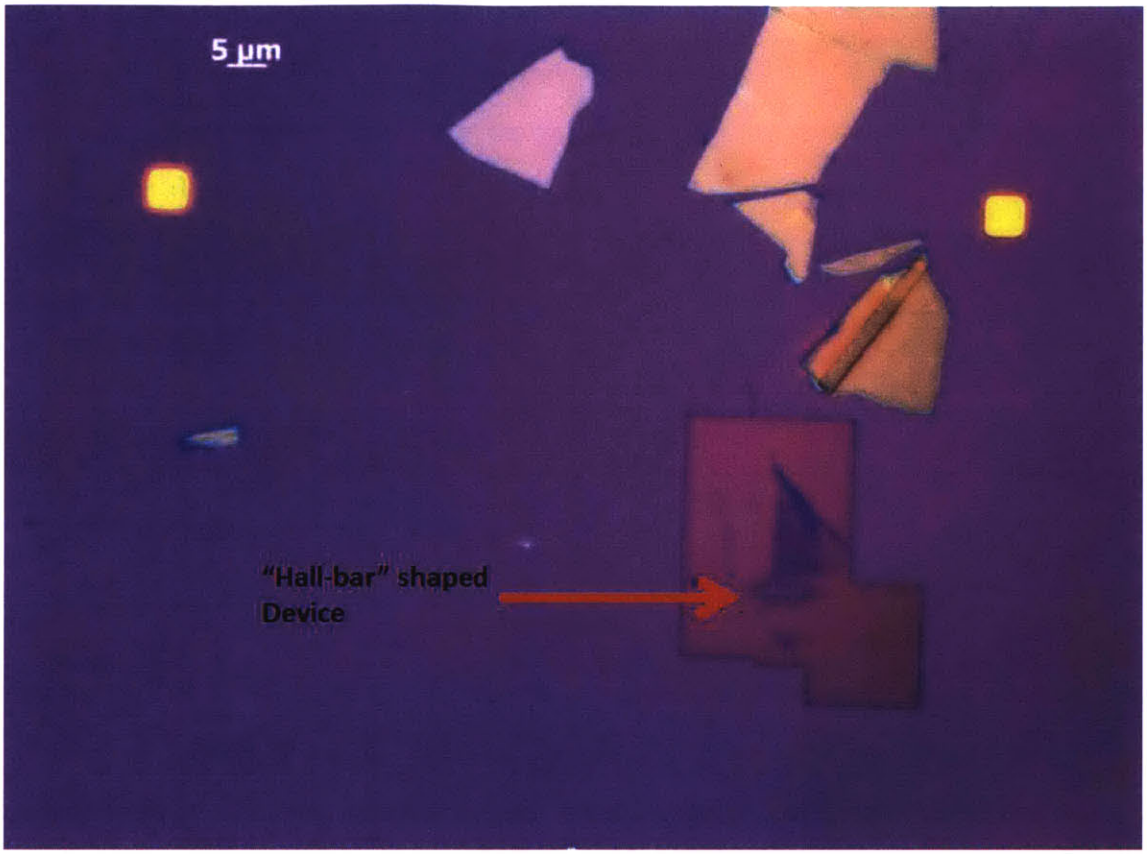

Figure 36 E-beam lithography for mesa isolation (after exposure and development). The Hall bar shaped area highlighted by an arrow is the region where the graphene was protected by the PMMA layer. In all the other areas, PMMA was removed so that the graphene is exposed to the dry etching.

A Hall bar pattern was protected in graphene with a PMMA layer. The rest of the graphene was exposed to oxygen plasma for 30 seconds, which removed the graphene everywhere except from the Hall bar area, as shown in figure 37.

Figure 37 Exfoliated graphene flake after mesa isolation

In the following steps, we defined the source and drain regions by e-beam lithography and deposited metal electrodes (figure 38). During the e-beam lithography, we used an exposure current of 120 pA. The field size is 150 μm and the dose chosen is 1500 $\mu C/cm^2$. After exposure, the sample was developed in the mixture solvent of Methyl isobutyl ketone (MIBK) and Isopropanol (IPA) (MIBK:IPA=1:3) for 90 seconds. Next, the sample was rinsed in IPA for one minute.

The metal deposited was Ti (4nm) on top of 30 nm Pt. The thin Ti layer served as an adhesion layer, since the Pt does not adhere to the graphene surface very well. The interaction between Ti and graphene is much stronger, and thus the electrodes become stickier to graphene surface. Here, we used the silicon substrate as a backgate. After this step, the graphene-based FET was finished and ready for measurement, as shown in figure 38.

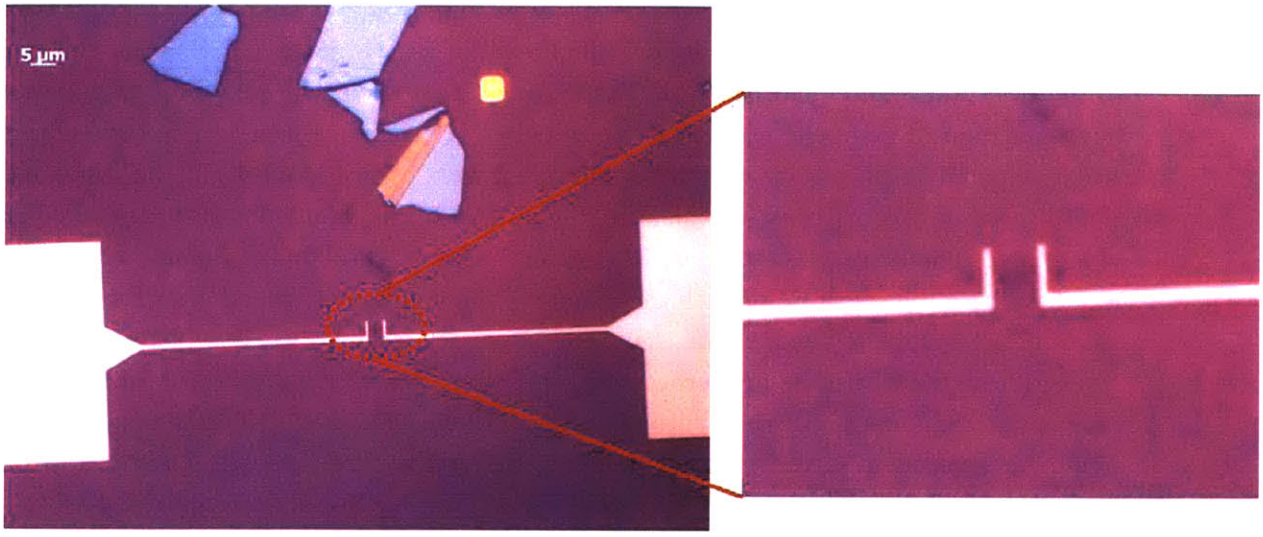

Figure 38 Exfoliated graphene FETs fabricated with source and drain by e-beam lithography (left), and a zoom-in picture of the device part (right).

Chapter 3 Graphene Chlorination

This thesis studied how the surface functionalization of graphene changes its electronic properties and band structure. In particular, we studied chlorination, fluorination and hydrogenation of graphene via plasma treatments. We mainly focused on graphene chlorination, and compared these results with those obtained with hydrogenation and fluorination. X-ray photoelectron spectroscopy revealed that chlorine atoms bonded with graphene, and the chlorinated graphene was quite stable under ambient conditions. Raman characterization indicated how the structure of the carbon network in graphene changed after functionalization. Chlorinated graphene field effect transistors were made and the subsequent measurements showed how the electronic properties and band structures were modified. A unique advantage of graphene chlorination over hydrogenation and fluorination is that chlorination via plasma treatment mostly preserved its high mobility, but at the same time it allowed control of its Fermi level and the preparation of controllable and effective bonding structures.

3.1 Experimental setups and Sample preparation

- **Experimental setups**

The chlorine plasma treatments were done in an Electron Cyclotron Resonance Reactive Ion Etcher (ECR/RIE, PlasmaQuest). We optimized both the ECR (electron cyclotron resonance) power and radio frequency (RF) power to control the reaction.

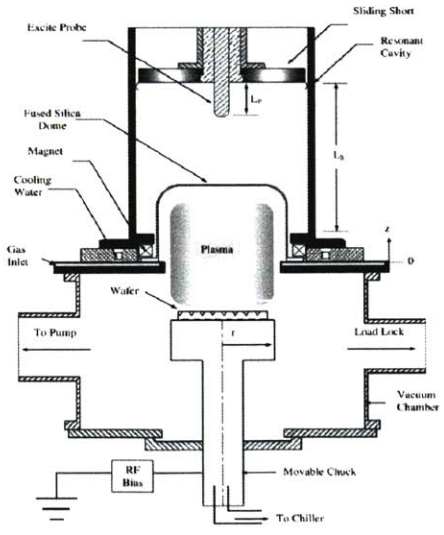

Figure 39 Schematic of ECR microwave plasma etching reactor[50]

Plasma was generated from the ECR plasma source in the chamber and accelerated towards the substrate by a divergent magnetic field. Electrons travel in a circular orbit when a perpendicular magnetic field is applied, due to the Lorentz force. If the pressure in the plasma chamber is low enough, the mean free path can be long enough for an electron to complete its orbit without scattering. When the magnetic field is applied at its resonance frequency (Larmor frequency), the electrons absorb energy from the magnetic field during each orbit. The electrons are, in this way, excited and gain enough energy to free themselves from the nuclei (Chlorine atoms in our case), which ionizes the gas and creates a plasma. This is the basic principle of an Electron Cyclotron Resonance (ECR) plasma etcher. It is easy to understand that at the same pressure and flow rate, the higher the ECR power, the higher is the density of plasma that can be generated in the chamber. Also, at the same ECR power condition, a higher the pressure in the etcher, and a higher plasma density can be produced. The figure below shows how the density of the plasma in the chamber changes as the pressure is increased.

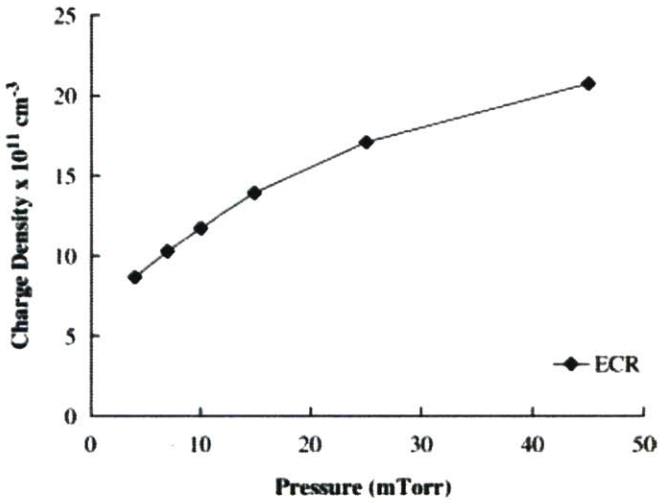

Figure 40 Plasma density increases as the pressure in the chamber is raised.[50]

At the same time that the plasma is generated, an RF generator in the etcher chamber induces a radio frequency signal towards the substrate. This RF signal creates a depletion region over the sample area, and thus the sample is (becomes) biased relative to the plasma. Therefore, the plasma is accelerated in the depletion region and gains kinetic energy to strike onto the sample surface[50]. In summary, the ECR power controls the density of the plasma generated in the chamber, while the RF power controls the kinetic energy of the plasma.

The temperature of the sample can be controlled by changing the chuck temperature, however in all our experiments we kept it at 25 °C. There are two different options to control the kinetic energy of the plasma: either by setting the RF power, or the RF bias. In this work, we are aiming to functionalize graphene with a chlorine plasma at relatively low energy, since we want

the surface reactions to be as gentle as possible, to not etch or damage the graphene. When trying to use a very weak RF signal, the RF power was too unstable to be controlled in a reproducible fashion. At the same time, we found the RF bias is much more controllable. The plasma presence can be seen as a light purple glow in the chamber, as shown in Figure 41.

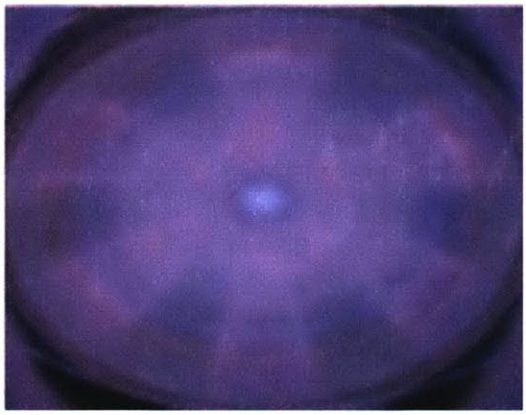

Figure 41 A photo of the plasma glow in the PlasmaQuest chamber [50]

Before each run, we used oxygen plasma to clean the chamber for 10 minutes. After that, the desired chlorine plasma recipe was run for 10 minutes to condition the chamber. In the following experiments, the flow rate of chlorine gas was 80 sccm. The pressure in the chamber was maintained at 20 mTorr. The ECR power, RF bias and treatment duration were carefully controlled to systematically analyze the reaction mechanisms.

➢ Sample Preparation

Both exfoliated graphene flakes and large-area CVD-grown graphene were investigated. The HOPG graphene were transferred onto a silicon wafer with 300 nm SiO_2 layer on top (graphene/SiO_2/Si). Single layer graphene was identified via an optical microscope, and further confirmed by Raman spectroscopy.

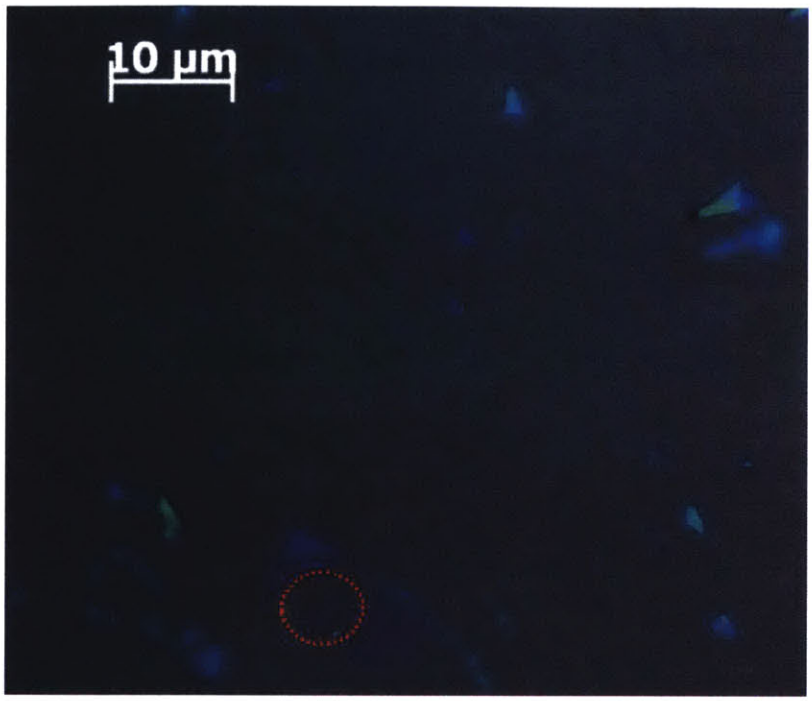

Figure 42 Optical image of one of the exfoliated HOPG graphene flakes.

Figure 42 shows an optical image of one of the exfoliated HOPG graphene flakes. Single layer graphene shows a light pink color under the microscope (in the incident white light). Figure 43 shows the Raman spectrum of this flake. The G peak centered at 1580 cm^{-1} indicates the carbon bonding signature. And the G' peak appears at around 2680 cm^{-1} with a symmetric Lorentzian profile, having a FWHM (full width at half maximum) of about 28 cm^{-1}.[28] The spectrum in Figure 43 is the typical Raman evidence for single layer graphene.

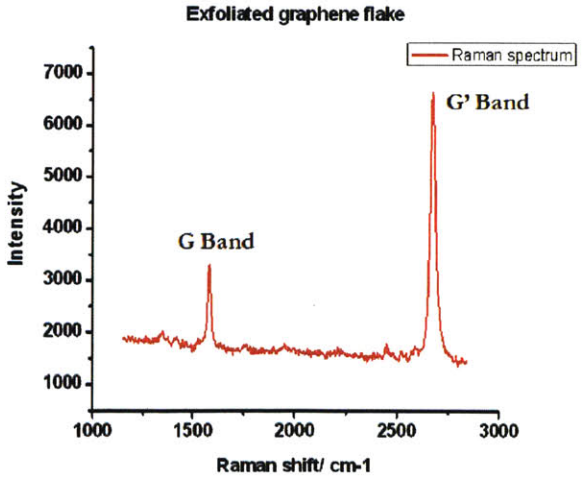

Figure 43 Raman spectrum of the exfoliated HOPG graphene flake.

Graphene grown by chemical vapor deposition (CVD) was produced by annealing copper foil in CH_4 gas at 1035 ℃. [17], [48] The foil was then cooled down to room temperature. The as-grown graphene was transferred onto a SiO_2/Si substrate by a wet process. PMMA (4% in anisole) was spun onto graphene/copper as a protection layer, at 2500 rpm for one minute, and the sample was then baked at 140 ℃ for 5 minutes. The foil was placed in a $FeCl_3$ (aq) solution for one hour to dissolve the copper. After baking in an oven at 140 ℃ for 10 minutes, we used acetone vapor to dissolve the PMMA layer. Figure 44 shows an optical image of the transferred CVD graphene.

Figure 44 Optical image of CVD graphene on a SiO_2/Si substrate

The quality of the CVD graphene layer was characterized by Raman spectroscopy, as shown in Figure 45.

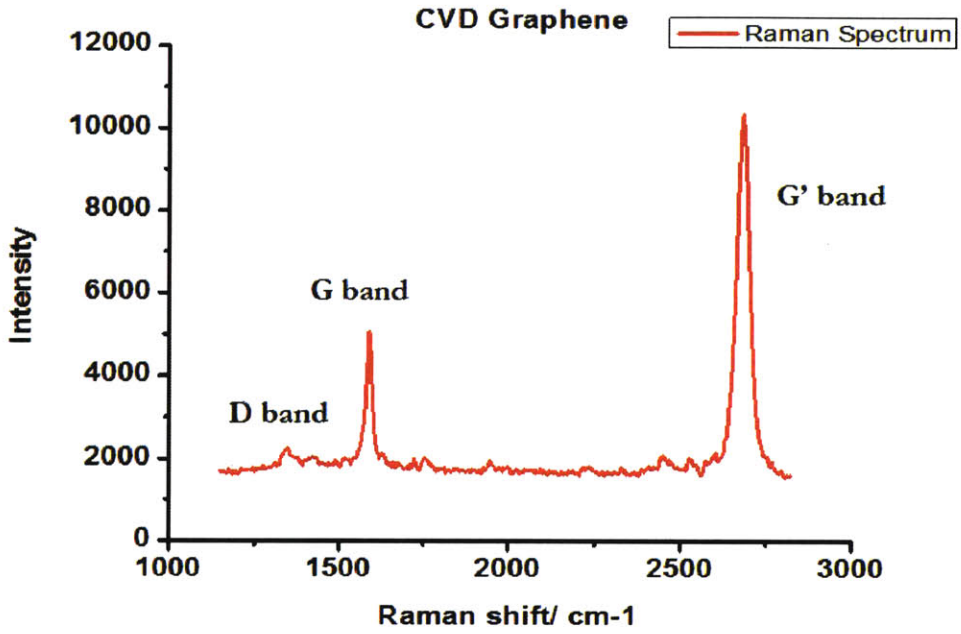

Figure 45 Raman spectrum of CVD graphene on SiO2/Si substrate.

Figure 45 shows that there is a weak D peak centered at around 1350 cm^{-1}, indicative of symmetry breaking due to defects. [28] We attribute this peak to the results of defects introduced by the transfer process.

3.2 Raman Characterization

Raman spectroscopy provides a useful sensitive, fast and non-destructive characterization tool for carbon-based materials [44]. Therefore, Raman spectroscopy has been widely used to exploit the structures and electrical properties of graphene, such as the stacking orders, layer number and doping levels etc [45]. Here, we characterized the impact of plasma chlorination on graphene, and observed dramatic changes in its atomic structure, as evidenced by the comparison of the Raman spectrum of the chlorinated sample with that for the pristine sample.

➢ **Raman spectrum in pristine graphene**

Figure 46 shows a typical Raman spectrum of pristine graphene before chlorination. The essential features of the graphene Raman spectrum in Figure 46 are the G peak and G' peak, centered at 1580 cm^{-1} and 2680 cm^{-1}, respectively.

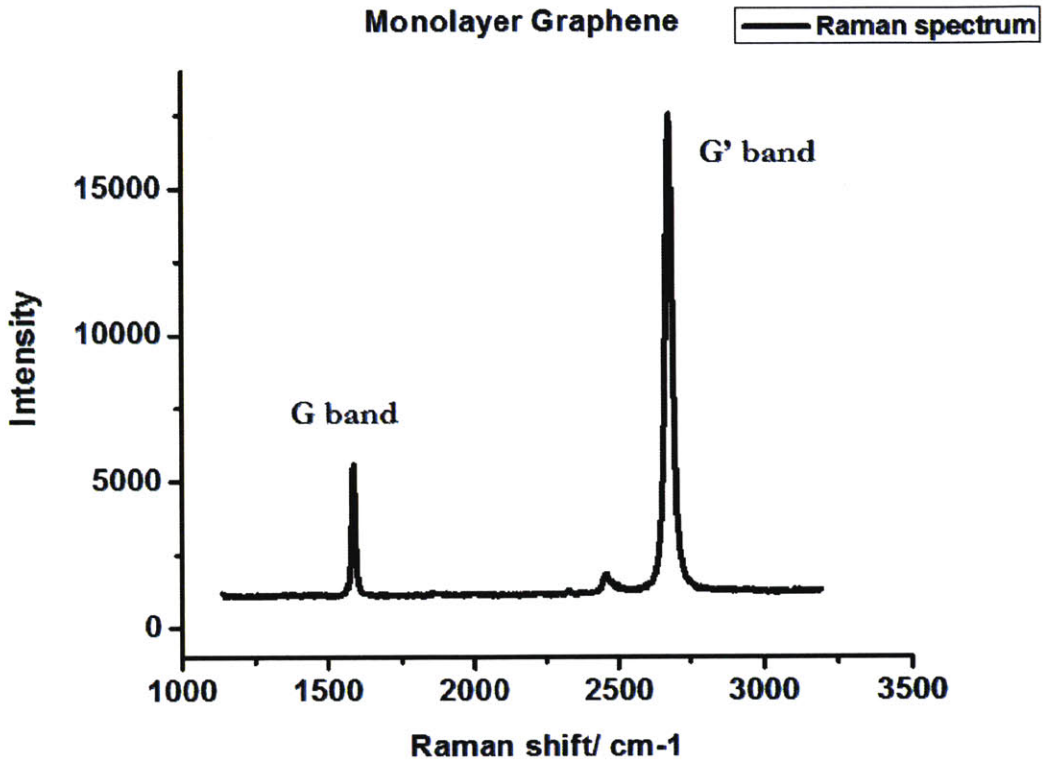

Figure 46 Raman spectrum of exfoliated HOPG monolayer graphene flake

The G band at around 1580 cm^{-1} originates from a normal first order Raman scattering process, corresponding to doubly degenerate optical photons at the Brillouin zone center, as indicated in figure 47 [45]. The G peak is the most common signature for all carbon-based material: carbon nanotubes, graphene, graphite etc.

Figure 47 Schematic of first order G-peak process[45]

The D peak originates from a second-order process: breathing-like modes, involving one in-plane transverse optical phonon near the K point and one defect. Importantly, a defect is required to activate this mode through an intervalley double-resonance Raman scattering process, as indicated in figure 48. [45]

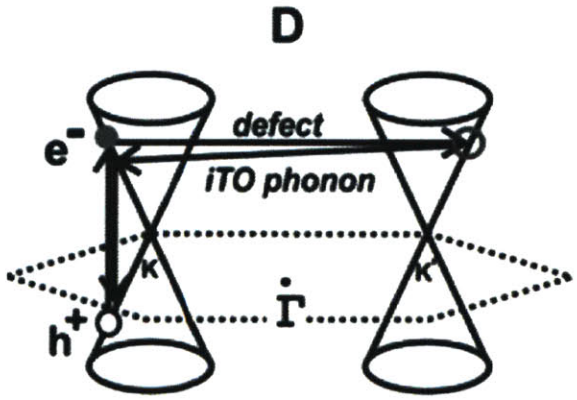

Figure 48 Double-resonance process for D-band (intervalley process) [45]

The G' peak is also a second-order scattering process and involves two in-plane transverse optical phonons near the K point. It is worth noting that the G' peak is symmetry-allowed and exists even in a defect-free sample[45]. A single Lorentzian profile in the G' peak and the relative intensity ration of the G and G' peaks are the most important signatures of single layer graphene. Figure 49 shows the double-resonance process responsible for the G' peak.

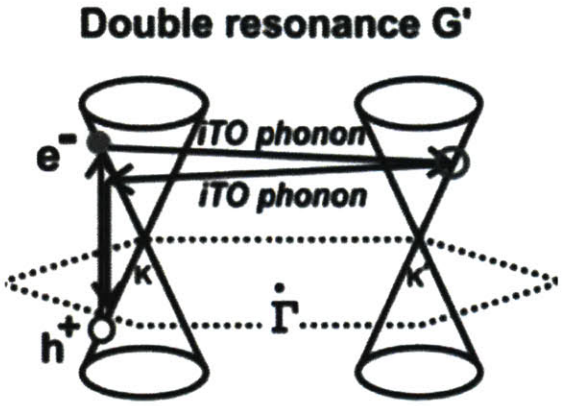

Figure 49 Schematic of the double-resonance process involved in the G' peak[45]

In figure 46, we found a very weak D peak, indicating that the graphene flake has very few defects. Also, the G'/G peak intensity ratio is about 3-4, and the G' peak has a symmetric Lorentzian profile with a FWHM of about 28 cm^{-1}. These facts together can confirm that this sample is a single layer graphene flake.

➢ Experimental Results of chlorinated graphene

We exposed the graphene sample to a chlorine plasma at room temperature in ECR plasma chamber with a RF bias. The pressure was maintained at 20mTorr, and the flow rate was kept at 80 sccm. The ECR power was 30 Watts. The Raman spectrum after chlorination is shown in figure 50.

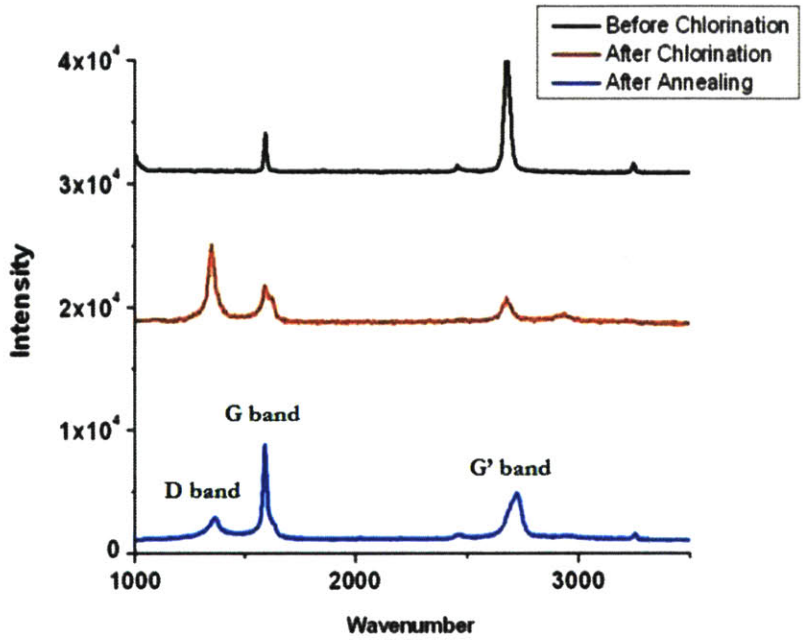

Figure 50 Raman spectrum of graphene before and after chlorination. It also includes the Raman spectrum after annealing.

Several observations can be made in the Raman spectra shown in figure 50. First of all, the D band increased substantially after chlorination treatment. Furthermore, a D' band was created at about 1620 cm^{-1}, which is also a disorder-induced Raman feature. There is also a very weak D+D' peak at ~ 2970 cm^{-1}. All of these features indicate that the symmetry in the sp^2 carbon network was broken after chlorination. There can be two reasons for this. The first one is the creation of defects in graphene. The second reason is some hybridization transition from sp^2 to sp^3 configuration. The difference between the two possible processes is that the hybridization change is a reversible process, while the defect creation is irreversible. To study the relative impact of each one of these processes, we annealed the as-received chlorinated graphene in a furnace at 500 °C, for 30 minutes. After annealing, the D peak (1580 cm^{-1}), D' peak (1620 cm^{-1}) and D+D' peak (2970 cm^{-1}) significantly decreased. This means that the process involved during chlorine plasma treatment is mostly reversible. At the same time, it should be noted that there is still a small D peak residue which cannot be fully eliminated after annealing, which indicates that during this plasma treatment, some defects were created in graphene. This may due to the damage caused by the energetic ion bombardments.

From the analysis above, it is clear that both reversible and irreversible processes happened during the plasma treatment. Some energetic chlorine atoms bonded with π bonds in the carbon atoms and changed its hybridization from the sp^2 to sp^3 configuration. At the same time, some strong σ bonds in graphene were also broken by the ion bombardment.

Next, we studied the impact of the RF bias on the surface functionalization and potential damage to the graphene surface. In these experiments, single layer graphene flakes were identified by their optical images and confirmed by Raman measurement. Then the samples were exposed to chlorine plasma with different RF bias values. Subsequent Raman characterization was done before annealing in an oven to test its reversibility. After annealing in 300℃ for one hour, the Raman spectrum was measured for comparison. It was found that the Raman spectrum significantly changed as a function of the RF bias. Figure 51 summarizes the results.

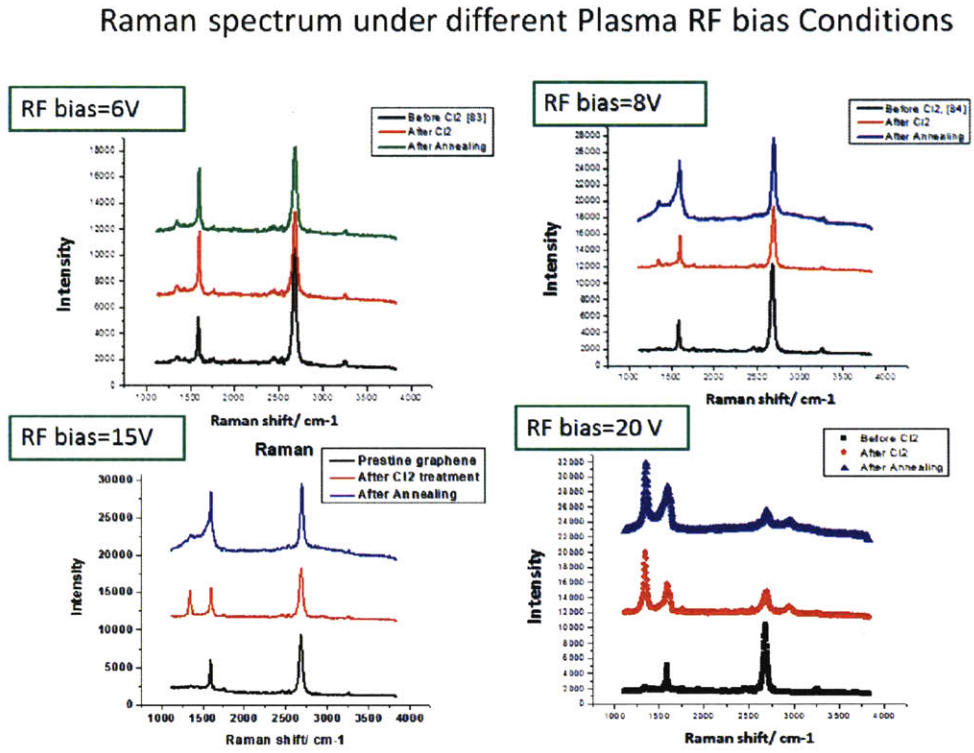

Figure 51 Raman spectrum for graphene flakes under chlorine plasma treatments with different magnitude of RF bias

At a RF bias =6V, the D peak had no obvious changes after chlorination. At higher RF bias (e.g. 8V), the D peak increased a little bit. When the RF bias was further increased, the situation became quite different. First of all, the D peak increased a lot, although this change was mostly reversible after annealing. At an even higher RF bias of 20V, the D peak increased quite a lot, but the spectrum for the pristine sample can no longer be recovered after annealing. Also, the D' peak and D+D' peak appeared after chlorination, and could not be eliminated by annealing.

There are several conclusions that we can draw based on these Raman results. At low RF bias, the chlorine plasma did not have enough energy to impact the hybridization type of the carbon bondings. At a moderate RF bias, the Cl_2 plasma was energetic enough to bond with carbon atoms, and thus change the sp^2 bonding to a partial sp^3 configuration. And this hybridization transition was reversible by annealing, meaning that not many defects were created during this process. When the RF bias was further increased to 20V, the Cl_2 plasma became so energetic that it was destructive to the graphene. Besides changing the bonding configuration of the carbon atoms, it also bombarded the sample as a whole and created a large number of defects in the graphene structure, these induced defects were not reversible any more.

In order to understand what happened in low RF bias conditions, we have to investigate the Raman spectrum in more detail. It is interesting to notice the blue shift in the G peak that was introduced from about 1590 cm^{-1} to 1600 cm^{-1}, after application of the Cl_2 plasma treatment for 600 seconds. This shift indicates that this process induced hole doping (p-type doping) in graphene. We believe that at low energy plasmas, charge transfer occurred during this process, though the plasma was not energetic enough to form covalent bonds with carbon atoms. Moreover, the G peak didn't shift back after annealing, which means the doping remains after the chlorine atoms are desorbed from the surface.

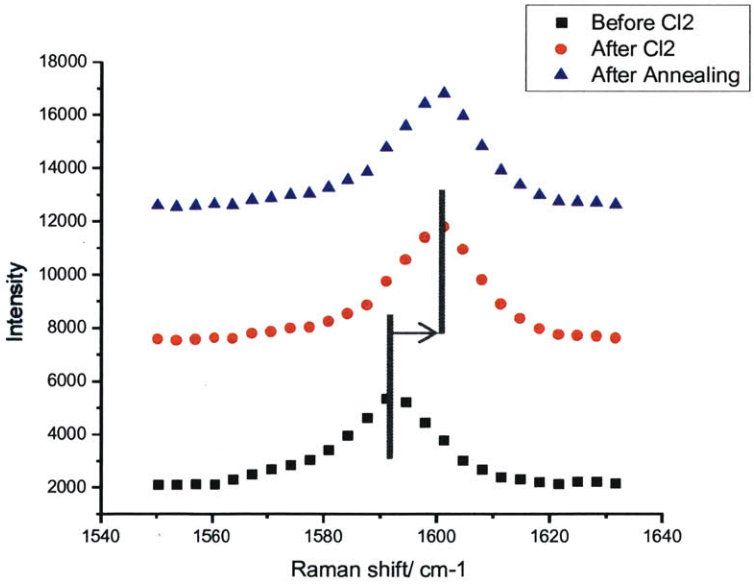

Figure 52 Blue shift in the G peak of graphene after chlorination

This result is shown in figure 52. It is interesting to point out that there are some samples showing slightly different results: the G peak can red shift in frequency a little bit after annealing, as indicated in figure 53.

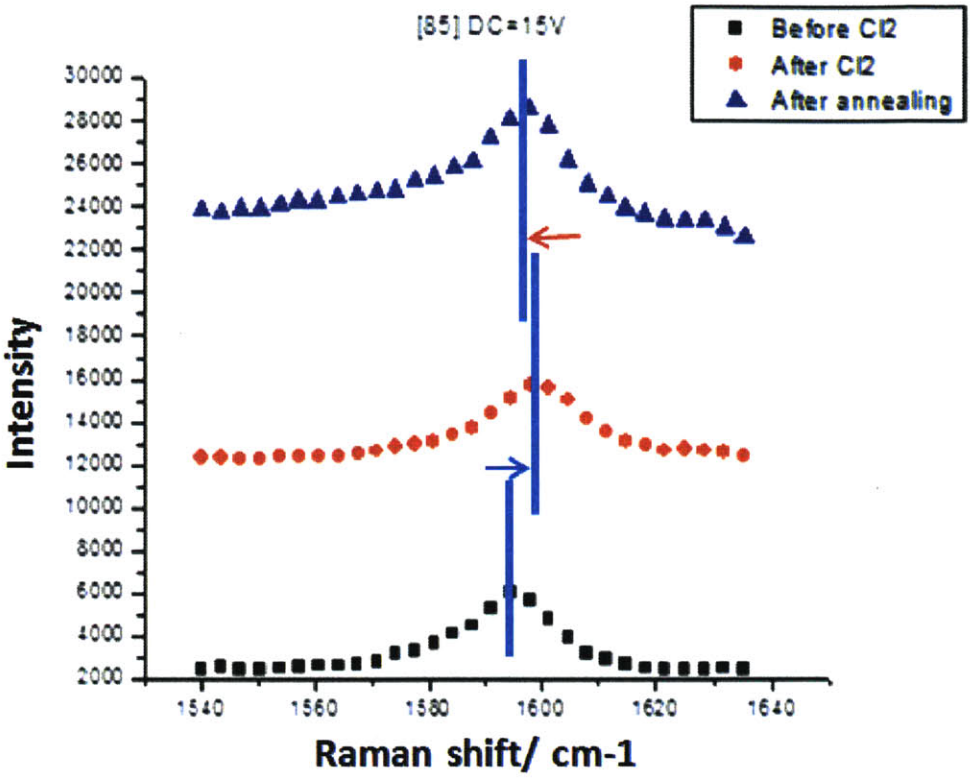

Figure 53 The G peak evolution after chlorination and after annealing

The result in Figure 53 indicated the existence of a competing mechanism. During annealing, the chlorine atoms gain enough energy to escape from the graphene plane, and the atoms return the electrons that were transferred during chlorination process back to the graphene; this is an n-type doping process, as shown in figure 54 where the charge transfer process is indicated and in figure 55 where molecular Cl_2 escape from the graphene surface. On the other hand, graphene may exchange electrons with oxygen gas and H_2O residue on the substrate, etc. during annealing. This process will result in p-type doping (hole doping). Therefore, there is a competition between p doping and n doping in graphene when annealing. That may account for the fact that sometimes the G peak will red shift back a little bit while sometimes this does not happen.

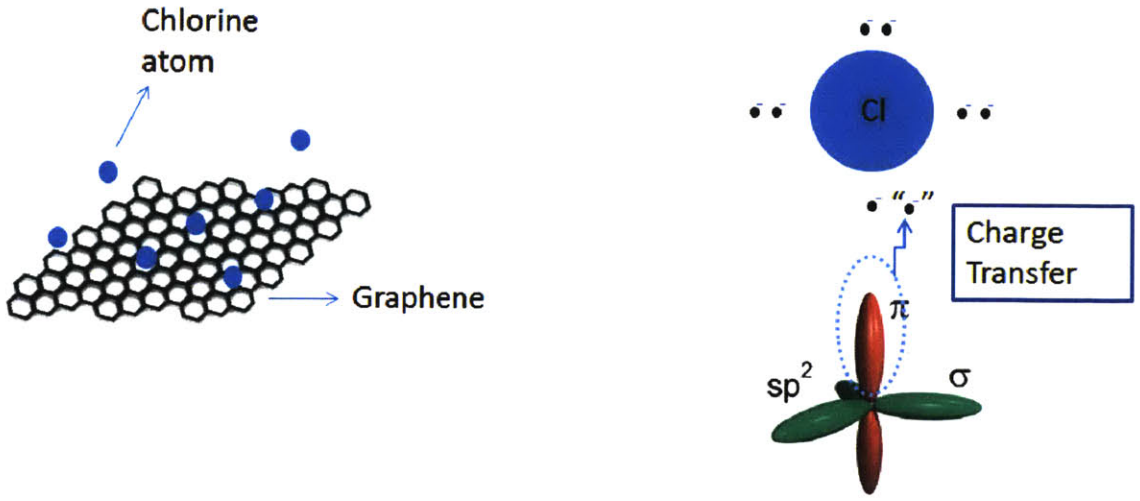

Figure 54 Cartoons showing the charger transfer between graphene chlorine plasma

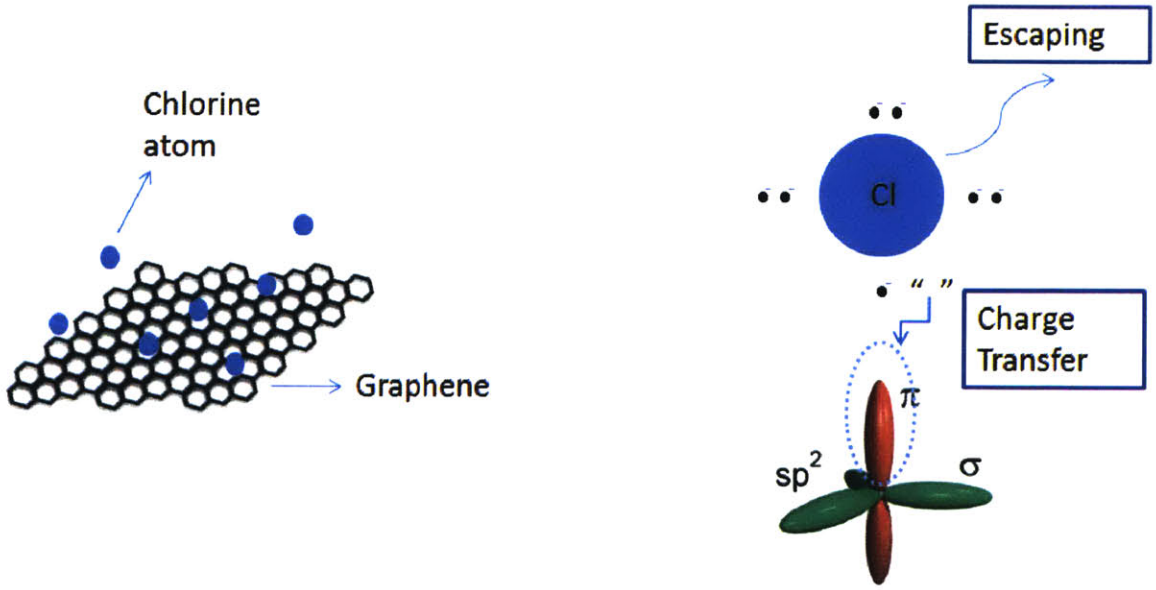

Figure 55 Cartoons showing the charger transfer during the annealing process when Cl_2 molecules escape from the graphene

We also analyzed samples with different chlorine plasma treatment time. It is found that the G peak blue shifted and saturated after a short chlorine treatment, only about 120 seconds, as shown in figure 56. This means that charge transfer during this reaction was very active and fast.

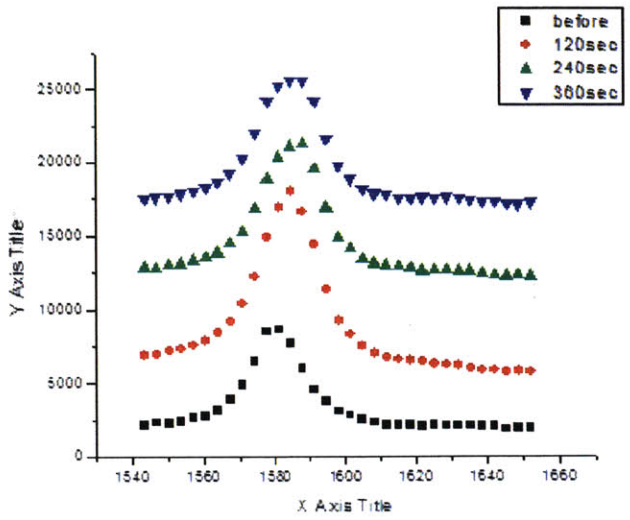

Figure 56 G peak evolution under different chlorine plasma treatment durations

In summary, these results seem to indicate that chlorine plasma treatment is an efficient way to dope the graphene layer p-type in a gentle way without creating damage to the sample. In this process charge is transferred very fast and does not create many defects. Further experimental evidence is needed to confirm this conclusion. Therefore, we will discuss related X-ray photoelectron spectroscopy characterization in the following section.

3.3 X-ray Photoelectron Spectroscopy

➢ Experimental Setups

In order to analyze how much chlorine coverage we got via the plasma reaction, we characterized the as-received chlorinated graphene samples using a Physical Electronics Versaprobe II X-ray photoelectron spectrometer (XPS). XPS is a very powerful tool in terms of elemental and chemical spectroscopic analysis. Both conductive and insulating samples can be analyzed. [51] Figure 57 shows its basic components and configurations. Since it has to count the number of photoelectrons generated, XPS must be operated under ultra-high vacuum (UHV) about $\mathbf{10^{-10}}$ Torr.

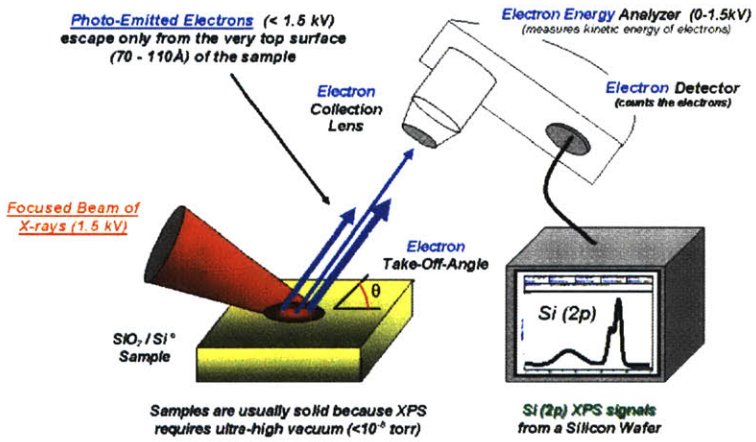

Figure 57 Illustration of the components of an XPS system[51]

The basic physics behind XPS is simple. By illuminating X-ray photons onto the surface of a sample, photoelectrons will be excited and an analyzer will collect and count the number of electrons. The extra kinetic energy of the photoelectrons can be related to their binding energy:

$$E_{kinetic} = E_{photon} - (E_{binding} + \emptyset),$$

where the $\emptyset$ represents the work function of the material. A typical XPS spectrum is a plot of the count number of photoelectrons versus the binding energy of those electrons. [50] Each element has its characteristic XPS peaks at different binding energy levels, such as 1s, 2p etc. By detecting the characteristic peaks, we can identify which elements exist in the sample and the percentage of each element. [51] Figure 58 illustrates the basic "photoelectric effect" in XPS system.

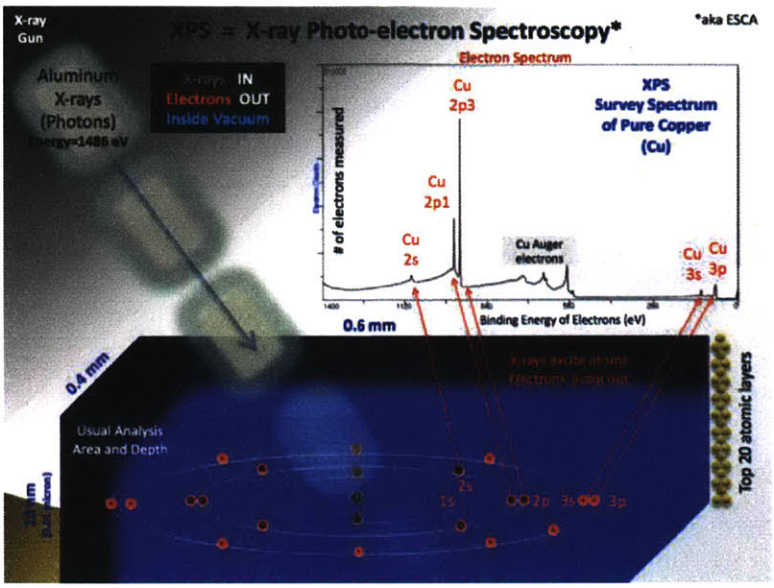

Figure 58 Schematic of the basic physics processes in an XPS system[51]

The XPS measurement facility we used is surface sensitive, with a high depth resolution of about 10 nm. The elemental sensitivity can reach from 0.1 to 0.01 atomic percentages. Its lateral resolution can be tuned from 10 μm to 200 μm, i.e. the diameter of the X-ray spot. During each analysis, the X-ray spot scan in a line with length of 1.3 mm, as shown in figure 59.

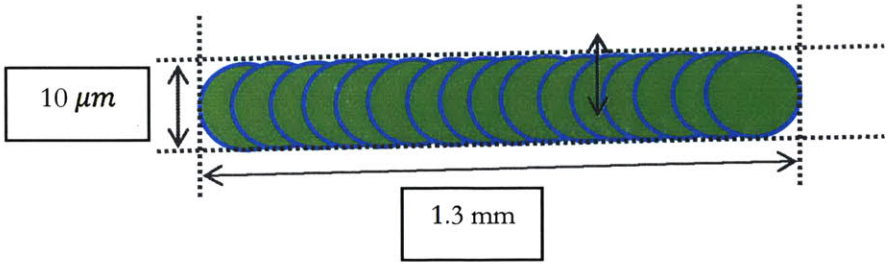

Figure 59 Illustration of the scanning X-ray spots in each run

From this figure, it is easily understood that the information that the XPS collects is statistical on a macroscopic scale. For this reason, the samples we analyzed in this section are all from large-area CVD graphene sheets, rather than from exfoliated HOPG flakes.

➢ Experimental results

We did chlorine plasma treatment on CVD graphene samples. The plasma parameters are summarized in the following table.

Table 1 Experimental parameter of the chlorine plasma reaction

	Step 1	Step 2	Step 3
Chlorine flow rate/sccm	80	80	80
Pressure/ mTorr	20	20	20
ECR power/Watts	0	50	87.42-98.15
RF bias/ Volts	0	0	5.86V
Temperature/ C	25	25	25
Time/ sec	30	5	30

Since the RF bias was relatively low, the plasma glow was dim, but reasonably stable. There were three steps during each chlorination process. During step 1, neither the ECR power nor RF bias was on. Gas was flowed into the chamber and stabilized. In Step 2, the ECR power was on, but the RF bias was still off. This step was a buffered step to condition the chamber. Step 3 was the actual reactions step, during which both the ECR power and the RF bias were applied.

Before doing XPS analysis, we characterized the chlorinated graphene sample by an X-ray generated secondary electron image, as shown in the figure below. We can find that the chlorination in graphene is relatively uniform from this image.

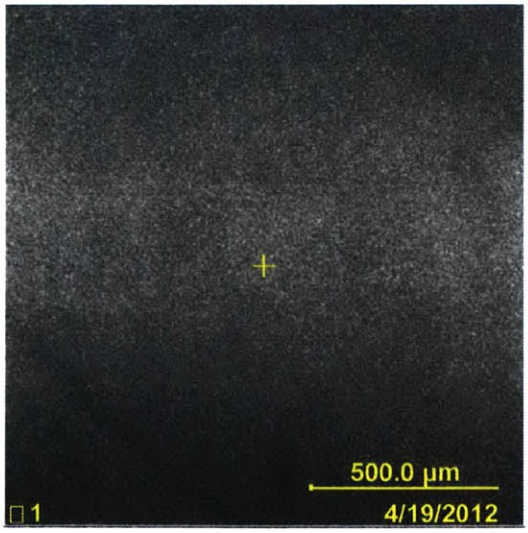

Figure 60 An X-ray generated secondary electron image of a chlorinated graphene sample

We chose six random points on the sample surface for analysis, and the results are shown in Figure 61.

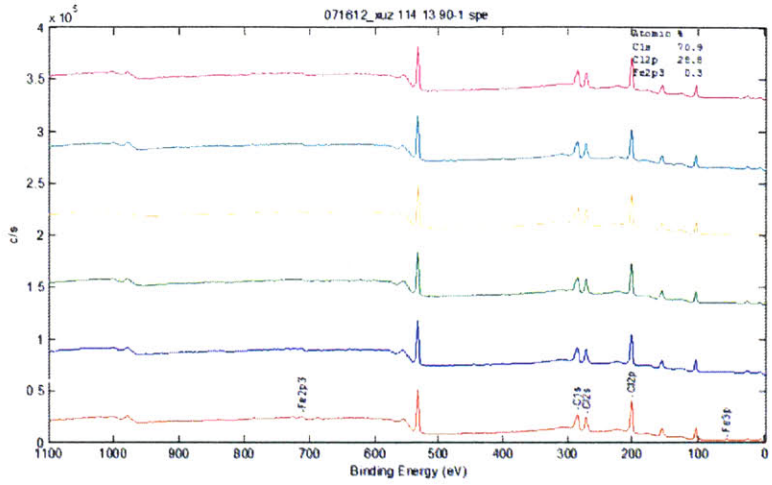

Figure 61 The XPS spectrum of chlorinated CVD graphene taken at 6 different random locations of 10 um diameter

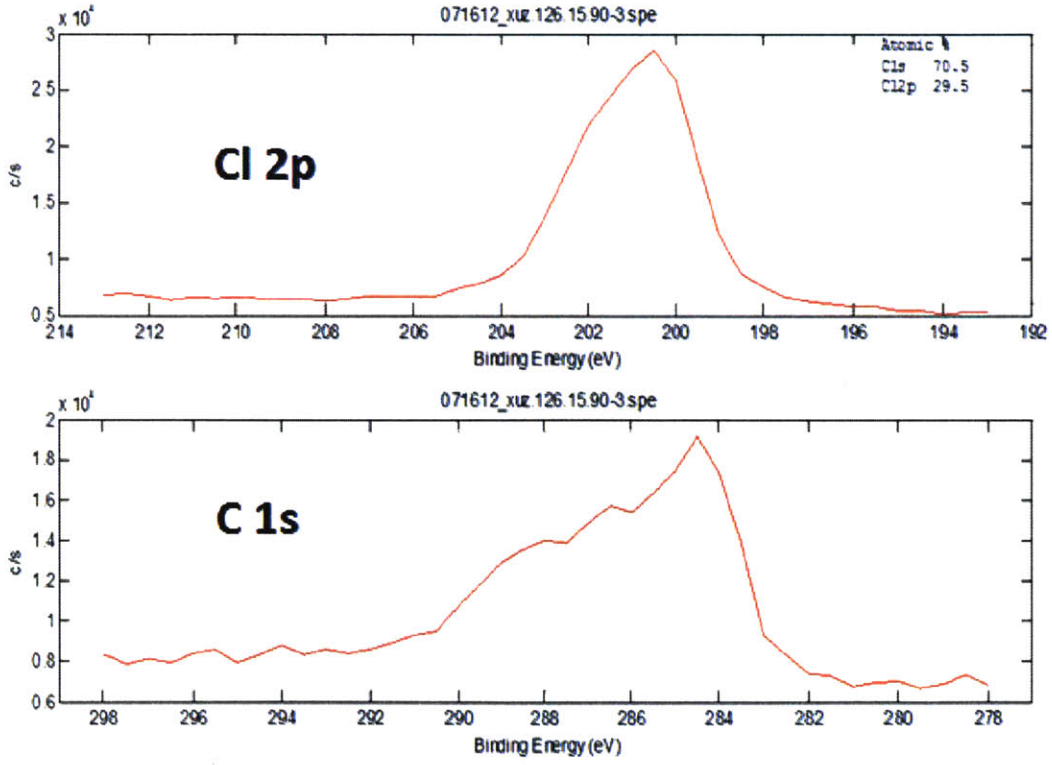

Figure 62 Details of C and Cl peaks in the XPS spectrum

Consistent with the secondary electron image, the XPS spectrum also showed a uniform feature in terms of chlorination coverage. Three elements were identified: carbon, chlorine and iron. (A silicon peak and an oxygen peak are also very obvious, but they result from the substrate SiO_2). The detection of iron is not surprising, since the $FeCl_3$ (aq) solution was used during wet transfer. Table 2 summarizes the atomic percentage of each element. From Table 2, we found that the quantity of iron was very low, only about 0.29% by atom. Strictly speaking, the existence of chlorine came from two sources: the chlorine plasma and the $FeCl_3$ solution during transfer. Because the quantity of chlorine coming from $FeCl_3$ should be on the same order as the iron percentage, we can infer that this source of chlorine can be neglected. The chlorine detected by XPS mainly comes from the chlorine plasma reaction. The Cl peak is labeled as Cl2p, while the carbon peak from graphene is labeled as C1s and the iron peak from $FeCl_3$ is labeled as Fe 2p3.

Table 2 The atomic percentage of C, Cl and Fe detected in the chlorinated graphene

	C 1s	Cl 2p	Fe 2p3
Atomic percent/%	70.44	29.27	0.29

To confirm that the Cl introduced during the wet etch of the Cu film is very low, we compared the XPS spectrum of chlorinated graphene with that of untreated CVD graphene, transferred by the same procedure. The chlorine percentage was very low in untreated CVD graphene, only 1.06%, as shown in Figure 63.

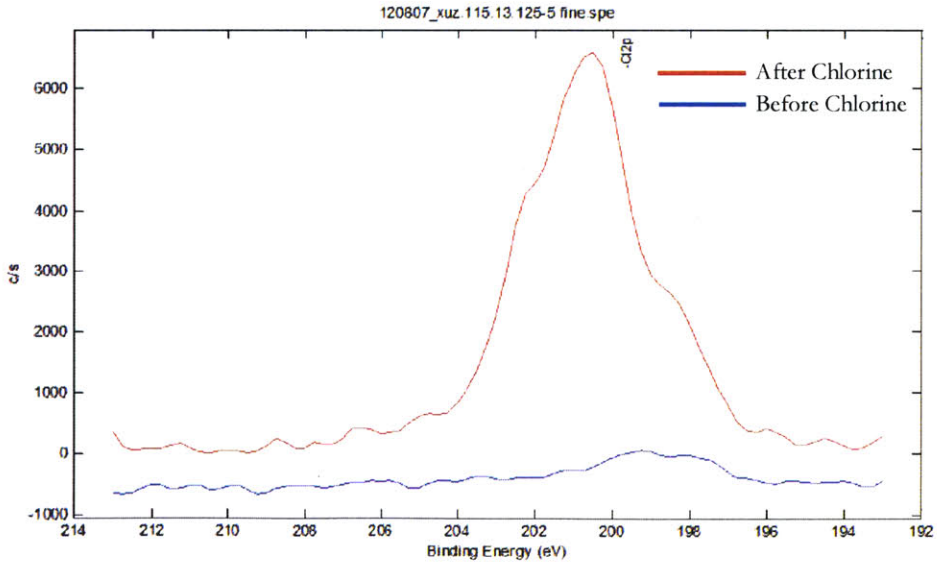

Figure 63 Comparison between the Cl 2p peak in the XPS spectrum of CVD graphene before and after chlorination. The peak value here is ~ 0 c/s before chlorination and ~6500 c/s after chlorination.

Therefore, the corrected chlorine coverage is 29.27%-1.06%=28.21%. The Cl: C ratio is about 1:2.5. Theoretically, the maximum possible Cl:C for single-side chlorinated graphene is 1:2, which means that one of the two sublattices in the graphene structure is completely bonded with chlorine atoms. Figure 64 belows illustrates this configuration.

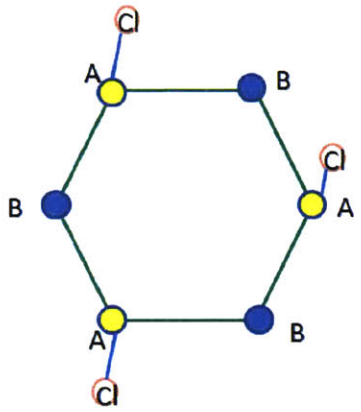

Figure 64 Configuration of chlorinated graphene when one sublattice is fully covered by chlorine atoms

The chlorinated graphene we prepared is very close to this theoretical limit, and is quite stable under ambient condition for weeks. However, theoretical work predicts that the most energy-favorable chlorination in graphene is Cl:C = 1:4 (for a homogenous pattern). And they also claim that the random cluster adsorption of hexagonal chlorine rings on graphene is even more stable, in which case the Cl:C ratio will be less than 1:4 [37]. Our results do not agree well with this theoretical prediction. What caused the discrepancy (meaning the higher chlorine concentration) between the theoretical and experimental results needs further investigation.

It is interesting to compare the carbon 1s peak in XPS spectrum before and after chlorination. Before chlorination, the carbon 1s peak had only one component, which s centered at 284.5eV (figure 65). This peak corresponded to the sp^2 binding energy. This is consistent with the magnitude of the bonding hybridization in pristine graphene.

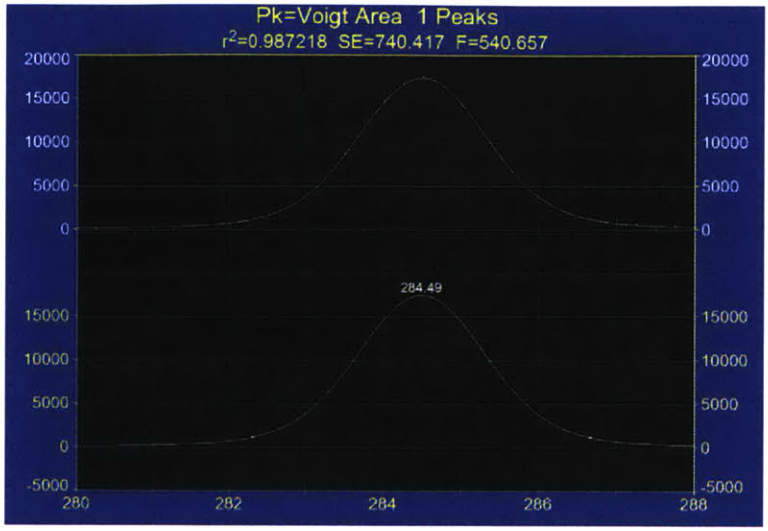

Figure 65 Peak fitting result of the C 1s XPS spectrum of pristine CVD graphene. The upper curve is the experimental Raman spectrum, while the lower curve is the fitting curve with single Lorentzian profile.

After chlorination, the carbon 1s peak changed dramatically, as Figure 66. It had two components: 284.4eV and 285.1eV, which were identified as sp^2 and sp^3 hybrids formed in chlorinated graphene. By calculating the areas under each peak component, we can get the sp^2/ sp^3 bond ratio which is measured to be about 9:1.

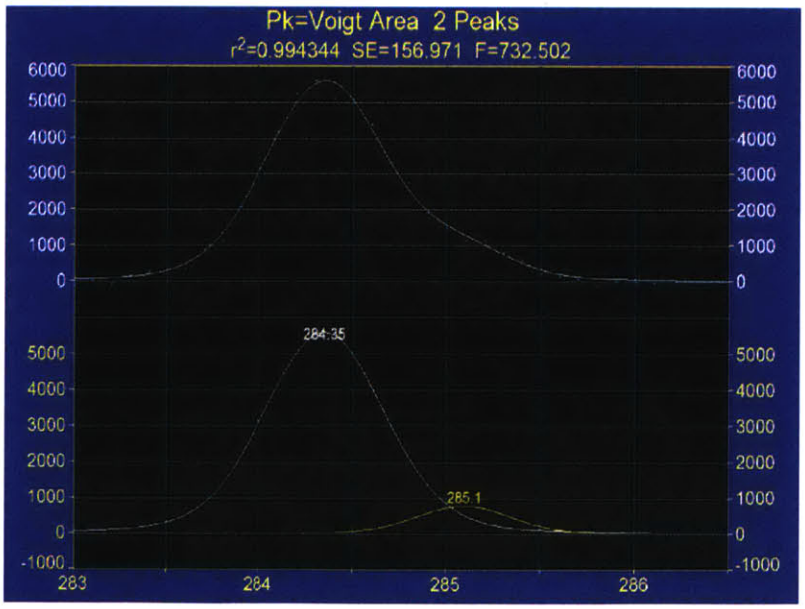

Figure 66 Peak fitting result of the C 1s XPS spectrum of chlorinated graphene. The upper curve is the experimental Raman spectrum, while the lower curve is the fitting curve with single Lorentzian profile.

There are several conclusions that can be drawn based on the XPS results of section 3.3 and the Raman spectrum described in the last section 3.2. First of all, during the plasma treatment, a large amount of carbon atoms were functionalized by chlorine. The Cl:C ratio of our chlorinated graphene samples reaches 2.5:1, which means 40% of the carbon atoms in graphene are bonded with chlorine. Moreover, the chlorination via this method is quite stable under ambient conditions. Secondly, the chlorine plasma did change the hybridization type from sp^2 to sp^3 partially, in which case carbon atoms interacted with chlorine atoms through covalent bonds. Last, the sp^3/sp^2 ratio was only about 1:9, which told us that only 10% of the carbon atoms changed their bonding type from sp^2 to sp^3. The majority of chlorinated carbons atoms remained in the sp^2 hybridization, though they did interact with chlorine plasma. We inferred that those sp^2 chlorinated carbon atoms bond with chlorine atoms via van der Waals interactions. No covalent bonds formed in this reaction stage; however, charge transfer occurred between the graphene and chlorine plasma. If this is true, this will be the first experimental evidence about the existence of a graphene-Cl charge transfer complex through Van der Waals bonds.

It is also interesting to examine how the chlorine coverage on graphene changes with plasma treatment duration keeping other parameters constant. We investigated this question by tuning the reactions time. The result was quite counter-intuitive, as shown in figure below.

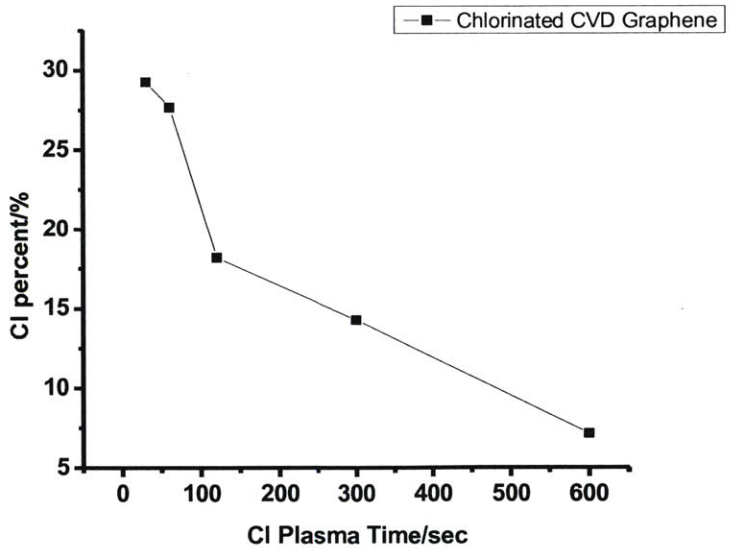

Figure 67 The relation between chlorine coverage percent on graphene and the chlorine plasma treatment time

As a first thought,, one would expect the chlorine coverage would increase with time and saturates at some point. However, it turns out that the chlorine plasma reacted with the

graphene very efficiently; it reached its maximum value within 30 seconds. Counter-intuitively, further chlorine dose led to a decrease in the chlorine percentage coverage. The reason may be that most of the chlorine-graphene bonds at this stage were weak (Van der Waals bonds), and further chlorine atom bombardment may break these weak bonds, thereby resulting in chlorine atoms getting desorbed escaping from the graphene surface.

3.4 Transport Characterization

➢ Experimental setups

Chlorinated graphene-based FETs were fabricated using e-beam lithography and optical lithography. The following figures show the optical image of two examples of chlorinated graphene devices.

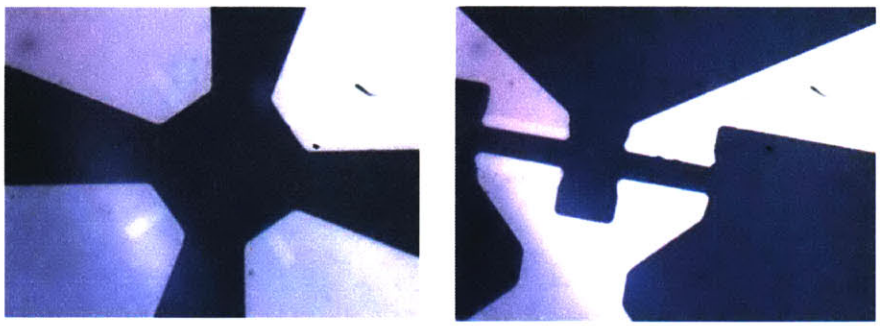

Figure 68 Optical images of two examples of graphene FETs measured in this thesis

The samples were measured using a Cascade MicroTech Summit 11000AP Probe Station (Figure 69). Tri-axial cables were used to minimize the leakage current between the core and the inner shield, and thus enabled precision low-current measurement. Figure 70 shows the Triaxial BNC connector. Agilent 4155C Semiconductor Programmer Analyzer was used to control the measurement and performed graphical analysis.

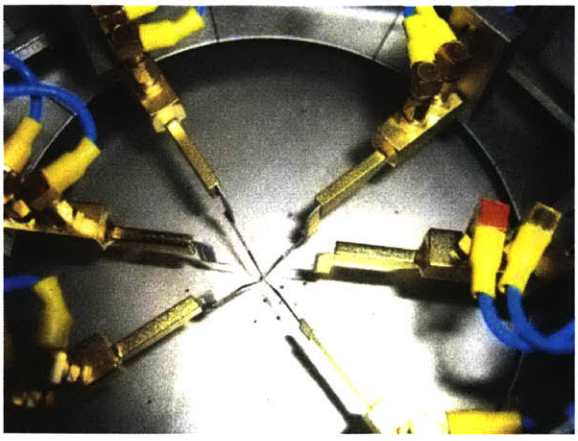

Figure 69 Image of the Cascade MicroTech Summit 11000AP Probe Station

Figure 70 Image of the triaxial BNC connector

➢ Experimental Results

The figure below compares the conductivity of graphene FETs before and after chlorine plasma treatment. First of all, the conductivity increased after chlorination, which means the plasma process was very gentle to the graphene surface, not creating too much surface damage. In addition, the Dirac voltage, corresponding to the point where the conductivity is minimum, shifted far beyond 100V (heavily hole doping). This result was not surprising and consistent with the Raman measurement: the blue shift in the G peak of the Raman spectrum also indicated a high hole doping during the plasma reactions.

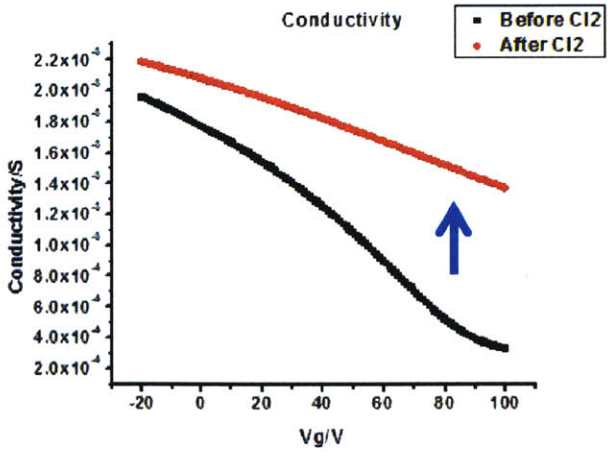

Figure 71 Conductivity of a chlorinated graphene FET before and after chlorine plasma reaction

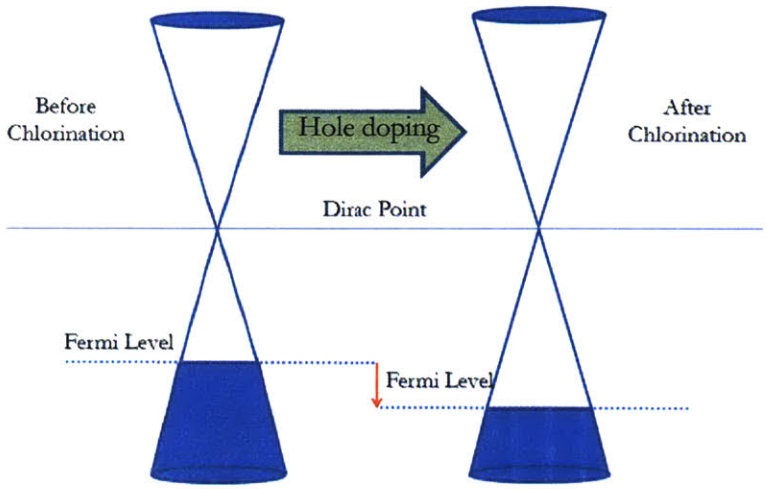

Figure 72 Schematic of the Fermi level movement during the chlorine plasma treatment showing p-type doping

Figure 72 above indicates how the Fermi level changed after chlorination. The CVD graphene we used was intrinsically p-type doped. Its Fermi level is below the Dirac point before any chlorination, due to p-type doping during the process of transferring graphene from copper to the SiO_2 substrate. When exposed to a chlorine plasma, the chlorine atoms interacted with the graphene and trapped an electron from the π orbit of each chlorinated carbon atom. Therefore, the chlorination of graphene was a hole-doping process.

As we mentioned during the analysis of the Raman spectra, chlorination in graphene via plasma reactions is very efficient and it saturates within the first 30 seconds. After 30 seconds, the G peak did not blue shift any more. Here, we found that the transport measurement was also consistent with the Raman results. The Dirac point shifted in the p-type direction in very short time, for both exfoliated graphene and CVD graphene. The Dirac voltage in chlorinated graphene was much more than 100 volts, far beyond the range that we can measure with our Agilent 4155 setup. This observation, together with the Raman results, confirmed that chlorination via plasma reactions was very fast, and that it impacted the carbon bonding in graphene in a very gentle and mild way.

In order to track the doping evolution in chlorinated graphene, we fabricated a conventional graphene FET. Then we spun a PMMA layer on top and opened a very narrow gap (180nm in width) in the PMMA layer over graphene channel region, as shown in Figure 73.

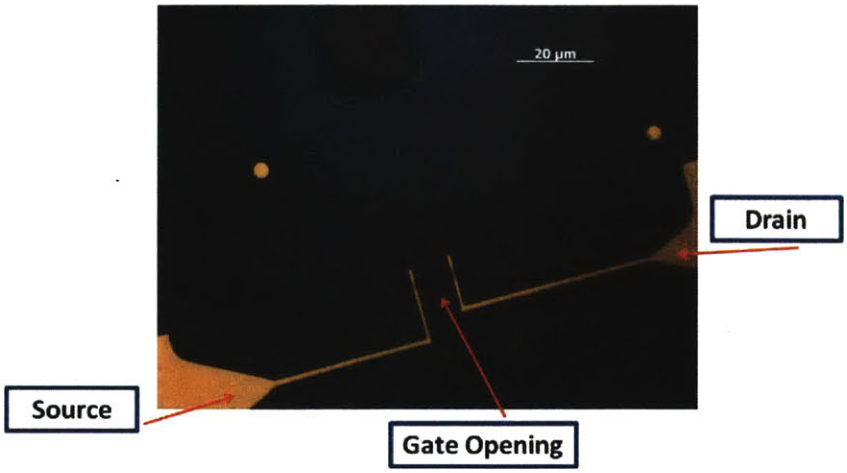

Figure 73 A small gap opened in the channel of the chlorinated graphene FET

We measured the Dirac point shift after different chlorine plasma treatment duration, as shown in the figure below. When only a narrow gap area was exposed to chlorine, the reaction was relatively slower than when a large-area was exposed. After 60 seconds, the hole doping process saturated. And from figure 74, the Dirac point p-type shift can be clearly tracked.

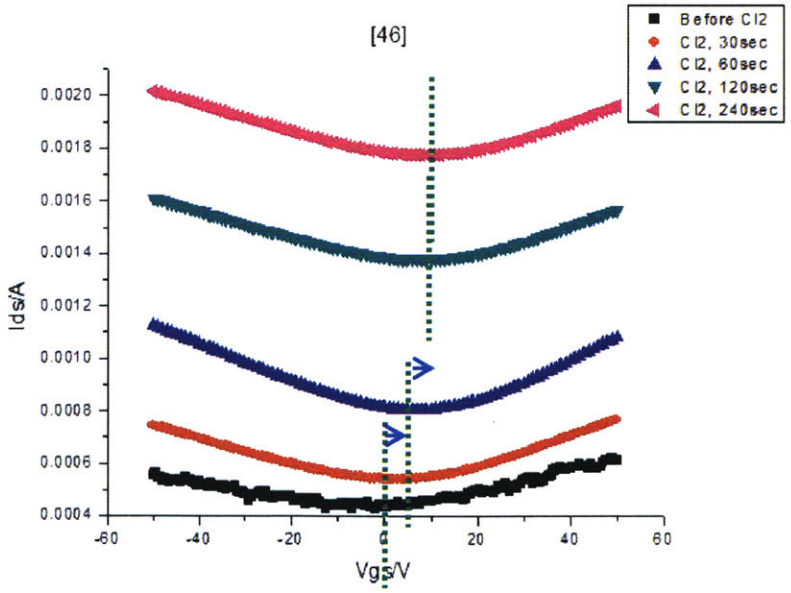

Figure 74 Dirac voltage p-type shift under different chlorine plasma treatment time as indicated in the legend (upper right).

To further confirm the p-type doping process during the plasma reaction, we also measured the change in the graphene carrier concentration after chlorination. From figure 75, we found that the hole concentration before chlorination was on the level of $10^{12}\ cm^{-2}$. After chlorination, the hole concentration increased by about 3-4 times. This result reinforced our previous conclusion about hole doping.

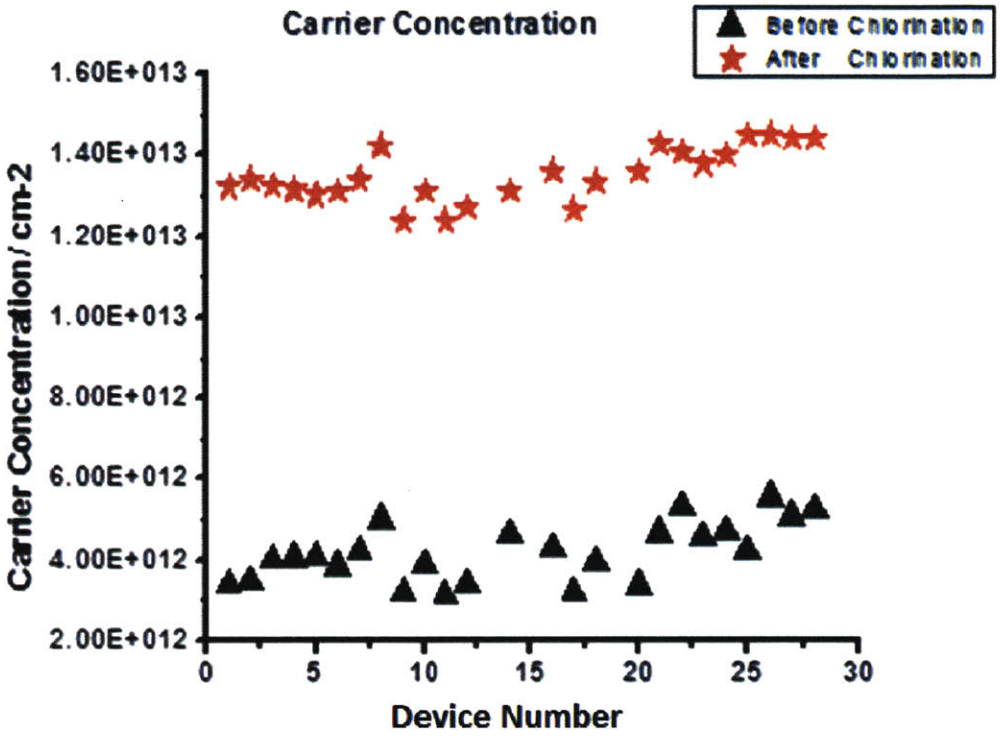

Figure 75 The increase of the hole concentration after chlorination for numerous devices.

It is very critical to investigate how the chlorination process impacted the mobility in graphene. High mobility is the most obvious advantage of graphene's electronic properties. If we have to sacrifice this property in order to engineer its band structure, graphene electronic devices would be less attractive. We did mesa isolation in CVD graphene to fabricate a large-area sheet into an appropriate crossing shape for Hall measurement in order to measure its mobility. Figure 76 shows how the configuration looks like. The yellow dotted lines indicate the area where the CVD graphene layer remains.

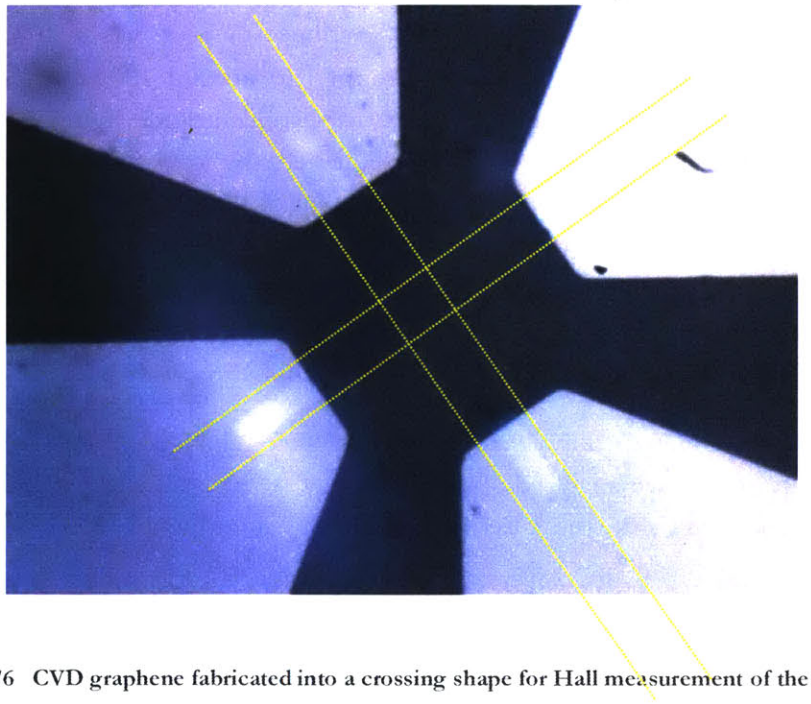

Figure 76 CVD graphene fabricated into a crossing shape for Hall measurement of the mobility

About thirty Hall bar devices were measured and the mobility results before and after chlorination were collected in Figure 77.

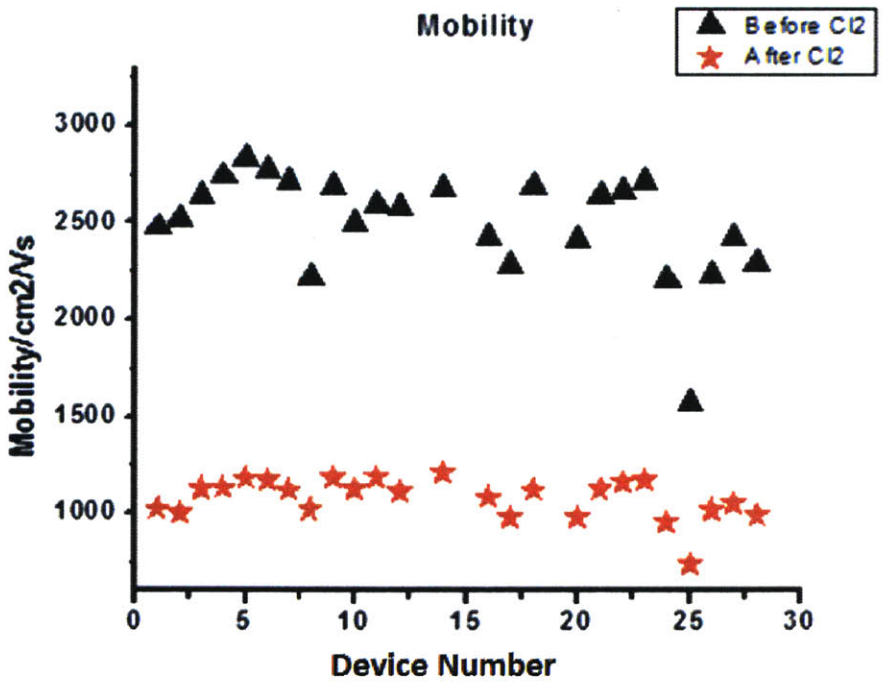

Figure 77 Carrier mobility before and after chlorination in CVD graphene

Before chlorination, the mobility of our graphene devices was in the 2000-3000 $cm^2/V \cdot s$ range. After chlorination, the mobility dropped to around 1000 $cm^2/V \cdot s$. As the chlorine plasma doped the graphene samples, the carrier concentration increases, and thus the carrier-carrier scattering also increases. As a consequence, the intrinsic mobility of the graphene will drop. The important thing here is that the mobility in the chlorinated graphene is still quite high after chlorination, in comparison with hydrogenated graphene and fluorinated graphene, which usually were found to possess mobilities of only ~ 10 $cm^2/V \cdot s$. [23] It is also worth pointing out that a mobility of 1000 cm^2/Vs is still higher than the typical carrier mobility in silicon MOSFETs at full channel charge operating at room temperature.

We also investigated how the sheet resistance changed after chlorination. From the conductivity results we analyzed above, it is expected that the sheet resistance will drop. And this was confirmed by the measurement results shown in Figure 78.

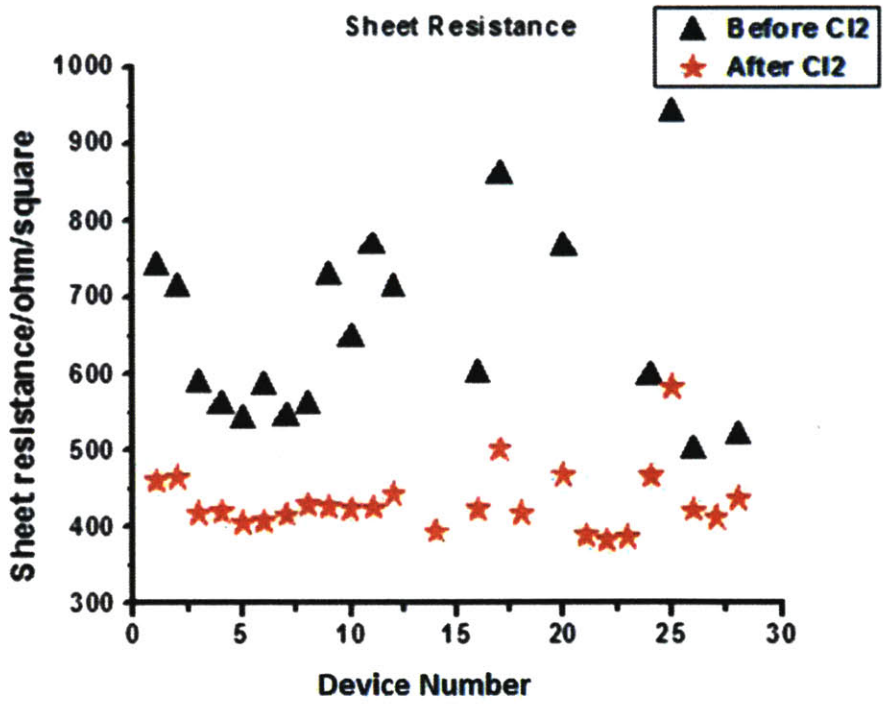

Figure 78 Sheet resistance before and after chlorination in CVD graphene

The standard deviation of the sheet resistance is larger than that of the mobility and carrier concentration, but for each device we measured, its sheet resistance always decreased after chlorination. The decrease in sheet resistance and increase in conductance both result from the

increase in the carrier concentration. The relation between carrier concentration, mobility and conductivity is expressed as.

$$n \cdot \mu = 2.42 \times 10^4 \cdot \sigma ,$$

where, the n is the carrier concentration (in units of $10^{10}\, cm^{-2}$), μ represents the mobility (in units of $cm^2/V \cdot s$) and σ is the conductivity (in unit of e^2/h). [52] In this way we find that there is a competition between the impact of n and μ on the change of the conductivity (sheet resistance): the decrease of the mobility tends to decrease the conductivity (increase the sheet resistance), while the increase of carrier concentration tends to increase conductivity (decrease sheet resistance). And the overall result shows that chlorination can lead to increased conductivity. This can also be regarded as an evidence that the chlorine plasma process is non-destructive to graphene, which maintains its attractive high mobility after chlorination.

In order to demonstrate that the chlorination process in this study was gentle to graphene, we also compared the atomic force microscope images before and after plasma treatment, as shown in the AFM images in Figure 79 and 80.

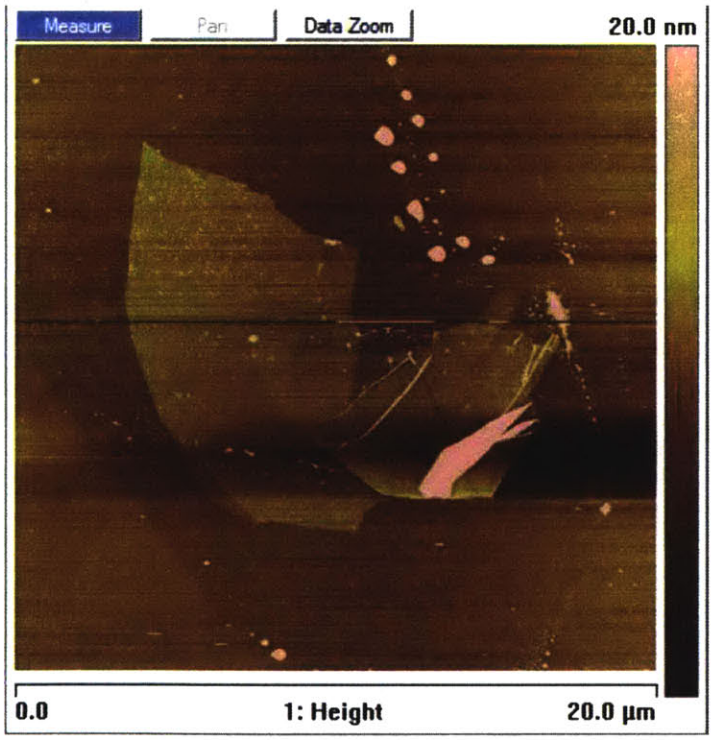

Figure 79 AFM images of an exfoliated graphene flake before chlorine plasma treatment

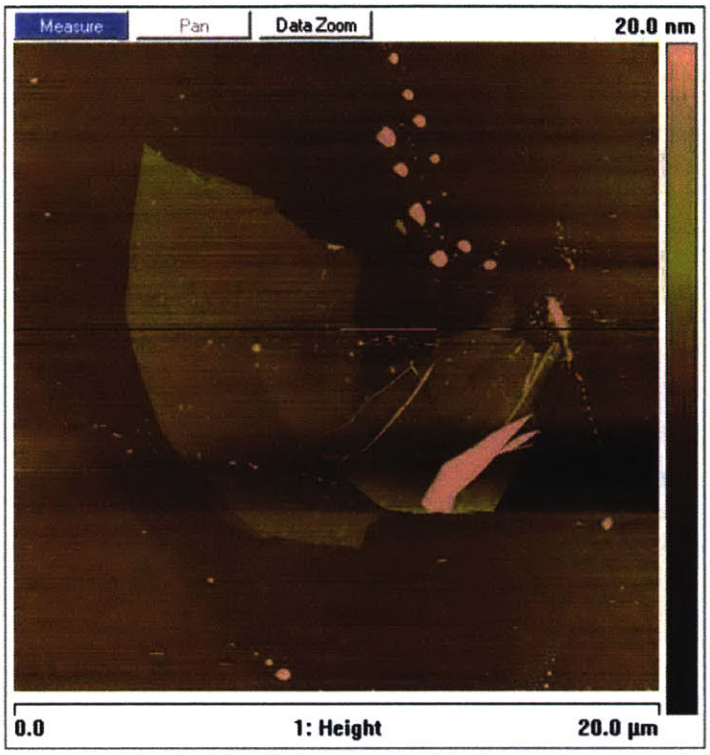

Figure 80 AFM images of an exfoliated graphene flake after chlorine plasma treatment

Comparing the AFM images of the exfoliated graphene flake, we found that all the detailed topography of the sample was preserved, which means that the chlorine plasma was not etching the sample at all. This is very important result for the fabrication of chlorinated graphene FETs. We also did Raman G peak mapping as shown in Figure 81 below. This result also supported the AFM observations that the physical topography of this graphene flake was well preserved after chlorination.

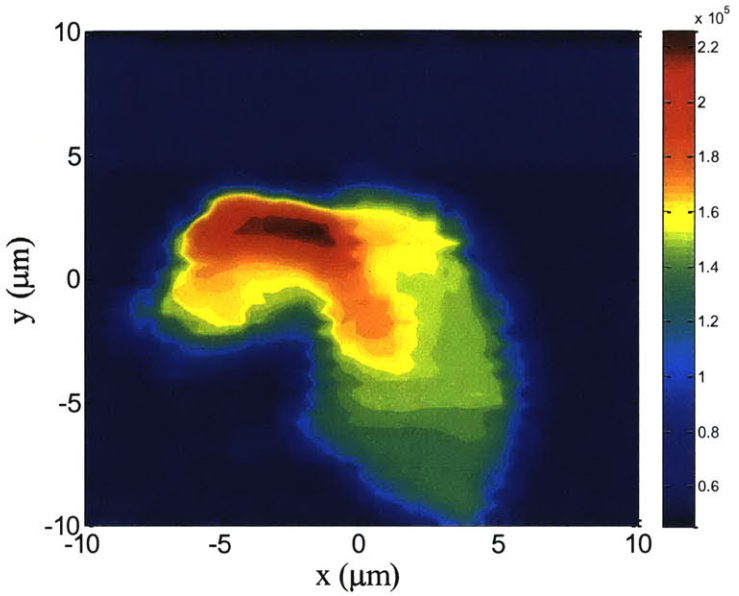

Figure 81 G peak mapping in Raman spectroscopy of chlorinated graphene.

In summary, we investigated the transport properties of graphene FETs chlorinated by plasma treatment. There are several conclusions that can be drawn from these results. First of all, chlorination through exposure to chlorine plasma is a very efficient way to induce hole doping in graphene. The hole concentration can in this way be increased from $10^{12}cm^{-2}$ to $10^{13}cm^{-2}$. Secondly, the reaction between the graphene and the chlorine plasma is very fast. It saturates within 30 seconds for large-area CVD graphene. Furthermore, chlorination in graphene is very controllable; by tuning the RF bias, the interaction between the carbon atoms and chlorine can be controlled to be charge transfer (Van der Waals bonding), covalent bonding or defect creation. Last but not least, the chlorination in a plasma chamber is non-destructive to graphene. Its mobility can be kept at ~ 1000 $\frac{cm^2}{Vs}$, even after chlorination. This is a highly unique advantage over hydrogenation and fluorination, as we will see in Chapter 4 of this thesis.

3.5 Reaction Mechanism of Chlorination in Graphene

Based on all the Raman characterization, XPS characterization and transport measurement, we can integrate all these results to propose a schematic picture of how the chlorine plasma interacts with graphene. The critical factor here is how energetic the chlorine atoms are, which can be controlled by the RF bias. Under different RF bias voltages, the reaction between carbon and chlorine atoms is quite different. Now let us discuss the interaction during chlorination at different RF bias voltages.

- **Low RF bias (<6V)**

When the RF bias is low, the chlorine plasma is not energetic enough to impact the carbon sp^2 hybridization. However, the chlorine ions can bond with carbon atoms through Van der Waals bonds, and charge transfer can occur during this process. As illustrated in the figure below, " ⬮ " represents the Van der Waals bonds between carbon and chlorine. Only 10% of the carbon atoms change their bonding type from sp^2 to sp^3 configuration, as indicated schematically by the yellow dots. Those carbon atoms will bond with chlorine through valence bonds and the carbon atom is thereby lifted up out of the graphene plane.

In this circumstance, 90% of the carbon atoms (see section 3.3) in graphene only form very weak bonds with chlorine (via Van der Waals bonds). However, the chlorinated graphene is quite stable under ambient conditions. The flat structure of graphene is largely maintained and therefore no D peak is expected in the Raman spectrum. This agrees well with our Raman results. However, charge transfer (hole doping) is allowed and this observation is consistent with the G peak blue shift in the Raman spectrum.

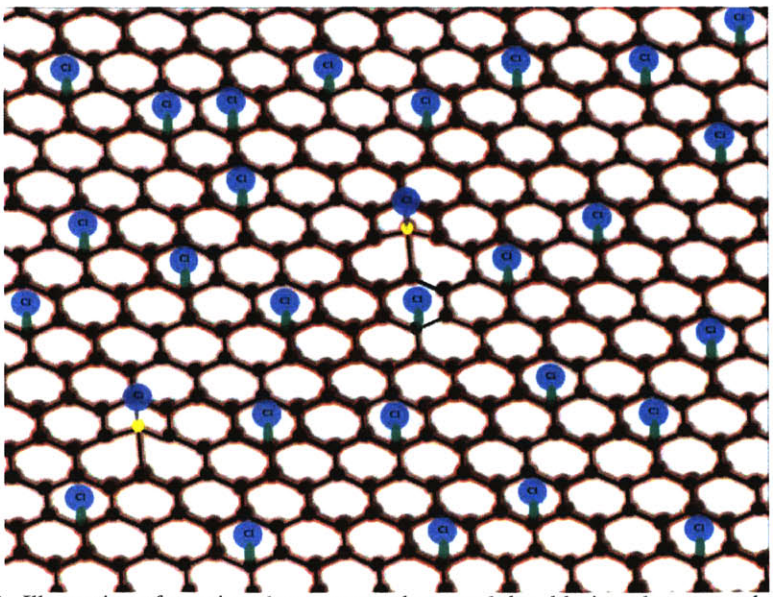

Figure 82 Illustration of reactions between graphene and the chlorine plasma at a low RF bias

➢ **Moderate RF bias (8-15V)**

As the RF bias is increased, more and more chlorine atoms have enough energy to alter the hybridization of the carbon bonds. Therefore, the overall sp^3 bonding component in chlorinated graphene will increase as a result. As indicated in Figure 83, " ▮ " represents the covalent bond between carbon and chlorine atoms. The graphene structure is more and more deformed where the carbon hybridization type is changing to the sp^3 configuration. As a consequence, D peak intensity will show up in the Raman spectrum. And it can be expected that as a higher RF bias is applied, the higher D/G ratio will be in the Raman spectrum, which agrees well with our Raman measurements.

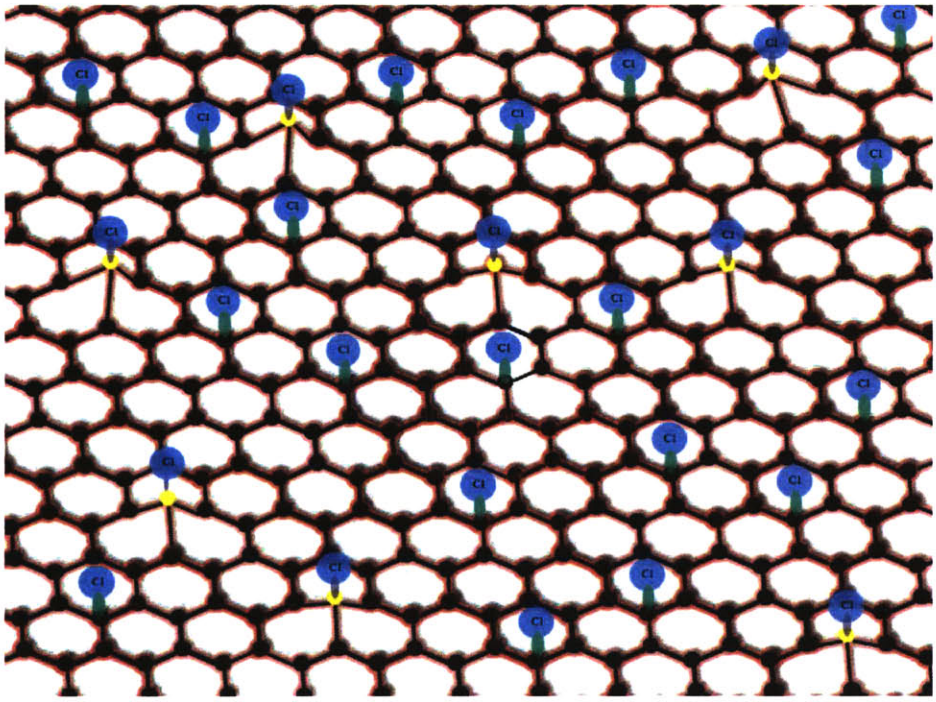

Figure 83 Illustration of reactions between graphene and chlorine plasma at moderate RF bias

At some point in the applied RF bias (~ 15V), the plasma has enough energy to make all the bonds between the graphene and chlorine covalent, as illustrated in Figure 84 where we see that. The sp^3 hybridization dominates in this situation.

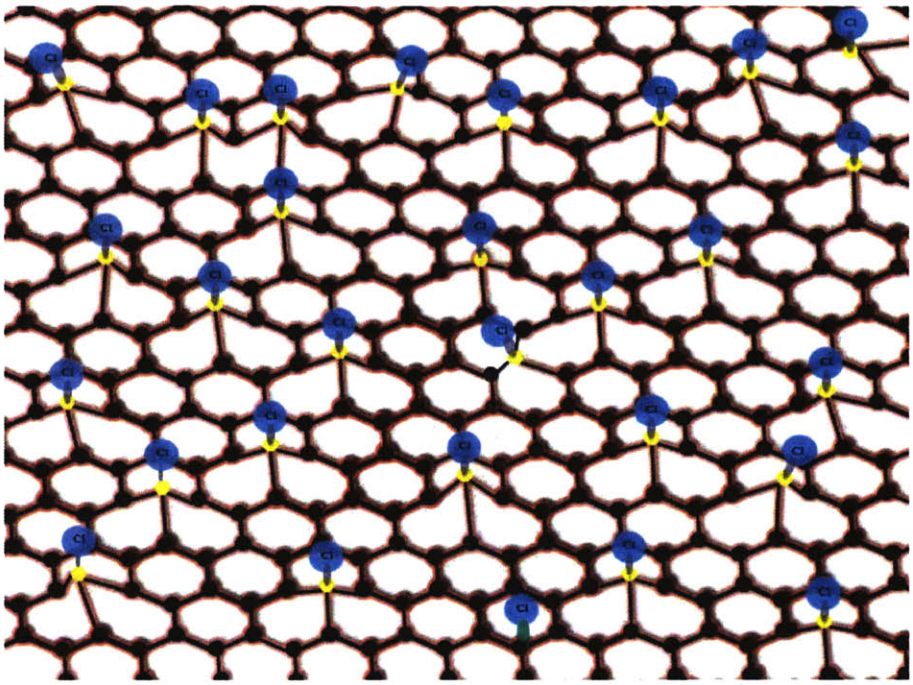

Figure 84 Illustration of the reactions between graphene and chlorine plasma when sp3 hybridization dominates

From this figure, it is easy to understand why the mobility drops from ~ 2000 $\frac{cm^2}{Vs}$ to about 1000$\frac{cm^2}{Vs}$ after chlorination if no defects are created. There are two main factors contributing to the mobility decrease. On one hand, the chlorination increases the carrier concentration by 3-5 fold. As a result, the electron-electron scattering is significantly enhanced, which degrades the mobility in graphene. On the other hand, when the RF bias is high enough to alter the carbon bonding type from the sp^2 to the sp^3 configuration, the chlorine atoms move the carbon atoms up out of the flat plane, as the carbon atom is bonded with that Cl atom through a more covalent bond. The graphene 2D structure is then deformed and the scattering between electron and the carbon lattice is increases, i.e. the electron-phonon scattering is enhanced. This is illustrated in figure 85. These two factors, increased electron-electron scattering and electron-phonon scattering, together contribute to the mobility degradation.

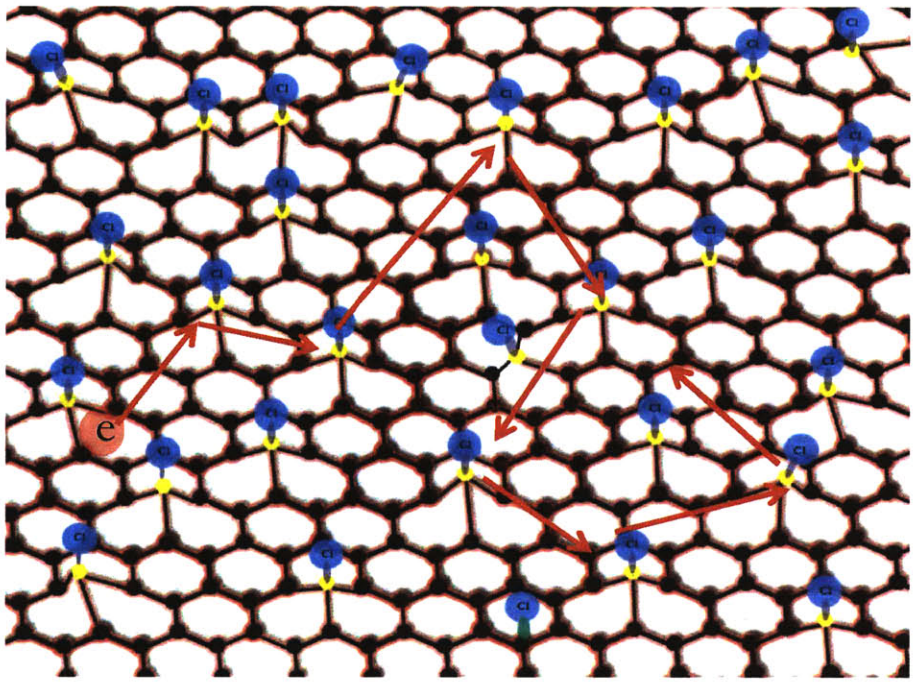

Figure 85 Illustration of one electron in graphene being scattered randomly by the deformed carbon structure

➢ High RF bias (>20V)

When the RF bias is further increased, the chlorine plasma becomes so energetic that it is destructive to the graphene structure itself. Besides charge transfer and sp^2 to sp^3 hybridization transition, defect creation also occurs during the chlorination process. This situation is summarized in figure 86 below. Importantly, the defects caused by chlorine plasma bombardment cannot be eliminated by annealing. This explains why the D peak in the Raman spectrum did not change after annealing, as shown in figure 87 (d).

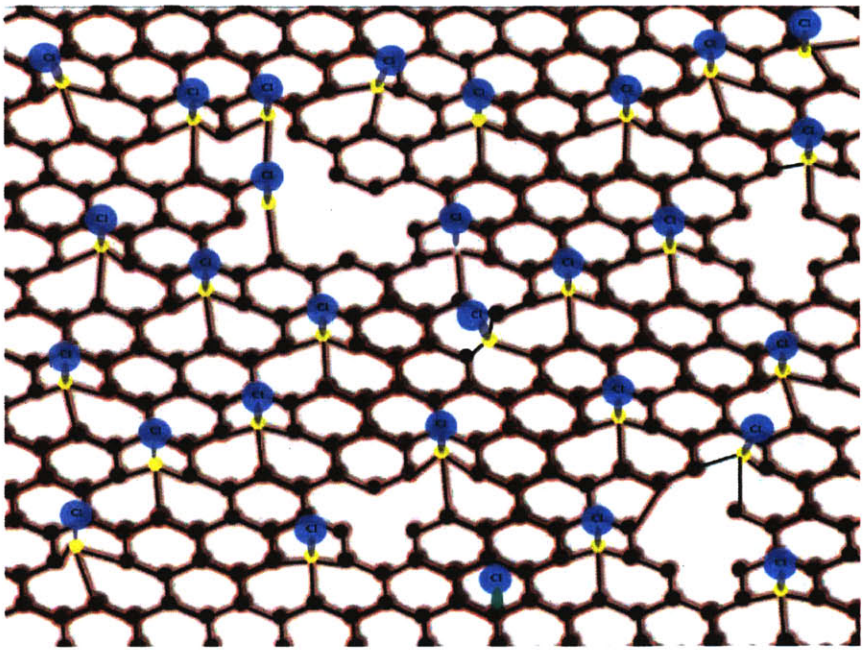

Figure 86 Schematica illustration of reactions between graphene and the chlorine plasma when the RF bias is high enough to be destructive

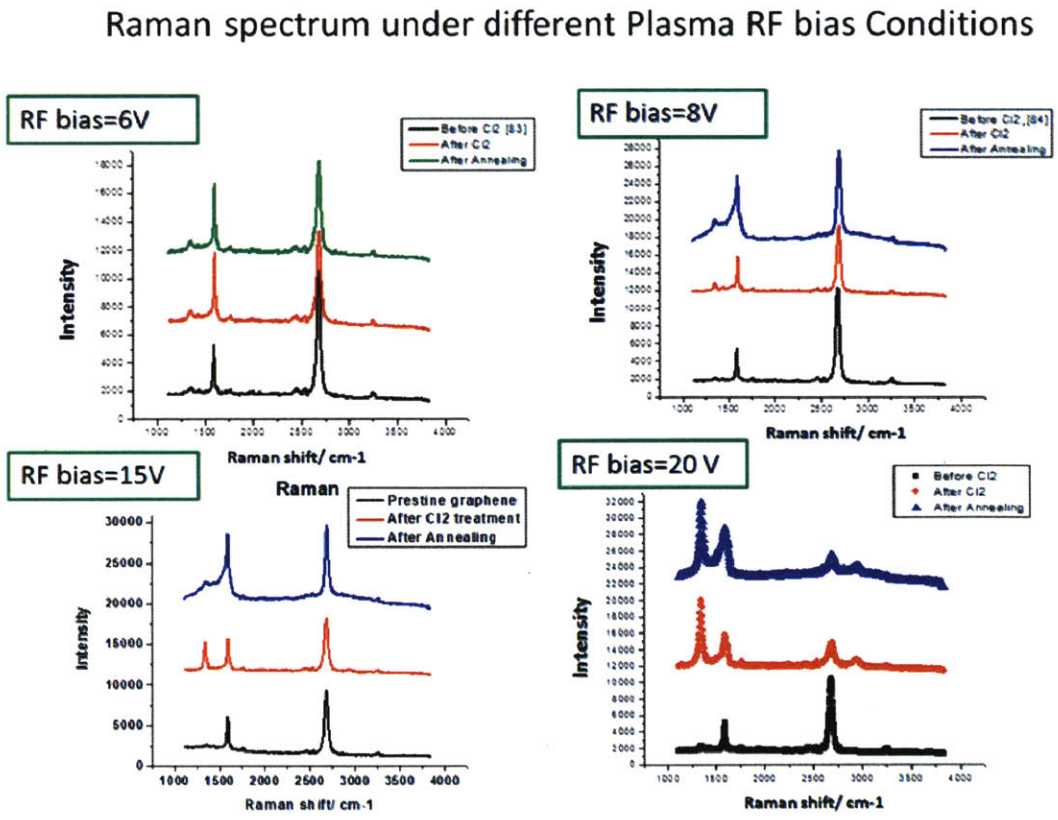

Figure 87 Raman spectrum for graphene flakes under chlorine plasma treatments with different RF bias voltages: (a) 6V, (b) 8V, (c) 15 V, (d) 20V.

It is worth pointing out a different reaction picture that is suggested by a theoretical study (figure 88), in which the author claimed that the different reaction stages between graphene and chlorine depends on the exposure of the graphene surface to chlorine atoms. [37]

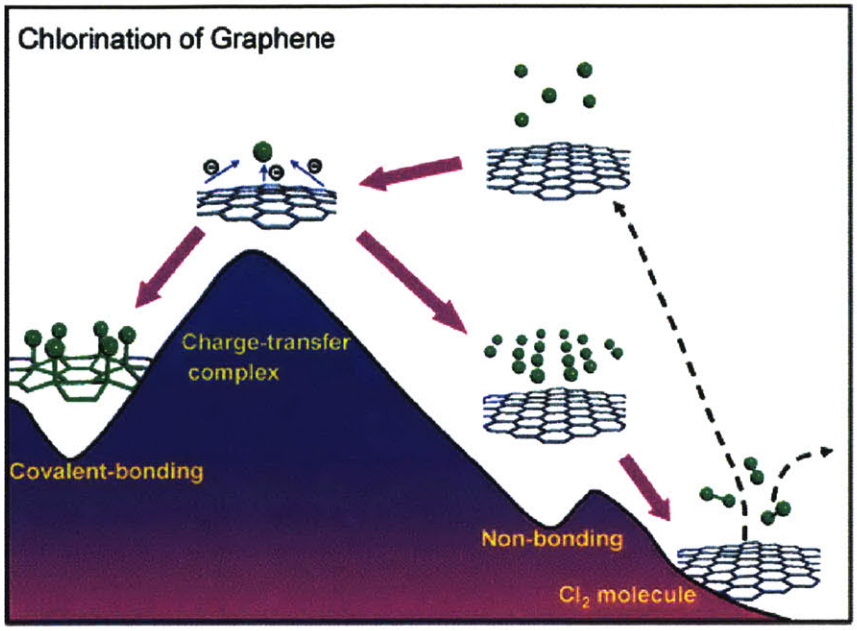

Figure 88 Schematic representation of the interaction between graphene and chlorine under different adsorption configurations. [37]

It should be noted that our experimental results are quite different from what DFT calculations predict. These numerical calculations predict that when the amount of chlorine is low, isolated chlorine atoms absorb on graphene to form charge-transfer complex. By further increasing the amount of chlorine, the chlorine atoms will get closer and closer to each other. Two configurations can happen on single-side exposed graphene: forming hexagonal Cl ring clusters via covalent bonding, or non-bonding. The non-bonding configuration is unstable and chlorine atoms will form chlorine molecules and escape, leaving the graphene available again for further chlorination. And these calculations predict that the most energy favorable configuration is random hexagonal Cl ring clusters on graphene, and therefore the coverage of chlorine will be less than 25%. [37] More work is necessary to explain the observed difference between experiments and DFT calculations.

3.6 Bandgap Engineering

Chlorination in graphene can transform the carbon hybridization from sp^2 to sp^3 and thus change its band structure. Pristine graphene is a purely sp^2 carbon structure, with a zero bandgap. Diamond is a purely sp^3 carbon crystal with the face center cubic structure, with large bandgap 5.5 eV [53]. By tuning the coverage of the chemical species functionalizing in graphene, it is possible to engineer its band structure, and especially its bandgap. Surface functionalization through hydrogenation and fluorination has been demonstrated to open a bandgap in graphene. However, both H and F will largely degrade the mobility in graphene, which limits the application of these dopants in semiconductor devices.

➢ DFT Calculations

DFT calculations predict that a bandgap can be opened through chlorination, and the size of the bandgap depends on the coverage of chlorine on graphene (by courtesy of Prof. Evan Reed's Group from Stanford University). The simulation results are summarized in the figure below.

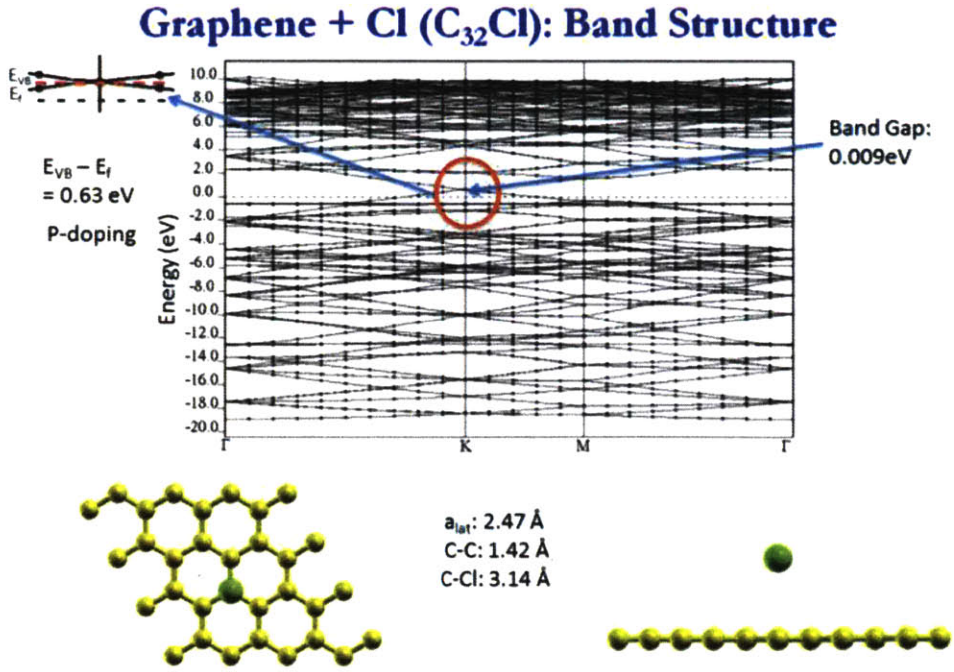

Figure 89 DFT calculation of band structure of chlorinated graphene $C_{32}Cl$ (by courtesy of the Evan Reed Group)

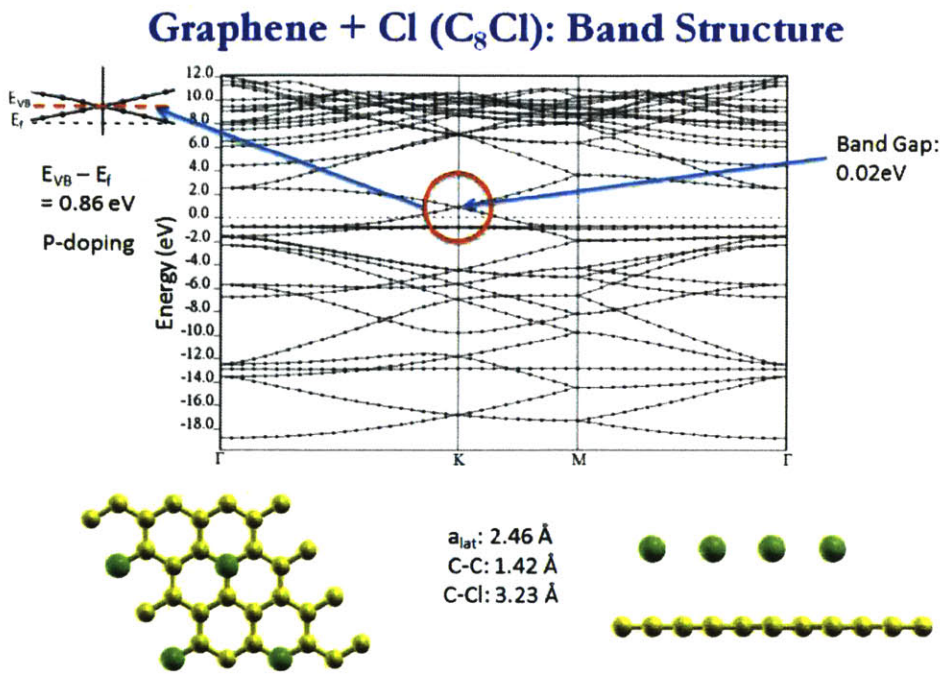

Figure 90 DFT calculation of band structure of chlorinated graphene $\underline{C_8Cl}$ (by courtesy of the Evan Reed Group)

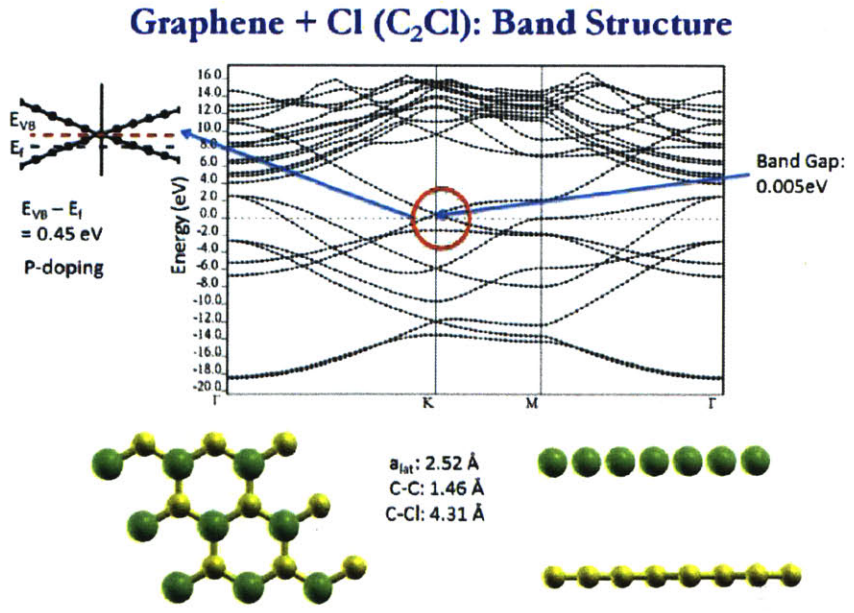

Figure 91 DFT calculation of band structure of chlorinated graphene $\underline{C_2Cl}$ (by courtesy of the Evan Reed Group)

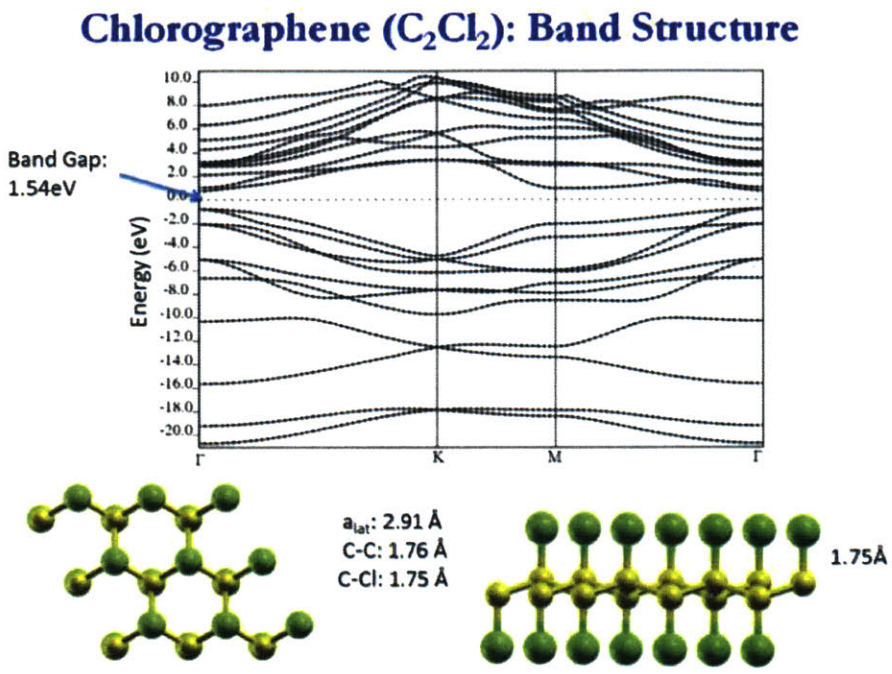

Figure 92 DFT calculation of band structure of double-side chlorinated graphene C_2Cl_2 (by courtesy of the Evan Reed Group)

From the DFT calculations, when graphene is chlorinated on only one side (C/Cl ratio from 32 to 2), the band structure is only slightly modified. A very small bandgap less than 50 meV is introduced in graphene, which is too small to be useful in electronic applications operating at room temperature. However, when graphene is double-side chlorinated and when the C/Cl ratio reaches 1 (C_2Cl_2), a bandgap as large as 1.54 eV can be opened. In this circumstance, the sublattice A of graphene is fully chlorinated and the other sublattice B is also fully chlorinated on the other side.

It is also interesting to investigate how the structural changes in graphene caused by chlorination affects the electronic structure. From the above DFT results, for $C_{32}Cl$, C_8Cl, and C_2Cl, the atomic lattice length are 2.47 Å, 2.46 Å and 2.52 Å, respectively. They are very close to pristine graphene's lattice constant 2.46 Å. We can find that the lattice structure is not altered much. Moreover, if we look at the C-C bond lengths, they are also close to 1.42 Å, the value of pristine graphene. The distance between C and Cl is from 3.14 Å to 4.31 Å. The large distances indicate that the bonding between carbon and chlorine is very weak, which is consistent with

the result that the graphene lattice structure is largely preserved. This is all consistent with the fact that the bandgap opening in $C_{32}Cl$, C_8Cl, and C_2Cl is negligible. Figure 93 summarizes the relation between the C/Cl ratio and the bandgap opening.

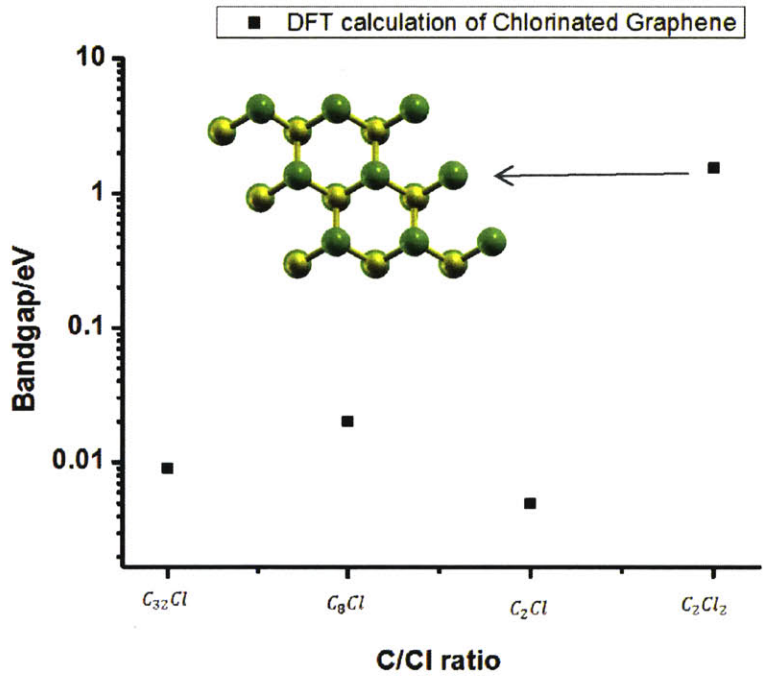

Figure 93 DFT calculations indicate the relation between C/Cl ratio and the bandgap opening

For double-side chlorinated C_2Cl_2, the situation changes significantly. First, the carbon and chlorine atom distance becomes much smaller than in single-sided chlorination, only 1.75 Å, indicating that the interaction between graphene and chlorine becomes much stronger (covalent bonding). Second, the carbon structure in graphene is largely distorted through double-sided chlorination. Upon Cl_2 doping, the lattice constant changes to 2.91 Å (2.46 Å for pristine graphene) and the carbon-carbon bond length becomes 1.76 Å (1.42 Å for pristine graphene). All these results support that the bonding between graphene and chlorine is very strong and the hybridization state of carbon atoms can be transformed from sp^2 to sp^3 configuration. Therefore, it is not surprising that a large bandgap 1.54 eV is predicted under this condition.

➢ Experimental Challenges

Up to now, we have not been successful in fabricating a chlorinated graphene FETs with a bandgap opening and current saturation. There are two main challenging obstables remaining to be overcome. Firstly, only when both sides of the graphene are functionalized by chlorine, is it possible to open a bandgap. This requires fabrication of a monolayer suspended graphene to make both sides of graphene accessible to chlorine plasma. The fabrication of these structures is quite challenging and still on-going. Secondly, chlorination heavily dopes the graphene p-type, and thereby the Fermi level will become far below the Dirac point after chlorination, as shown in Figure 94.

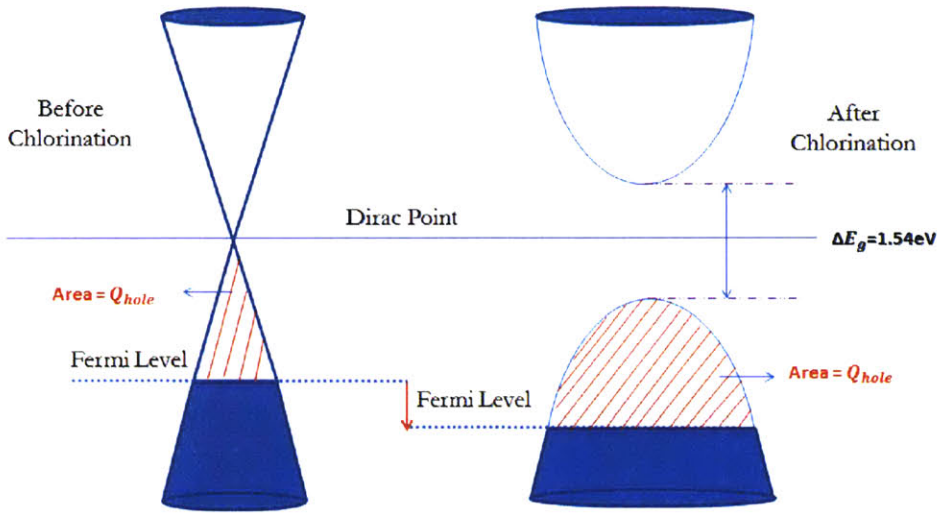

Figure 94 Schematic illustration of the bandgap opening in graphene after chlorination

The shadowed red area in figure 94 indicates the total amount of hole carrier charges in the chlorinated graphene. Even if we can open a bandgap as shown in the figure above, to take advantage of it in electronic devices, we have to tune its Fermi level into a position somewhere in the band gap. This can be done by applying a positive gate bias which can induce negative charges (electrons) in the channel and fill up the shadowed red area with carriers. And the Dirac voltage depends on the capacitance of the gate, as expressed in the equation below.

$$\Delta Q_{hole} = C * V_{gate}$$

We have to note that the concentration of hole carriers introduced by the chlorine dopants is very large, and the applied gate voltage V_{gate} cannot be too high, for otherwise, the graphene FETs will break down due to the electric field. Considering these two facts, we need a very high capacitance to fulfill any device requirements. And that is the second challenge we are still facing.

Chapter 4 Graphene Hydrogenation and Fluorination

Before our chlorination study, previous experimental results had already demonstrated alternative functionalization approaches, such as exposure to XeF_2 and F_2 and H_2 plasmas, and had shown that such approaches can significantly change the band structure of graphene and turn it into an insulator, with a bandgap from 2.9 eV to 5.4 eV [23], [36], [54], [55]. Besides the chlorination method via a plasma reaction, a photochemical process has also been shown to change graphene into an insulator [56]. However, all these methods are quite destructive to the graphene structure. It is therefore interesting to compare our chlorination results with the prior hydrogenation and fluorination studies, and to show that that the proposed chlorination technology is more suitable than other surface treatments to engineer the band structure of graphene.

4.1 Hydrogenation in Graphene

We investigated plasma-based hydrogenation in exfoliated samples. The experimental setup, sample preparation and physics behind the hydrogenation of graphene are all similar to our own previous chlorination studies, so we will not duplicate the explanation here. The treatment parameters are summarized in Table 3.

Table 3 Experimental parameters for the hydrogenation plasma reaction

Gas	Flow rate/sccm	Pressure/mTorr	ECR power/Watts	RF bias/V	Temperature/C	Time/sec
H_2	3	5	60	7.8	25	30
Ar	10					

The reaction conditions that we chose for the hydrogen plasma experiments are different from those that were used for the chlorine plasma. The reason is that, as we will see later in this chapter, the reaction between hydrogen and graphene is extremely fast and the graphene layer would be badly etched away if we would choose the same conditions. To choose the optimum processing conditions, we control the plasma conditions so as to find the minimal parameters needed to activate the plasma and to keep the flow rate stable, i.e. to make the surface functionalization effective but reduce as much as possible the potential damage. Figure 95 shows an example of the exfoliated graphene flakes were investigated in this study.

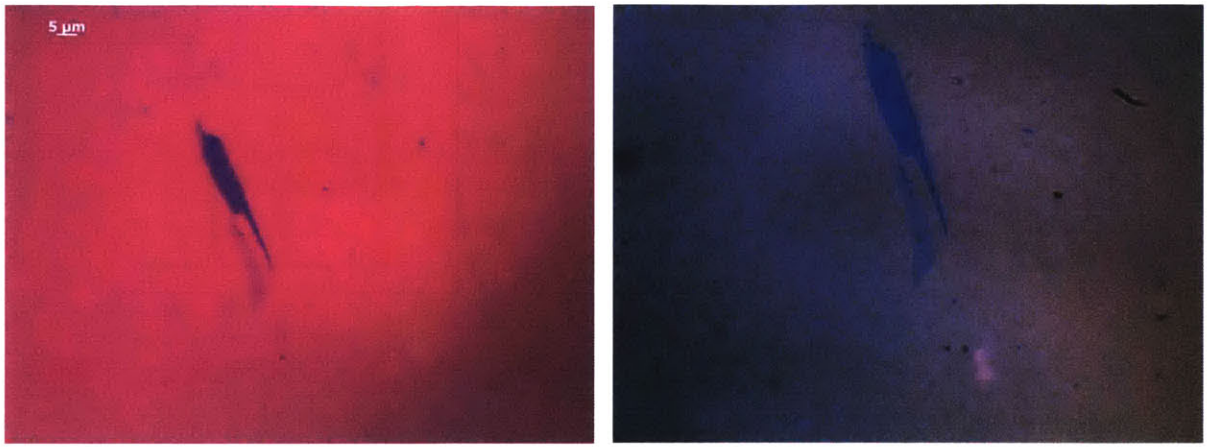

Figure 95 Left: optical image of exfoliated graphene flakes before the plasma reaction

Right: optical image of exfoliated graphene flakes after the plasma reaction

We measured the Raman spectrum of one of the graphene flake samples before and after hydrogenation. The results are shown in Figure 96. The Raman results of hydrogenated graphene after annealing are also included in this figure. The annealing was conducted in an argon gas environment for 4 hours at 400 ℃. The flow rate of Ar is kept at 800 sccm.

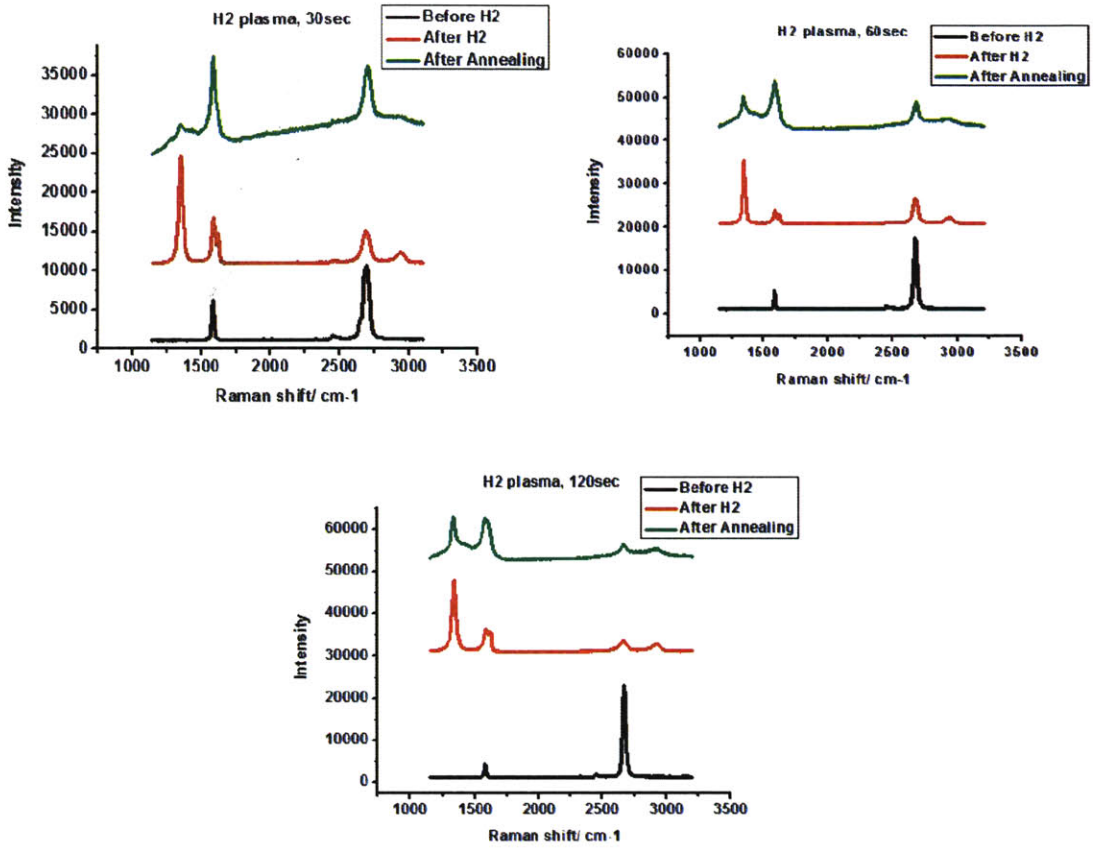

Figure 96 Raman spectra of graphene flakes under different hydrogen plasma treatment conditions. Black line: graphene before hydrogenation. Red line: graphene after hydrogenation. Green line: hydrogenated graphene after hydrogenation and annealing.

Comparing with graphene chlorination, the Raman spectra in Figure 96 exhibited a similar response. First of all, the defect-related D peak intensity centered at 1350 cm^{-1} and the D+D' peak intensity centered at 2970 cm^{-1} increased dramatically. Meanwhile, the G'/G intensity ratio significantly decreased. These results indicate the presence of defects in graphene crystal structure. It is worth pointing out that the D peak can be largely diminished after annealing in the graphene samples which were only treated for 30 seconds in hydrogen plasma. The longer the exposure time to the hydrogen plasma, the higher the D peak intensity that was left after annealing. Moreover, the longer time the graphene samples were exposed to hydrogen plasma, the lower the G'/G peak intensity ratio after hydrogenation.

If we look into the G peak in more detail (Figure 96), a D' peak centered at ~1620 cm^{-1} was also induced by the hydrogen plasma, and this D' peak is again a defect-activated mode. Unlike the

chlorination, we did not find a blue shift in G peak here. The G peak did not move in frequency after hydrogenation and/or after annealing.

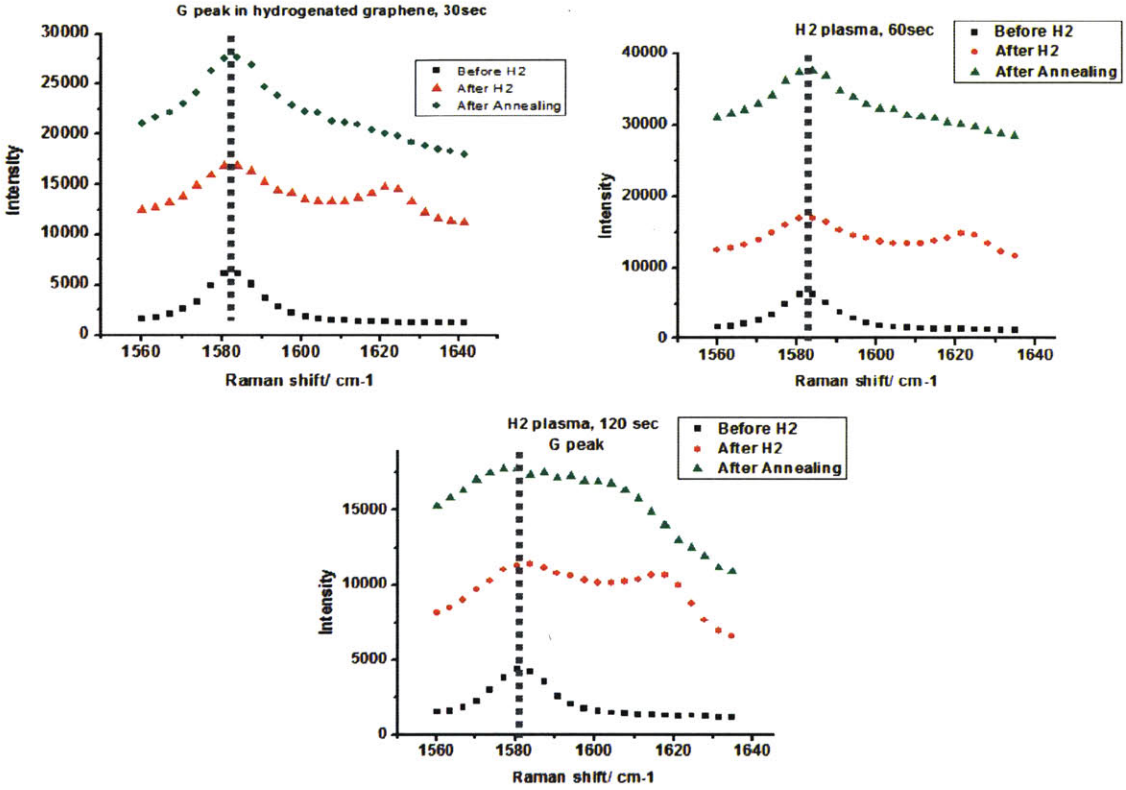

Figure 97 Effect of hydrogenation on the G peak in the Raman spectrum of graphene for different length of time (labeled in the title of each figure) of exposure to the hydrogen plasma. Black line: graphene before hydrogenation. Red line: graphene after hydrogenation. Green line: hydrogenated graphene after annealing

The transport properties of the hydrogenated graphene FETs were also investigated. Figure 98 shows how the resistance of the graphene FETs changes after hydrogen plasma treatment. The samples used in Figure 98 were exposed in hydrogen plasma for 30 seconds, and the reaction parameters were the same as the ones in Table 3.

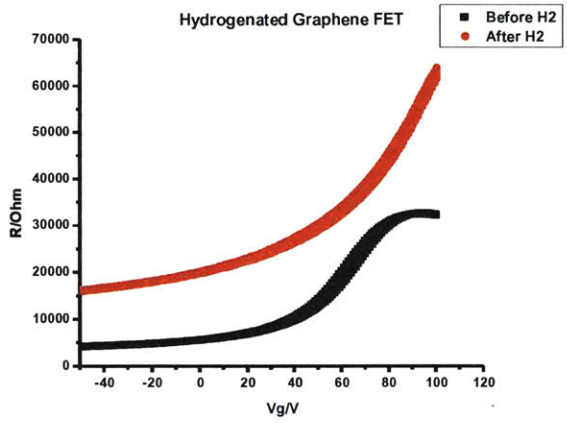

Figure 98 The change in resistance of graphene FETs before and after hydrogenation

As shown in Figure 98, the resistance of the graphene FET increased after hydrogenation, which is quite different from the chlorination results we discussed previously. Two possible reasons that may account for this observation. One is that hydrogenation is more destructive to graphene than the chlorination process. The hydrogen plasma created too many defects in graphene so that the increased defect scattering led to an increased resistance. The other potential explanation is that the hydrogenation process fundamentally changed the band structure of graphene and opened a large bandgap (the band parameters are changed significantly), i.e. the "hydrogenated graphene" became an insulator. Further experimental investigations are needed to find out what is the exact reason that results in the dramatic change in graphene's resistance. Moreover, the Dirac voltage shifts in the p-type direction, suggesting a hole doping scenario. In order to further understand better these observations, we measured and compared the carrier concentration, sheet resistance and mobility before and after hydrogenation. The results are shown in Figure 99, 100 and 101, respectively.

Figure 99 shows that the carrier (hole) concentration in graphene increases after hydrogenation, from $5 \times 10^{12}\ cm^{-2}$ to $7.5 \times 10^{12}\ cm^{-2}$ (Figure 99). Similar to the chlorination in graphene, the hydrogen plasma tends to induce hole doping in graphene: its hole concentration increased about 50%. As a comparison, the carrier concentration in graphene increased about 3 to 4 times after chlorination. We can see that the chlorination is much more efficient than hydrogenation in terms of hole doping. This can be explained by a higher electronegativity of chlorine than the one in hydrogen.

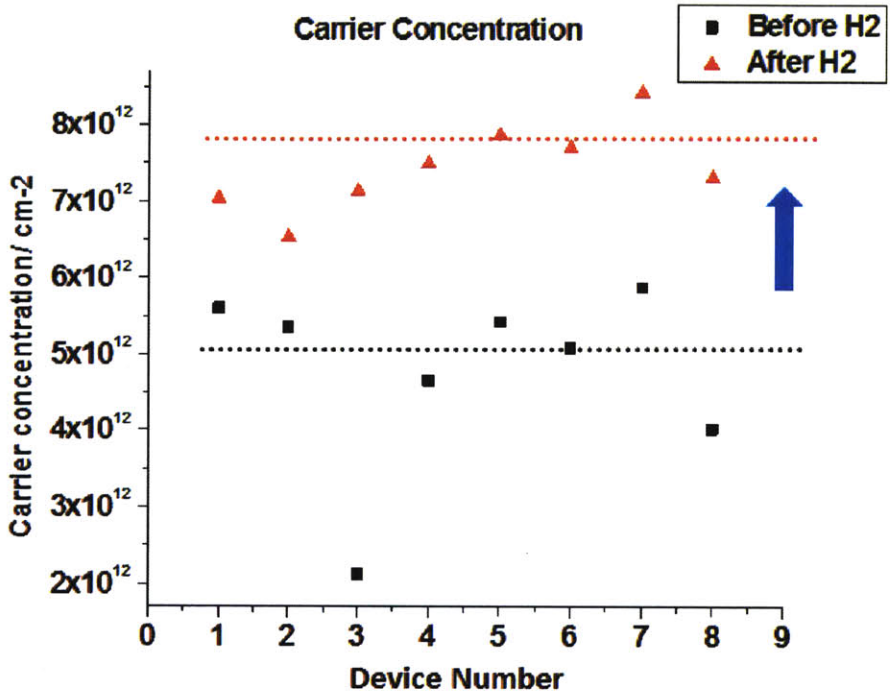

Figure 99 The change in carrier concentration of the graphene FETs before and after hydrogenation. The dashed black (red) line indicates the average value of carrier concentration of the devices before (after) hydrogenation

We also measured the change in sheet resistance of the hydrogenated graphene. After the hydrogen plasma treatment, the graphene became more resistive, as indicated in Figure 100. This is consistent with the result shown in Figure 98. This is opposite to the result obtained in the chlorinated graphene sample, where the resistance dropped with chlorination, as we mentioned previously (Figure 78). Therefore, we can find a distinctive difference between hydrogenation and chlorination: hydrogenation makes graphene more resistive, while chlorination makes graphene even more conductive.

The relation between carrier concentration, mobility and conductivity can be expressed as:

$$n \cdot \mu = 2.42 \times 10^4 \cdot \sigma ,$$

where, n represents the carrier concentration (in units of $10^{10}\ cm^{-2}$), μ is the mobility (in units of $cm^2/V \cdot s$) and σ is the conductivity (in unit of e^2/h) [52]. From Figure 99, we know that the the carrier concentration in hydrogenated graphene increased after hydrogen plasma

treatment, which should lead to an increased conductivity, i.e. a decreased resistance, according to the equation above. However, we found (Figure 98 and Figure 100) exactly the opposite: an increased resistance. This result indicates that the mobility in hydrogenated graphene must drop significantly, more than the amount that the hole concentration increased, which is confirmed in Figure 101.

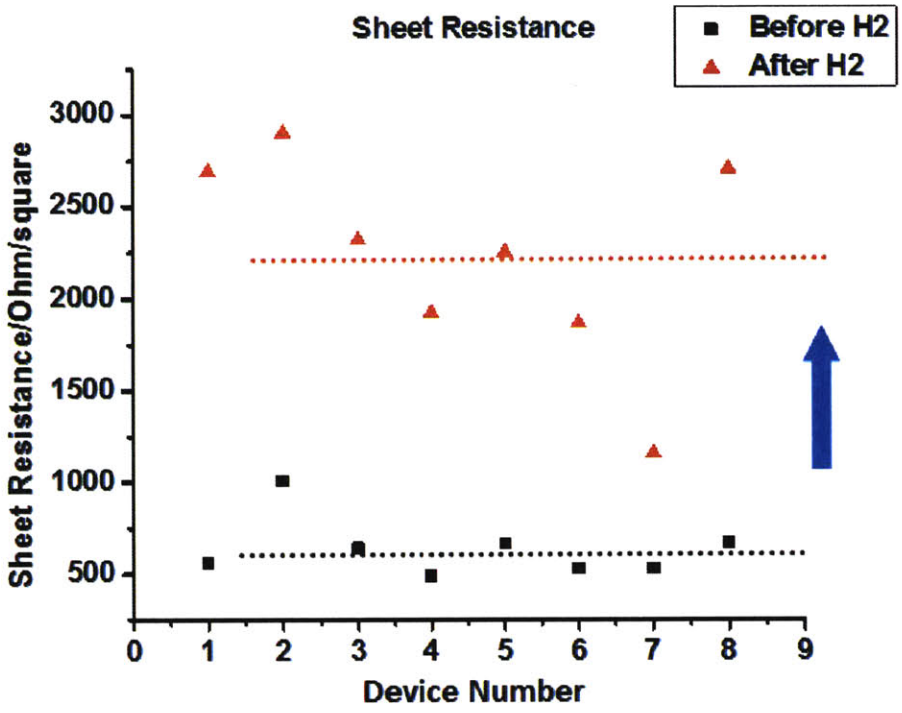

Figure 100 The change in the sheet resistance of the graphene FETs before and after hydrogenation. The dashed black (red) line indicates the average value of sheet resistance of the devices before (after) hydrogenation. The length of treatment time is 30 second.

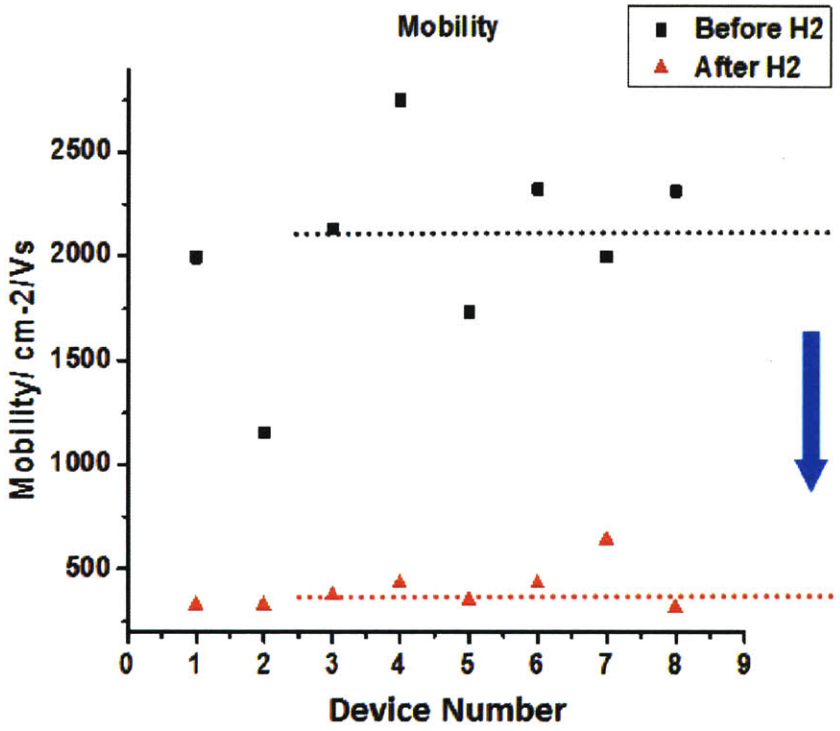

Figure 101 The change in the mobility of the graphene FETs before and after hydrogenation. The dashed black (red) line indicates the average value of the mobility of the devices before (after) hydrogenation

The mobilities in graphene FETs decreased from around 2000 $(\pm 500)\ cm^2/Vs$ to less than 500 $(\pm 200)\ cm^2/Vs$ after hydrogenation. Comparing with hydrogenated graphene, the mobilities of graphene after chlorination are about two times higher, around 1000$(\pm 200)\ cm^2/Vs$. The Geim Group showed a similar result on graphene hydrogenation, in which the mobility dropped from 14,000 cm^2/Vs to about 10 cm^2/Vs [23]. Our measurements here showed much less mobility degradation than their results. This may be due to weaker RF bias applied in the hydrogen plasma chamber and shorter treatment time used in our experiments.

It is also interesting to examine how the hydrogenated graphene's properties change after annealing. The annealing was again done in an argon gas environment at 400 ℃ for four hours under atmospheric pressure conditions. The flow rate was maintained at 800 sccm. We found that the mobility of hydrogenated graphene increased a little after annealing, but is still much lower than the original value, as shown in Figure 102. At the same time, the sheet resistance can also be partially, but not fully, recovered (Figure 103). The partial reversibility in hydrogenated

graphene's mobility indicates that both increased defect-induced scattering and increased electron-phonon scattering play a role in the mobility degradation of the hydrogenation process. Defect scattering must exist, because if not, graphene's mobility would be fully recovered after the hydrogen atoms escape from the graphene surface during annealing. Furthermore, the hydrogen plasma also changes the atomic structure of graphene and partially transforms the sp^2 hybridization to a sp^3 configuration (a sizeable bandgap may also be opened up at the same time), which makes the "hydrogenated graphene" no longer a simple two-dimensional structure. It is likely that the electron-phonon scattering is modified. The reason is that the mobility of our graphene samples would not be recovered at all if otherwise the defect creation is the only factor that accounts for the drop in the graphene mobility. The 400 ℃ temperature at which we annealed the samples is not high enough to heal the defects.

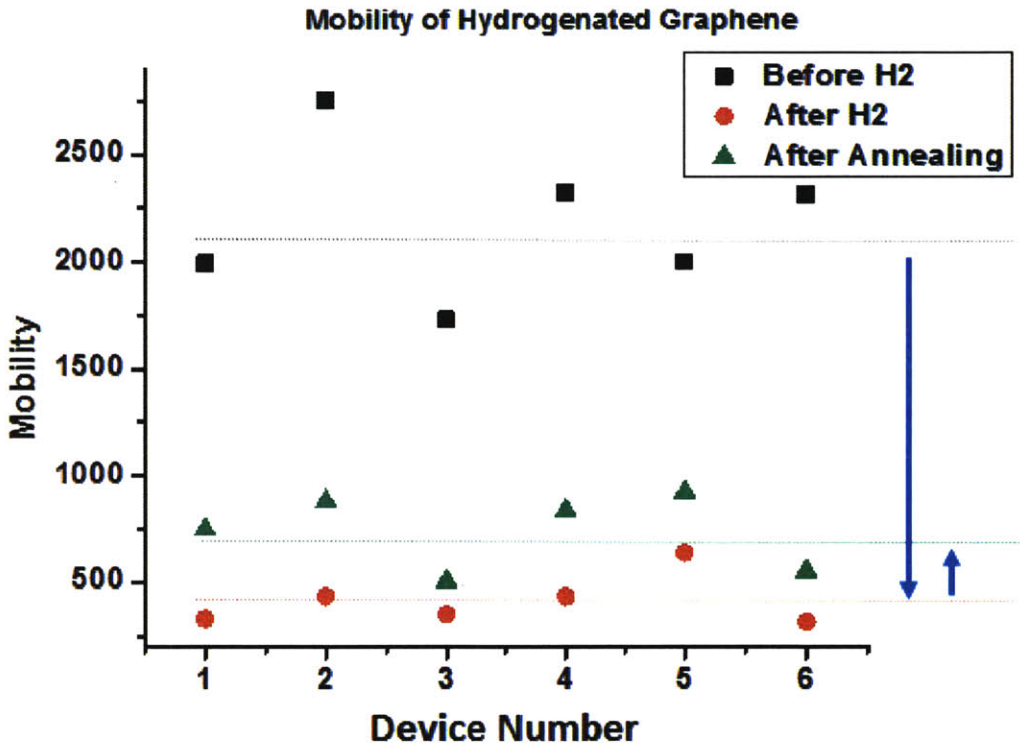

Figure 102 The change in the mobility of the graphene FETs before and after hydrogenation. The dashed black (red) line indicates the average value of mobility of the devices before (after) hydrogenation. The dashed green line represents the average level of mobility after annealing in an argon gas at 400 °C for four hours.

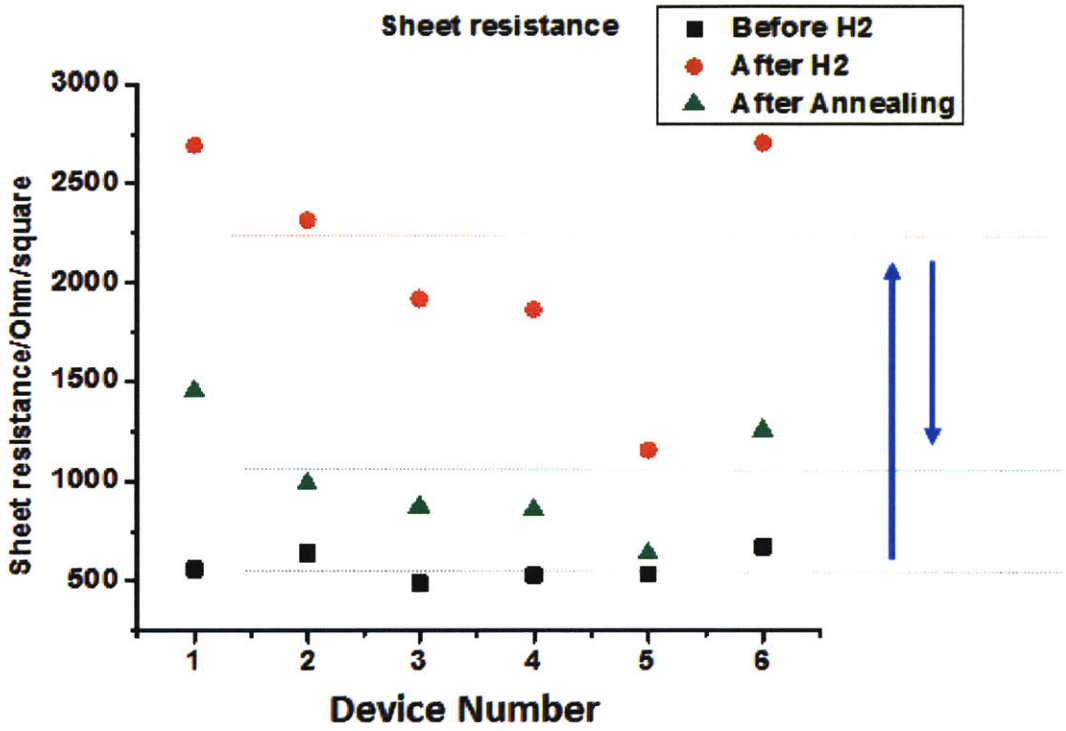

Figure 103 The change in the sheet resistance of the graphene FETs before and after hydrogenation. The dashed black (red) line indicates the average value of sheet resistance of the devices before (after) hydrogenation. The dashed green line represents the average level of sheet resistance after annealing in argon gas at 400 °C for four hours

4.2 Fluorination in Graphene

Fluorination in graphene was also investigated as a comparison, through a slightly different approach was used in this case. The pristine graphene samples were exposed to a fluorinating agent, i.e. XeF_2 at room temperature and around 2 Torr of pressure. Unlike hydrogenation and chlorination, no power or bias was applied to energize XeF_2 molecules and thus no plasma was generated. If a plasma had been used, it is expected that the graphene would have been severely damaged. XeF_2 can easily decompose on graphene into atomic fluorine, which is highly reactive [54].

We measured the Raman spectrum of graphene samples before and after XeF_2 exposure. The Raman results after annealing were also examined and these results are included in Figure 104. The samples were exposed to XeF_2 gas for different durations: 30 seconds, 60 seconds and 150 seconds, respectively.

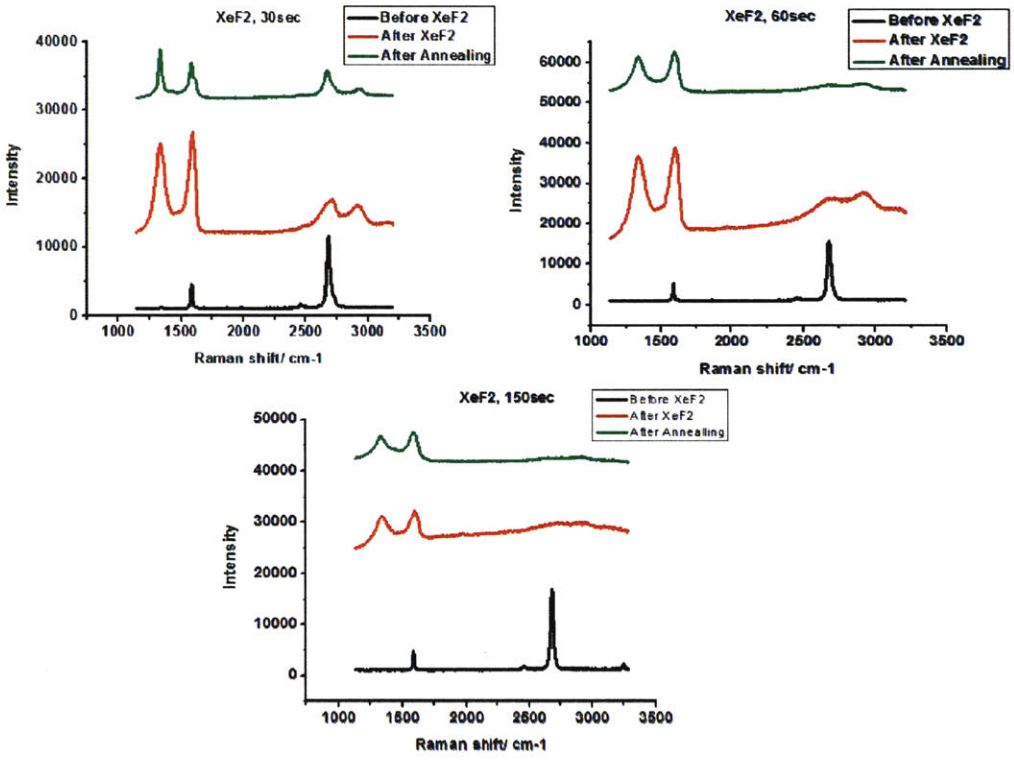

Figure 104 The Raman spectrum of graphene samples before fluorination, after fluorination and after annealing. The reaction times are 30 seconds, 60 seconds and 150 seconds as labeled in the figure. The annealing was done in an argon environment for 4 hours at 400°C.

From Figure 104, we find that the Raman response to fluorination is similar to the results of chlorination and hydrogenation. The defect-activated modes: D peak (1350 cm^{-1}), D' peak (1620 cm^{-1}) and D+D' peak (2970 cm^{-1}) all increased substantially after fluorination. However, these defect-related peaks did not decrease at all after annealing. Moreover, we found that longer XeF_2 exposure time did not result in a higher D/G intensity ratio (integrated area ratio under each peak in the Raman spectrum). However, a longer XeF_2 treatment did lead to a weaker G'/G peak intensity ratio.

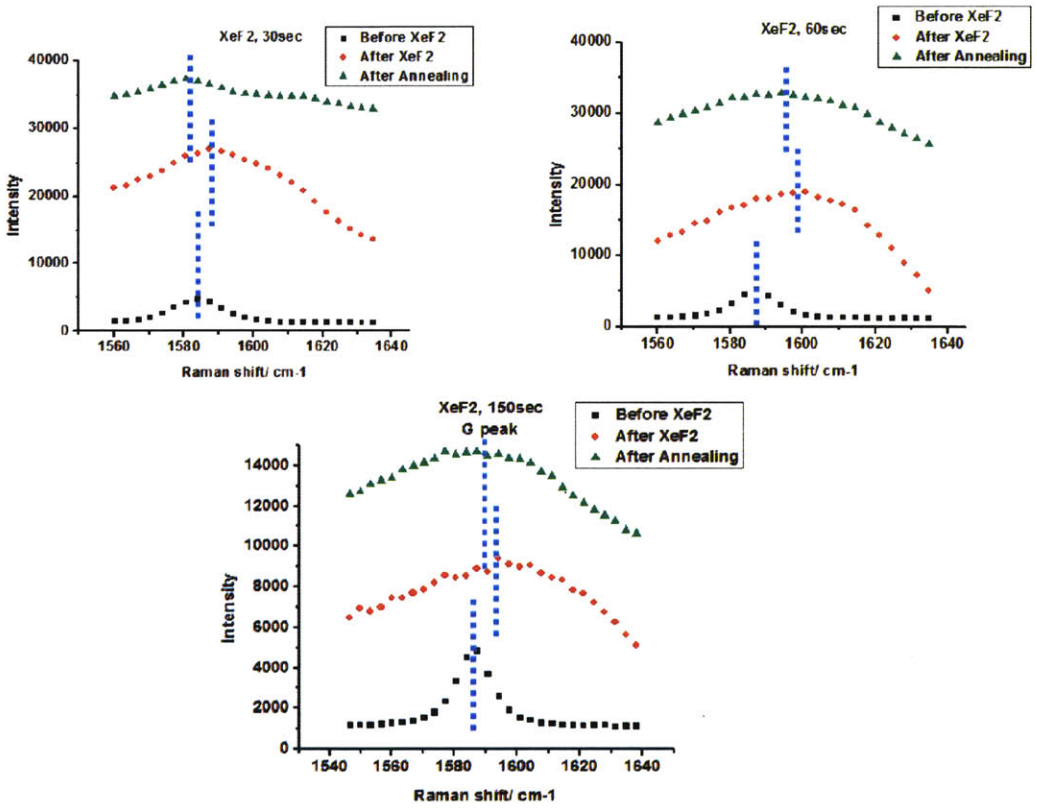

Figure 105 The Raman spectrum of graphene samples before fluorination, after fluorination and after annealing, for different reaction time. The reaction times are 30 seconds, 60 seconds and 150 seconds as labeled in the figure

Similar to the chlorination results, fluorination also results in a blue shift in the G peak of graphene's Raman spectrum, as shown in the Figure 105. This is easy to understand because the electronegativity of fluorine is even higher than in chlorine. A larger electronegativity means a stronger capability to gain electrons from other atoms [57]. Therefore, fluorine can also grab an electron from carbon's π bond and dope graphene with a hole, i.e. p-type doping, and thus we find a blue shift in G peak of graphene's Raman spectrum. It is interesting to note that after annealing, the G peak red shifts back a little. This result suggests that many fluorine atoms return the electrons back to graphene's π bonds (n-type doping process) when they escape from the graphene surface during annealing. Significantly, the

FWHM of the G peaks in the Raman spectra also increased. This indicates that a variety of carbon fluoride CF_x compounds may be formed during the XeF_2 treatment, and each of these carbon fluoride compounds has quite different electronic structures. In order to understand better this fluorination process, we also characterized the transport properties of fluorinated graphene. The graphene FETs were exposed to XeF_2 gas for only 20 seconds.

Figure 106 shows how the resistance of graphene FETs change after a 20 second exposure to XeF_2. It is found that fluorination can make graphene an insulator: its resistance increased from several hundreds of Ohm to more than 100,000 Ohm. After annealing in an argon environment for 4 hours at 400℃, its resistance dropped to less than 1000 Ohm, but still higher than its original resistance before fluorination. This process is largely reversible, meaning XeF_2 does not create too many defects in graphene. However, by bonding with carbon atoms in graphene, XeF_2 substantially deforms the crystal structure of graphene and transforms it into an insulator.

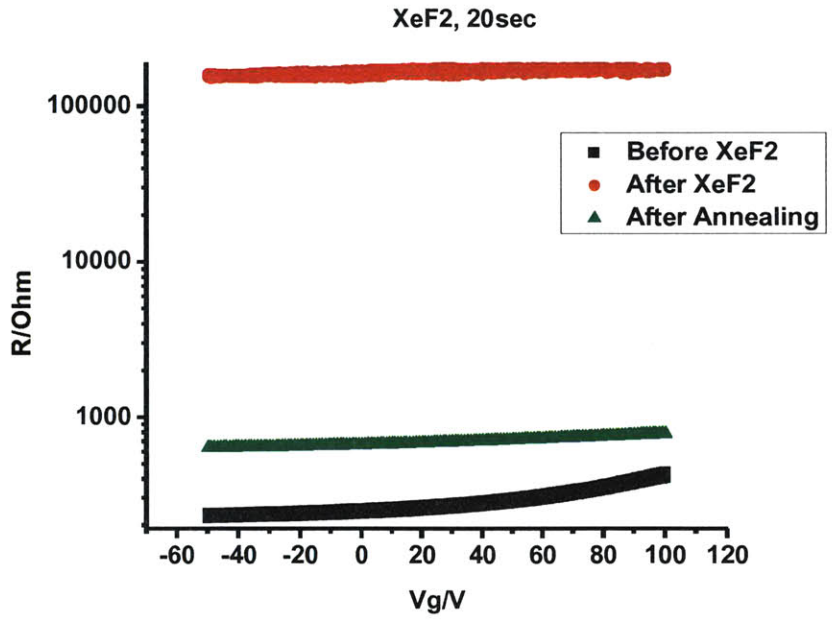

Figure 106 The change in resistance of fluorinated graphene FET after fluorination and after annealing

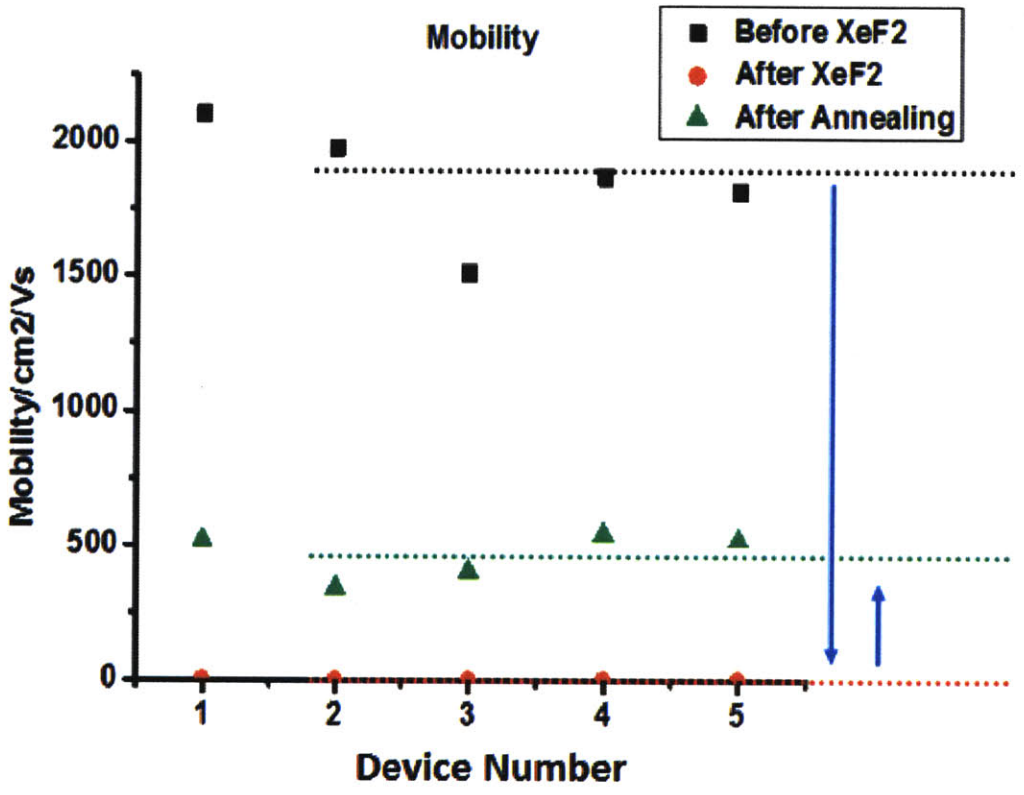

Figure 107 The change in the mobility of fluorinated graphene FET after fluorination and after annealing in an argon environment for 4 hours at 400°C

If we examine the change in fluorinated graphene's mobility, a consistent argument can be made here. After the reaction with XeF_2, the mobility in graphene was signifincatly reduced (beyond the resolution of our measurement setup). After annealing, its mobility partially recovered back to 300-500 cm^2/Vs. Considering all these observations, we think it is very likely that besides the defect creation and doping that happened during fluorination, XeF_2 also significantly altered the band structure of graphene, introduced a large bandgap, i.e. the fluorinated graphene became an insulator, and therefore we see the resistance of graphene increased by more than 100 times after fluorination. And the carbon atoms transformed their pure sp^2 hybridization to sp^3 configuration to some extent, which resulted in an increased electron-phonon scattering and largely degraded the mobility in graphene as we see in Figure

107. In order to confirm these conjectures, further experiments are needed to investigate the atomic structure of fluorinated graphene.

In summary, from the Raman and transport perspectives, we find that hydrogenation degrades the mobility of graphene much more than chlorination, and fluorination could degrade the mobility even more than hydrogenation. The possible reason can be change in the electronic structure itself, as well as an increased defect scattering and/or electron-phonon scattering. The controllability of chlorination and the preservation of high mobility in chlorinated graphene make it a competitive approach to realize surface functionalization in graphene.

Chapter 5 Conclusions and Future Plans

We systematically investigated the chlorination in graphene via plasma reactions and characterized the samples with Raman spectroscopy, X-ray photoelectron spectroscopy, atomic force microscopy (AFM) and transport measurements. The reaction mechanism between graphene and a chlorine plasma was analyzed in some detail. Plasma-based hydrogenation and fluorination of graphene layers were also performed and compared with chlorinated graphene properties. In this section, we will summarize the features of graphene chlorination and highlight its unique advantages over other surface functionalization approaches. Future challenges ahead and further plans for me to pave the way for its real applications of functionalized graphene are also discussed.

5.1 Conclusions

➢ Advantages of chlorination

First and foremost, chlorination via plasma reactions does not significantly degrade the high mobility in graphene. After chlorination, the mobility for CVD graphene is still about 1000 cm^2/Vs, which is still very competitive with silicon. It is expected that the mobility for exfoliated graphene after chlorination can be even higher. For comparison, the hydrogenated graphene by mechanical exfoliation exhibited a mobility degradation from 14,000 cm^2/Vs to 10 cm^2/Vs [23]. And there are experiments showing that the mobility in exfoliated graphene after fluorination will drop to about 150 cm^2/Vs [54]. It is also possible to chlorinate graphene through a photochemical process, however, the mobility of the chlorinated graphene obtained by this method drops from 5000 cm^2/Vs to only 1 cm^2/Vs [56]. The fast damage and severe mobility degradation caused by these methods significantly limit their applications in electronic devices. The preservation of a high mobility in chlorinated graphene provides a very important advantage over other known approaches.

Secondly, a chlorine coverage on graphene as high as 40% can be reached, i.e. the C:Cl ratio is 2.5:1, on single-side exposed graphene. This is already very close to the theoretical maximum limit of 50% (C:Cl=2:1). Furthermore, both hydrogenation and fluorination also showed high surface coverage. This coverage is much higher than what has been reported so far via the photochemical processes (i.e. Cl coverage of only 8%) [56].

Thirdly, the reaction rate between graphene and chlorine is very fast. It saturates within the first 30 seconds, which makes this method very efficient and convenient.

Last, but not least, the plasma reaction between carbon and chlorine is much more controllable than the hydrogenation and fluorination. By tuning the RF bias of the plasma, we can control the reaction at different stages. At low RF bias, the chlorination process is a purely charge transfer

process, showing controlled doping, without changing the hybridization state of the carbon atoms, which is difficult to achieve by using H_2 and F_2. At higher RF bias, we can transform the sp^2 bonding to the sp^3 configuration, which, according to DFT calculations, should open a bandgap of up to 1.54 eV.

➢ Reaction Mechanisms

The reaction mechanisms of a chlorine plasma on graphene have been less investigated in the literature. There are quite a few theoretical papers have been published [37], but very limited experimental results. In this thesis, we have used Raman, XPS and transport results to suggest a potential mechanism of how the chlorine plasma interacts with a graphene surface, as summarized in Figure 108.

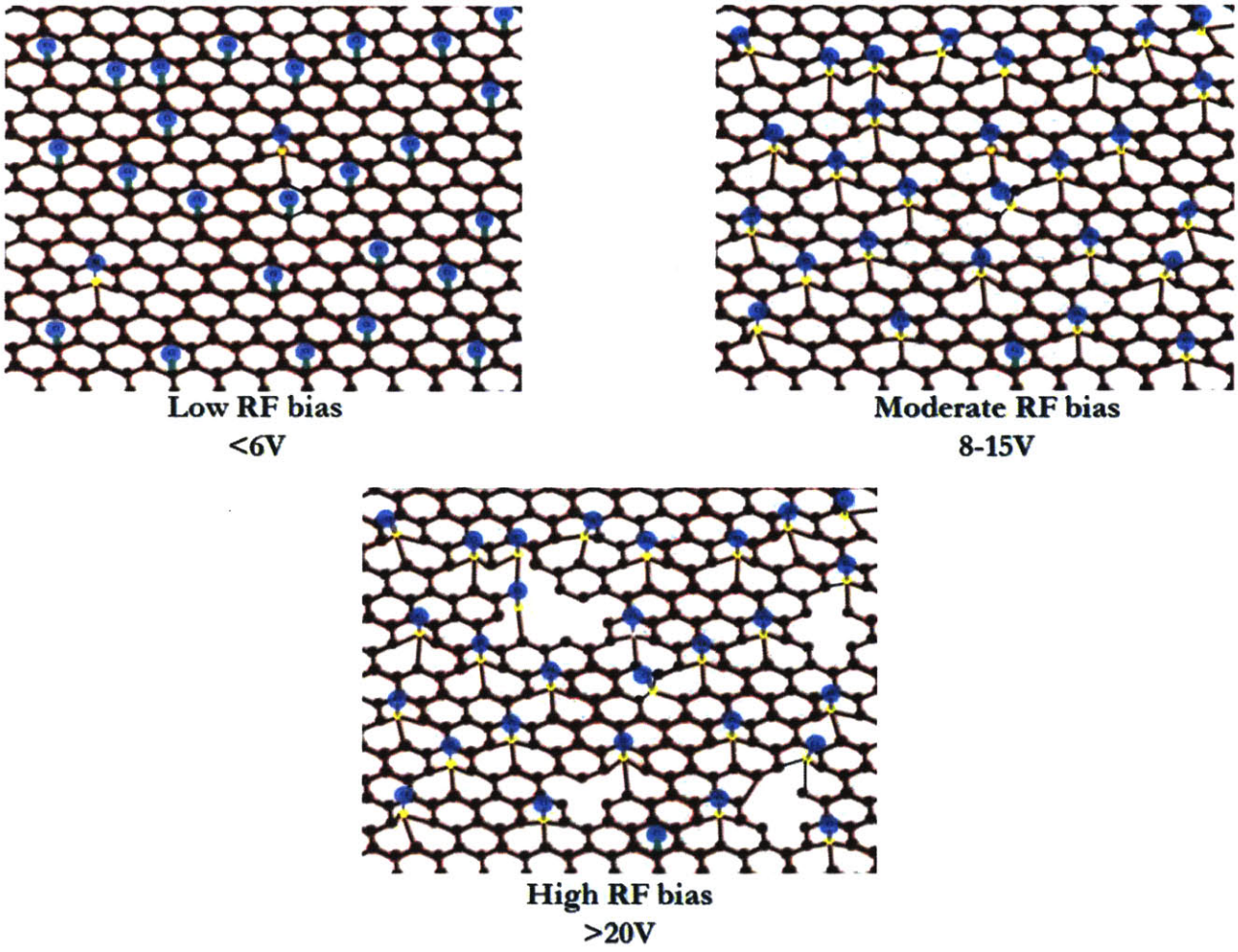

Figure 108 Schematic picture of the reactions between graphene and chlorine plasma under different RF bias conditions. (a) at low RF bias <6V, (b) at moderate RF bias 8-15V, (c) at high RF bias >20V.

The reaction between carbon atoms and chlorine atoms critically depends on the energy of the plasma, which is controlled by the RF bias. When the RF bias voltage is low, the chlorine only transfers charges to the graphene, i.e. resulting in p-type doping. The graphene remains in its flat structure with sp^2 carbon bonding.

As the RF bias is increased, the chlorine plasma becomes more and more energetic and it is able to change the hybridization state of the carbon-carbon bonding. And at some point, the sp^3 bonding type will become dominant. As a consequence, the graphene structure will be deformed and no longer flat. The angle between the carbon-carbon bonds will make a transition from 120° to some value closer to 109°. The Raman spectrum will then show an increased D/G intensity ratio due to the broken symmetry in the graphene structure. The significant hole doping will enhance the electron-electron scattering, while the sp^2 to sp^3 transition will increase the electron-phonon scattering. Both of them will lead to a mobility degradation from ~ 2000 cm^2/Vs to ~ 1000 cm^2/Vs. When the RF bias voltage is further increased, the plasma will eventually become energetic enough to "knock-off" the carbon-carbon σ bonds. Defects are created during this stage, which also results in an increased D/G ratio in the Raman spectra, which cannot be recovered by annealing.

As we mentioned previously in chapter 3, there is theoretical work suggesting that the different reaction stages between graphene and chlorine depends on the exposure of the graphene surface to chlorine atoms. This is different from the reaction mechanisms that we come up with here. In addition, these calculations predict that the configuration of random hexagonal Cl ring clusters on graphene is most energy favorable, and thus the coverage of chlorine would be less than 25% [37]. This is also different from our experimental results. Further investigation is needed to understand the difference between our experiments and theoretical predictions.

5.2 Future Research Implications

In this thesis, we fabricated graphene-based FETs and did surface functionalization via chlorine plasma reaction. With this, we investigated experimentally how the chlorination alters the structural and electrical properties of graphene. The reaction mechanism was also analyzed. In this section, we describe some future research efforts that are needed in order to further advance our understanding of surface functionalization in graphene and to facilitate the bandgap engineering in graphene devices.

➢ Bandgap Opening

One of the most important motivations for this study is to create a sizeable bandgap in graphene for digital electronic applications. There are two main challenges ahead in this project, as we discussed in the section 3.6. First, one has to fabricate freely suspended graphene in order to functionalize both sides of graphene. This is technically challenging. Second, in order to be able to tune the Fermi level into the band gap region, we need dielectric materials with very high capacitance, due to the significant p-type doping effect caused by chlorination. One way to address this challenge is to choose high-k dielectric materials. Another possible solution is to make the top gate and back gate function together to induce enough charges in the graphene. However, to integrate this fabrication with suspended graphene devices is quite challenging.

➢ Transmission Electron Microscopy (TEM)

It is very important to conduct TEM characterization of chlorinated graphene samples. TEM can provide direct evidence about the macroscopic continuity of the graphene samples after chlorination. It is necessary to examine if the chlorinated graphene remains homogeneous in the crystal structure after some time [58]. Also, by taking diffraction patterns, we can get the lattice constant of chlorinated graphene and compare it with the DFT calculations. The changes in lattice constant and in the carbon-carbon bond angle provide direct evidence of the sp^2 to sp^3 transition. [23].

➢ Scanning Tunneling Microscopy (STM)

STM can help us investigate the microscopic structure of chlorinated graphene. It is also a convincing way to determine the change in the carbon-carbon bonding length and carbon-chlorine bonding length, which are both very important for understanding the chlorine doping effect. Both STM and TEM investigation can help us examine the planarity of graphene after surface functionalization.

- **Strain Sensor Devices**

Another important motivation to investigate surface functionalization is to engineer piezoelectricity in graphene. Through chlorination, we are expecting to break the inversion symmetry in graphene, and thereby to introduce piezoelectricity as a new direction for graphene research [24].

In summary, in this thesis we demonstrated that chlorination in graphene via a plasma reaction is a very effective and controllable way to realize surface functionalization in graphene, and to engineer its structural and electronic properties. It is possible to reach high coverage of chlorine on graphene, without changing the carbon hybridization states. By carefully tuning the RF bias in the plasma chamber, we can turn a sp^2 bonding into sp^3, while largely preserving the high mobility in graphene. A detailed description of the reaction mechanism in chlorination has been provided. Hydrogenation and fluorination were also conducted and analyzed as comparison. It was found that the controllability and high mobility preservation in chlorinated graphene are important advantages over other functionalization approaches. These results confirm that chlorination via plasma reactions provides a powerful tool to improve graphene's suitability for future electronics.

List of Reference

[1] K. S. Novoselov, A. K. Geim, S. V. Morozov, D. Jiang, Y. Zhang, S. V. Dubonos, I. V. Grigorieva, and A. A. Firsov, "Electric Field Effect in Atomically Thin Carbon Films," *Science*, vol. 306, no. 5696, pp. 666–669, Oct. 2004.

[2] M. C. Lemme, "Current Status of Graphene Transistors," *arXiv:0911.4685*, Nov. 2009.

[3] A. K. Geim and K. S. Novoselov, "The rise of graphene," *Nature Materials*, vol. 6, no. 3, pp. 183–191, 2007.

[4] D. S. L. Abergel, V. Apalkov, J. Berashevich, K. Ziegler, and T. Chakraborty, "Properties of Graphene: A Theoretical Perspective," *arXiv:1003.0391*, Mar. 2010.

[5] A. H. Castro Neto, F. Guinea, N. M. R. Peres, K. S. Novoselov, and A. K. Geim, "The electronic properties of graphene," *Rev. Mod. Phys.*, vol. 81, no. 1, pp. 109–162, Jan. 2009.

[6] S. K. Banerjee, L. F. Register, E. Tutuc, D. Basu, S. Kim, D. Reddy, and A. H. MacDonald, "Graphene for CMOS and Beyond CMOS Applications," *Proceedings of the IEEE*, vol. 98, no. 12, pp. 2032 –2046, Dec. 2010.

[7] J.-H. Chen, C. Jang, S. Xiao, M. Ishigami, and M. S. Fuhrer, "Intrinsic and extrinsic performance limits of graphene devices on SiO2," *Nature Nanotechnology*, vol. 3, no. 4, pp. 206–209, 2008.

[8] W. Zhu, V. Perebeinos, M. Freitag, and P. Avouris, "Carrier scattering, mobilities, and electrostatic potential in monolayer, bilayer, and trilayer graphene," *Phys. Rev. B*, vol. 80, no. 23, p. 235402, Dec. 2009.

[9] K. S. Kim, Y. Zhao, H. Jang, S. Y. Lee, J. M. Kim, K. S. Kim, J.-H. Ahn, P. Kim, J.-Y. Choi, and B. H. Hong, "Large-scale pattern growth of graphene films for stretchable transparent electrodes," *Nature*, vol. 457, no. 7230, pp. 706–710, Jan. 2009.

[10] N. Petrone, C. R. Dean, I. Meric, A. M. van der Zande, P. Y. Huang, L. Wang, D. Muller, K. L. Shepard, and J. Hone, "Chemical Vapor Deposition-Derived Graphene with Electrical Performance of Exfoliated Graphene," *Nano Lett.*, vol. 12, no. 6, pp. 2751–2756, Jun. 2012.

[11] Y. Zhang, Y.-W. Tan, H. L. Stormer, and P. Kim, "Experimental observation of the quantum Hall effect and Berry's phase in graphene," *Nature*, vol. 438, no. 7065, pp. 201–204, Nov. 2005.

[12] F. Schwierz, "Graphene transistors," *Nature Nanotechnology*, vol. 5, no. 7, pp. 487–496, 2010.

[13] V. E. Dorgan, M.-H. Bae, and E. Pop, "Mobility and saturation velocity in graphene on SiO2," *Applied Physics Letters*, vol. 97, no. 8, pp. 082112–082112–3, Aug. 2010.

[14] Y. Taur and T. H. Ning, *Fundamentals of Modern VLSI Devices*. Cambridge University Press, 2009.

[15] A. A. Balandin, S. Ghosh, W. Bao, I. Calizo, D. Teweldebrhan, F. Miao, and C. N. Lau, "Superior Thermal Conductivity of Single-Layer Graphene," *Nano Lett.*, vol. 8, no. 3, pp. 902–907, Mar. 2008.

[16] R. Murali, Y. Yang, K. Brenner, T. Beck, and J. D. Meindl, "Breakdown current density of graphene nanoribbons," *Applied Physics Letters*, vol. 94, no. 24, pp. 243114–243114–3, Jun. 2009.

[17] X. Li, W. Cai, J. An, S. Kim, J. Nah, D. Yang, R. Piner, A. Velamakanni, I. Jung, E. Tutuc, S. K. Banerjee, L. Colombo, and R. S. Ruoff, "Large-Area Synthesis of High-Quality and Uniform Graphene Films on Copper Foils," *Science*, vol. 324, no. 5932, pp. 1312–1314, Jun. 2009.

[18] P. Blake, E. W. Hill, A. H. Castro Neto, K. S. Novoselov, D. Jiang, R. Yang, T. J. Booth, and A. K. Geim, "Making graphene visible," *Applied Physics Letters*, vol. 91, no. 6, pp. 063124–063124–3, Aug. 2007.

[19] M. I. Katsnelson, K. S. Novoselov, and A. K. Geim, "Chiral tunneling and the Klein paradox in graphene," *arXiv:cond-mat/0604323*, Apr. 2006.

[20] Wikipedia contributors, "MOSFET," *Wikipedia, the free encyclopedia*. Wikimedia Foundation, Inc., 28-Aug-2012.

[21] J. D. Cressler and G. Niu, *Silicon-Germanium Heterojunction Bipolar Transistors*. Artech House, 2003.

[22] F. Schwierz and J. J. Liou, *Modern microwave transistors: theory, design, and performance*. Wiley-Interscience, 2003.

[23] D. C. Elias, R. R. Nair, T. M. G. Mohiuddin, S. V. Morozov, P. Blake, M. P. Halsall, A. C. Ferrari, D. W. Boukhvalov, M. I. Katsnelson, A. K. Geim, and K. S. Novoselov, "Control of Graphene's Properties by Reversible Hydrogenation: Evidence for Graphane," *Science*, vol. 323, no. 5914, pp. 610–613, Jan. 2009.

[24] M. T. Ong and E. J. Reed, "Engineered Piezoelectricity in Graphene," *ACS Nano*, vol. 6, no. 2, pp. 1387–1394, Feb. 2012.

[25] Y. H. Lu, R. Q. Wu, L. Shen, M. Yang, Z. D. Sha, Y. Q. Cai, P. M. He, and Y. P. Feng, "Effects of edge passivation by hydrogen on electronic structure of armchair graphene nanoribbon and band gap engineering," *Applied Physics Letters*, vol. 94, no. 12, pp. 122111 –122111–3, Mar. 2009.

[26] D. W. Boukhvalov and M. I. Katsnelson, "Chemical Functionalization of Graphene with Defects," *Nano Lett.*, vol. 8, no. 12, pp. 4373–4379, Dec. 2008.

[27] J.-L. Li, K. N. Kudin, M. J. McAllister, R. K. Prud'homme, I. A. Aksay, and R. Car, "Oxygen-Driven Unzipping of Graphitic Materials," *Phys. Rev. Lett.*, vol. 96, no. 17, p. 176101, May 2006.

[28] A. Jorio, M. S. Dresselhaus, R. Saito, and G. Dresselhaus, *Raman Spectroscopy in Graphene Related Systems*. John Wiley & Sons, 2011.

[29] "Graphene," *Scribd*. [Online]. Available: http://www.scribd.com/doc/17157148/Graphene. [Accessed: 30-Aug-2012].

[30] K. Novoselov, "Beyond the wonder material," *Aalam Al-Zarra*, no. 124, pp. 16–20, Nov. 2009.

[31] D. W. Boukhvalov and M. I. Katsnelson, "Chemical functionalization of graphene," *arXiv:0809.5257*, Sep. 2008.

[32] Wikipedia contributors, "Graphane," *Wikipedia, the free encyclopedia*. Wikimedia Foundation, Inc., 29-Aug-2012.

[33] S. Lebègue, M. Klintenberg, O. Eriksson, and M. I. Katsnelson, "Accurate electronic band gap of pure and functionalized graphane from GW calculations," *Phys. Rev. B*, vol. 79, no. 24, p. 245117, Jun. 2009.

[34] H. Gao, L. Wang, J. Zhao, F. Ding, and J. Lu, "Band Gap Tuning of Hydrogenated Graphene: H Coverage and Configuration Dependence," *J. Phys. Chem. C*, vol. 115, no. 8, pp. 3236–3242, Mar. 2011.

[35] O. Leenaerts, H. Peelaers, A. D. Hernandez-Nieves, B. Partoens, and F. M. Peeters, "First-principles investigation of graphene fluoride and graphane," *Phys. Rev. B*, vol. 82, no. 19, Nov. 2010.

[36] J. T. Robinson, J. S. Burgess, C. E. Junkermeier, S. C. Badescu, T. L. Reinecke, F. K. Perkins, M. K. Zalalutdniov, J. W. Baldwin, J. C. Culbertson, P. E. Sheehan, and E. S. Snow, "Properties of Fluorinated Graphene Films," *Nano Lett.*, vol. 10, no. 8, pp. 3001–3005, Aug. 2010.

[37] M. Yang, L. Zhou, J. Wang, Z. Liu, and Z. Liu, "Evolutionary Chlorination of Graphene: From Charge-Transfer Complex to Covalent Bonding and Nonbonding," *J. Phys. Chem. C*, vol. 116, no. 1, pp. 844–850, Jan. 2012.

[38] W. Chen, S. Chen, D. C. Qi, X. Y. Gao, and A. T. S. Wee, "Surface Transfer p-Type Doping of Epitaxial Graphene," *J. Am. Chem. Soc.*, vol. 129, no. 34, pp. 10418–10422, Aug. 2007.

[39] X. Wang, X. Li, L. Zhang, Y. Yoon, P. K. Weber, H. Wang, J. Guo, and H. Dai, "N-Doping of Graphene Through Electrothermal Reactions with Ammonia," *Science*, vol. 324, no. 5928, pp. 768–771, May 2009.

[40] Wikipedia contributors, "Orbital hybridisation," *Wikipedia, the free encyclopedia*. Wikimedia Foundation, Inc., 28-Aug-2012.

[41] Wikipedia contributors, "Piezoelectricity," *Wikipedia, the free encyclopedia*. Wikimedia Foundation, Inc., 29-Aug-2012.

[42] N. Levy, S. A. Burke, K. L. Meaker, M. Panlasigui, A. Zettl, F. Guinea, A. H. C. Neto, and M. F. Crommie, "Strain-Induced Pseudo–Magnetic Fields Greater Than 300 Tesla in Graphene Nanobubbles," *Science*, vol. 329, no. 5991, pp. 544–547, Jul. 2010.

[43] A. K. Geim, "Graphene: Status and Prospects," *Science*, vol. 324, no. 5934, pp. 1530–1534, Jun. 2009.

[44] A. C. Ferrari, J. C. Meyer, V. Scardaci, C. Casiraghi, M. Lazzeri, F. Mauri, S. Piscanec, D. Jiang, K. S. Novoselov, S. Roth, and A. K. Geim, "Raman Spectrum of Graphene and Graphene Layers," *Phys. Rev. Lett.*, vol. 97, no. 18, p. 187401, Oct. 2006.

[45] L. M. Malard, M. A. Pimenta, G. Dresselhaus, and M. S. Dresselhaus, "Raman spectroscopy in graphene," *Physics Reports*, vol. 473, no. 5–6, pp. 51–87, Apr. 2009.

[46] C. H. Lui, Z. Li, K. F. Mak, E. Cappelluti, and T. F. Heinz, "Observation of an electrically tunable band gap in trilayer graphene," *Nature Physics*, vol. 7, no. 12, pp. 944–947, 2011.

[47] X. Li, Y. Zhu, W. Cai, M. Borysiak, B. Han, D. Chen, R. D. Piner, L. Colombo, and R. S. Ruoff, "Transfer of Large-Area Graphene Films for High-Performance Transparent Conductive Electrodes," *Nano Lett.*, vol. 9, no. 12, pp. 4359–4363, Dec. 2009.

[48] X. Li, C. W. Magnuson, A. Venugopal, R. M. Tromp, J. B. Hannon, E. M. Vogel, L. Colombo, and R. S. Ruoff, "Large-Area Graphene Single Crystals Grown by Low-Pressure Chemical Vapor Deposition of Methane on Copper," *J. Am. Chem. Soc.*, vol. 133, no. 9, pp. 2816–2819, Mar. 2011.

[49] Wikipedia contributors, "Photolithography," *Wikipedia, the free encyclopedia*. Wikimedia Foundation, Inc., 28-Aug-2012.

[50] D. T. Tran, T. A. Grotjohn, D. K. Reinhard, and J. Asmussen, "Microwave plasma-assisted etching of diamond," *Diamond and Related Materials*, vol. 17, no. 4–5, pp. 717–721, Apr. 2008.

[51] Wikipedia contributors, "X-ray photoelectron spectroscopy," *Wikipedia, the free encyclopedia*. Wikimedia Foundation, Inc., 30-Aug-2012.

[52] S. Das Sarma, S. Adam, E. H. Hwang, and E. Rossi, "Electronic transport in two-dimensional graphene," *Rev. Mod. Phys.*, vol. 83, no. 2, pp. 407–470, May 2011.

[53] Wikipedia contributors, "Diamond," *Wikipedia, the free encyclopedia*. Wikimedia Foundation, Inc., 31-Aug-2012.

[54] F. Withers, M. Dubois, and A. K. Savchenko, "Electron properties of fluorinated single-layer graphene transistors," *Phys. Rev. B*, vol. 82, no. 7, p. 073403, Aug. 2010.

[55] K.-J. Jeon, Z. Lee, E. Pollak, L. Moreschini, A. Bostwick, C.-M. Park, R. Mendelsberg, V. Radmilovic, R. Kostecki, T. J. Richardson, and E. Rotenberg, "Fluorographene: A Wide Bandgap Semiconductor with Ultraviolet Luminescence," *ACS Nano*, vol. 5, no. 2, pp. 1042–1046, Feb. 2011.

[56] B. Li, L. Zhou, D. Wu, H. Peng, K. Yan, Y. Zhou, and Z. Liu, "Photochemical Chlorination of Graphene," *ACS Nano*, vol. 5, no. 7, pp. 5957–5961, Jul. 2011.

[57] Wikipedia contributors, "Electronegativity," *Wikipedia, the free encyclopedia*. Wikimedia Foundation, Inc., 29-Aug-2012.

[58] J. Wu, L. Xie, Y. Li, H. Wang, Y. Ouyang, J. Guo, and H. Dai, "Controlled Chlorine Plasma Reaction for Noninvasive Graphene Doping," *J. Am. Chem. Soc.*, vol. 133, no. 49, pp. 19668–19671, Dec. 2011.